

EXPERIMENTAL STUDY OF A NOVEL GAS TURBINE ENGINE INTEGRATED WITH  
AN ABSORPTION REFRIGERATION SYSTEM

by

ERIC B. HOWELL

A THESIS PRESENTED TO THE GRADUATE SCHOOL  
OF THE UNIVERSITY OF FLORIDA IN PARTIAL FULFILLMENT  
OF THE REQUIREMENTS FOR THE DEGREE OF  
MASTER OF SCIENCE

UNIVERSITY OF FLORIDA

2007

© 2007

Eric B. Howell

## ACKNOWLEDGMENTS

I first thank my committee chair, Dr. William Lear, for giving me the great opportunity to be a part of this research effort, and for his counsel throughout my graduate studies. I would also thank Dr. S. A. Sherif, and Dr. Herbert Ingley for serving on my committee and demonstrating great patience with me throughout this work. I must also thank Mr. John Crittenden for all of his advice, encouragement, and comradeship during this undertaking. I am also indebted to Mr. Dan Brown and Mr. Todd Nemecek for all their technical assistance and recommendations.

# TABLE OF CONTENTS

	<u>page</u>
ACKNOWLEDGMENTS .....	3
LIST OF TABLES .....	7
LIST OF FIGURES .....	8
LIST OF TERMS.....	10
ABSTRACT.....	14
CHAPTER	
1 INTRODUCTION.....	16
2 LITERATURE REVIEW .....	21
History of Semi-Closed Cycle Concepts.....	21
Analytical Studies.....	22
Experimental Studies.....	24
3 TESTING HARDWARE.....	26
Combined Cycle Components.....	26
Engine Characteristics and Specifications.....	26
Recuperator.....	27
Turbocharger .....	27
Heat Exchangers.....	27
Hot gas cooler (HGC) .....	28
Warm gas cooler (WGC).....	28
Cold gas cooler (CGC).....	28
Dynamometer .....	29
Ducting .....	29
Facility Resources.....	29
Chilled Water.....	29
Fans and HVAC .....	30
Vapor Absorption Refrigeration System (VARs).....	30
Overview of Build Configurations .....	30
Build 1 .....	31
Build 2A .....	32
Build 3 .....	33
Build 4.....	34

Data Measurement .....	34
Data Acquisition Hardware .....	34
Data Acquisition Software .....	36
Instrumentation .....	36
Thermocouples .....	36
Pressure transducers .....	37
Turbine and paddle-wheel flowmeters .....	37
Optical tachometer .....	37
Load cells .....	38
Gas analysis .....	38
Mechanical instruments and analog readers .....	39
4 TEST PROCEDURES .....	45
Test Plan .....	45
Engine/Component Preparation .....	45
Instrument Preparation .....	46
Transducer Offsets .....	46
Ambient Conditions .....	47
5 DATA REDUCTION SCHEME .....	49
Gas Properties .....	49
Enthalpy and Specific Heat .....	50
Gas Composition .....	52
Basic Equations and Assumptions .....	54
Main Air Inlet (MAI) .....	54
Low Pressure Compressor (LPC) .....	55
Recirculation Venturi (RCV) .....	55
Hot Gas Cooler (HGC) .....	56
Warm Gas Cooler (WGC) .....	56
Cold Gas Cooler (CGC) .....	58
Ducting Section 4-5 .....	59
High Pressure Compressor (HPC) .....	60
Combustor .....	61
Ducting Section 7-8 .....	63
High Pressure Turbine (HPT) .....	64
Recuperator .....	66
Low Pressure Turbine (LPT) .....	68
Mixing Junctions .....	68
Propagation of Uncertainty .....	70
Data Adjustments .....	72
Pressure Drop Considerations .....	73
6 EXPERIMENTAL RESULTS .....	79

7	CONCLUSIONS AND RECOMMENDATIONS .....	105
	Summary .....	105
	Recommendations.....	107
APPENDIX		
A	OPERATING PROCEDURES FOR HPRTE/VARS .....	110
B	SETUP PROCEDURES FOR HPRTE/VARS .....	113
C	ADJUSTED EXPERIMENTAL DATA .....	119
	LIST OF REFERENCES .....	135
	BIOGRAPHICAL SKETCH .....	137

## LIST OF TABLES

<u>Table</u>	<u>page</u>
3-1. Temperature locations and instrumentation. ....	40
3-2. Pressure locations and instrumentation. ....	41
5-1. Uncertainty of instruments .....	74
5-2. Data scaling parameters [19]. ....	75
C-1. Data from runs B4-1 and B4-2. ....	119
C-2. Data from runs B4-3 and B4-5. ....	121
C-3. Data from runs B4-7 and B4-8. ....	123
C-4. Data from runs B4-10 and B4-11. ....	125
C-5. Data from run B4-12. ....	127
C-6. Data from run B4-14. ....	129
C-7. Data from runs B4-15 and B4-16. ....	131
C-8. Data from run B4-17. ....	133

## LIST OF FIGURES

<u>Figure</u>	<u>page</u>
1-1. Block diagram of HPRTE flow path. ....	20
3-1. Block diagram of Build 1 configuration. ....	42
3-2. Photograph of Build 1 improvised evaporator installation. ....	43
3-3. Block diagram of Build 2A configuration. ....	43
3-4. Block diagram of Build 3 configuration. ....	44
3-5. Block diagram of Build 4 configuration. ....	44
5-1. Map used for finding the HPC adiabatic exit temperature, shown as a function of corrected flow rate and corrected speed [16]. ....	76
5-2. Rover 1S-60 internal power losses as a function of rotor speed [16]. ....	77
6-1. Actual net power output from Build 4 engine runs. ....	92
6-2. Corrected Power, power, and thermal efficiency over corrected speed. ....	93
6-3. Scaling parameters versus corrected speed. ....	93
6-4. Theta versus LPC pressure ratio. ....	94
6-5. Power versus LPC pressure ratio. ....	94
6-6. High pressure turbomachinery temperature differences and mass flow rate versus LPC pressure ratio. ....	95
6-7. Percent change in high pressure turbomachinery temperature differences and mass flow rate versus LPC pressure ratio. ....	95
6-8. Flow parameters versus corrected speed. ....	96
6-9. Generalized effects of HPC pressure ratio and CTR on specific power, illustrated on a T-S diagram. ....	96
6-10. Specific power versus CTR, for various HPC pressure ratios. ....	97
6-11. Corrected power versus CTR for various HPC pressure ratios. ....	97
6-12. HPC pressure ratio and CTR versus corrected speed. ....	98
6-13. Thermal efficiency versus CTR. ....	98

6-14. Thermal efficiency versus HPC pressure ratio. ....	99
6-15. HPC isentropic efficiency versus corrected speed. ....	99
6-16. Recirculation ratio versus LPC pressure ratio. ....	100
6-17. Fresh air flow rate versus recirculation ratio. ....	100
6-18. Equivalence ratio versus recirculation ratio. ....	101
6-19. Equivalence ratio versus LPC pressure ratio. ....	101
6-20. Nitric oxide and carbon monoxide concentrations versus recirculation ratio. ....	102
6-21. Oxygen and nitrogen concentrations versus recirculation ratio. ....	102
6-22. Water-to-fuel ratio versus LPC pressure ratio. ....	103
6-23. Recirculation flow rate versus LPC pressure ratio. ....	103
6-24. Temperatures related to water extraction versus LPC pressure ratio. ....	104

## LIST OF TERMS

### Roman Letters

a	first degree coefficient for specific heat polynomial
A	cross sectional area
b	second degree coefficient for specific heat polynomial
c	third degree coefficient for specific heat polynomial
$c_p$	constant-pressure specific heat
e	heat exchanger effectiveness
F	force
FA	fuel-to-air ratio
h	specific enthalpy or convection coefficient
M	molecular weight
$\dot{m}$	mass flow rate
n	moles
$\dot{n}$	mole flow rate
N	engine speed
$N^*$	corrected engine speed
P	pressure or power
$P^*$	corrected power
PR	pressure ratio
$\dot{Q}$	heat transfer rate
R	mass-specific gas constant or recirculation ratio
$\bar{R}$	mole-specific (universal) gas constant

T	temperature
$\dot{V}$	volumetric flow rate
$\dot{W}$	power
y	mole fraction

### Greek Letters

$\gamma$	specific heat ratio
$\delta$	pressure correction parameter
$\varepsilon$	emissivity
$\eta$	efficiency
$\theta$	temperature correction parameter
$\rho$	density
$\sigma$	Stefan-Boltzmann constant
$\tau$	dimensionless temperature parameter
$\omega$	angular velocity, or uncertainty

### Subscripts

0	reference state, 300 Kelvin
AMB	ambient
AVG	average
COLD	cold side of heat exchanger
COMB	combustor
CONV	convective
DAQ	data acquisition
DRY	dry gas mixture, omitting water

DYNO	dynamometer
fg	liquid-vapor transition
HOT	hot side of heat exchanger
HPTI	high pressure turbine inlet
HPTX	high pressure turbine exit
i	$i^{\text{th}}$ term in a series, or $i^{\text{th}}$ constituent of a mixture
in	general inlet state point
INST	instrumentation
LPCI	low pressure compressor inlet
LPCX	low pressure compressor exit
max	maximum possible value
MIX	mixture
MECH	mechanical friction
NC	non-condensable
out	general outlet state point
R	recuperator
RAD	radiative
RCVI	recirculation venturi inlet
SEN	sensible
SURF	surface
TOT	total value for mixture
TRAN	transient
W	water

WGCG	warm gas cooler, gas side
WGCI	warm gas cooler inlet
WGCW	warm gas cooler, water side
X	generalized independent parameter

Abstract of Thesis Presented to the Graduate School  
of the University of Florida in Partial Fulfillment of the  
Requirements for the Degree of Master of Science

EXPERIMENTAL STUDY OF A NOVEL GAS TURBINE  
ENGINE INTEGRATED WITH AN ABSORPTION REFRIGERATION SYSTEM

by

Eric B. Howell

August 2007

Chair: William E. Lear

Major: Mechanical Engineering

A series of tests were performed on a novel gas turbine engine, coupled to a vapor absorption refrigeration system. The engine cycle is unique in that it is semi-closed and turbocharged in addition to utilizing a recuperator. The refrigeration system is in place to remove heat from the recirculating exhaust gases, to cool the engine inlet gases, and to produce additional refrigeration for auxiliary thermal loads. The engine was developed in several stages and operated over a wide range of conditions. The data from these experiments were reduced, analyzed and presented with emphasis placed on the unique attributes of the combined cycle. Observed hardware limitations are also identified, and adjustments were made to the data in an effort to estimate certain performance parameters for more ideal components.

It was observed in these experiments that power transitions could be made with this cycle by varying the turbocharger pressure ratio. Doing so results in a somewhat constant thermal efficiency over a range of power levels, since the core engine approximately remains at a constant, dimensionless operating point. It is also shown that semi-closure of the power cycle reduces the air flow necessary to run the engine, highlighting the anticipated size reduction of certain components. The data also validate that semi-closure of the cycle serves to alter the combustion environment, such that  $\text{NO}_x$  emissions are reduced, making the power cycle more

attractive from an environmental perspective. The cooling of recirculation gases presents the additional opportunity to extract fresh water from the gas path. This capability is also realized in these experiments, but the amount of water extracted was limited by some of the experimental hardware to less than half the theoretical maximum.

## CHAPTER 1 INTRODUCTION

With rising energy costs and instability of energy sources, it is becoming ever more important to develop newer technologies to meet the unrelenting increase in demand for energy. This challenge is further complicated by concerns about the current and future states of the environment, and must be overcome while concurrently decreasing any negative, environmental impacts. Distributed generation of energy is seen as a potential solution, at least in part, to present energy challenges. Some varieties of distributed generation exist in the form of solar panels and wind turbines, which use natural energy sources that are often inconsistent and dependant upon weather. Moreover, these types of systems must be implemented on a large scale if they are to be significant contributors to the energy supply. Microturbines are also becoming more attractive as distributed generation systems, as they are more compact and can burn a large variety of fuels. Microturbines also provide the capability of supporting heating loads with exhaust gases, and more recent innovations utilize absorption refrigeration systems to provide refrigeration loads as well.

It is hypothesized that several innovations to the conventional gas turbine engine can increase its usefulness as a distributed generation system. The particular improvements implemented in this study are believed to reduce the physical size of the engine and enable it to follow load demands without significant sacrifices of thermal efficiency. In addition, it is theoretically possible for the integration of such an engine with a Vapor Absorption Refrigeration System (VARs) to further enhance its attractiveness by enabling the combined cycle to produce external refrigeration, and fresh water.

In an effort to better quantify the extent of these prospective capabilities, modeling and experimental activities were conducted at the University of Florida. This thesis details the

experimental efforts undertaken on a novel gas turbine engine cycle combined with a VARS. The power cycle is unique in that it is both semi-closed and turbocharged, in addition to being recuperated, and is referred to as the High Pressure Regenerative Turbine Engine (HPRTE). Figure 1-1 shows the flow path of the HPRTE.

There are two main reasons for turbocharging the gas turbine engine. The first, more apparent of these is the resulting increase in power density. By increasing the pressure of the working fluid, the density is also increased. In turn, the same size engine can operate with a greatly increased mass flow rate which equates to more power from a smaller engine. The second reason for turbocharging the gas turbine engine is more subtle. The engine thermal efficiency can remain approximately constant over a range of power levels. This is accomplished by using the turbocharger itself to perform power transitions. Exhaust can be diverted through/around the Low Pressure Turbine (LPT) to raise/lower the inlet pressure of the engine. If the inlet temperature is held constant, then the density and flow rate will in turn increase proportionately to the inlet pressure. Doing so allows the core engine to remain at the same, dimensionless operating point (same corrected flow corrected power and pressure ratios) for different power levels. The core engine is simply the recuperated gas turbine engine being operated apart from other, supporting hardware (turbocharger, VARS, etc.).

It is also theorized that the semi-closure of the gas turbine cycle also offers several advantages over conventional gas turbine cycles. The first of these relates to the fact that about 20 percent of the air ingested by a conventional gas turbine engine is necessary to support combustion. Semi-closing the cycle entails recirculating much of the exhaust gases to be used again as the working fluid, and as this recirculated proportion of gas is increased, the net inflow and outflow of air and exhaust gas are reduced. This effect is believed to significantly reduce the

size of the turbocharger and other inlet air and exhaust ducting. Some applications may also find significant utility in the smaller thermal and acoustic signatures from the engine resulting from the reduced exhaust flow.

Speculations are also made regarding the attractiveness of the semi-closed gas turbine engine from an environmental perspective. The more oxygen-dilute gases are expected to reduce the temperature within the primary zone of the combustor. This should result in a significant reduction of oxides of nitrogen ( $\text{NO}_x$ ), since  $\text{NO}_x$  formation rates scale very strongly with temperature. Similar arguments can also be made about soot formation rates.

Recirculating significant quantities of hot exhaust gases to the High Pressure Compressor (HPC) inlet presents both the problem of significant cooling, and the benefit of fresh water extraction. Aside from its front-end material considerations, the gas turbine engine would perform poorly with such extreme temperatures of mixed inlet gases. Hence, these gases must be cooled. However, a benefit is made available by the cooling of these gases, as an appreciable fraction of the recirculation flow is water vapor. Once condensed in the cooling process, the water can straightforwardly be extracted and made ready to drink. This rather large cooling challenge presented by the recirculating exhaust gases can be viewed as an opportunity to extract further potential from the power cycle via integration of the VARS.

The VARS is driven by the heat rejected from the recirculation loop and in turn benefits the HPRTE in several ways. The most notable of these is the theoretical capability it offers for reducing the HPC inlet temperature to below ambient temperatures, and improving the engine performance. This attribute implies that the engine performance should depend much less, if at all, on ambient conditions, since the HPC inlet temperature and pressure can be controlled by the VARS and turbocharger, respectively. Additionally, it is theorized that the VARS can produce

more refrigeration than is necessary for the gas-path cooling. As a result, a fourth commodity, refrigeration, can be counted alongside of power, heat, and water as an output from this combined cycle.

The apparent advantages and capabilities of this combined cycle motivated the US Army Research Laboratory to fund the development of an experimental HPRTE/VARS combined cycle for the purpose of demonstrating its thermodynamic principles. The University of Florida was subcontracted to carry out the design and testing of several experimental apparatuses within its Energy and Gasdynamics Laboratory (EGDL). The overall objectives of this research work were to assemble an experimental HPRTE/VARS combined cycle, demonstrate its operability, and demonstrate that its theoretical capabilities could be realized in accordance with the predictions of thermodynamic models. A stepwise approach was taken in the experimental development such that the capabilities of the experimental apparatus were expanded incrementally. A second objective of the experimental work was to help develop and validate design-point models for this combined cycle. Though details of the modeling efforts are not within the scope of this work, some comparisons are made between the modeled and experimental results.

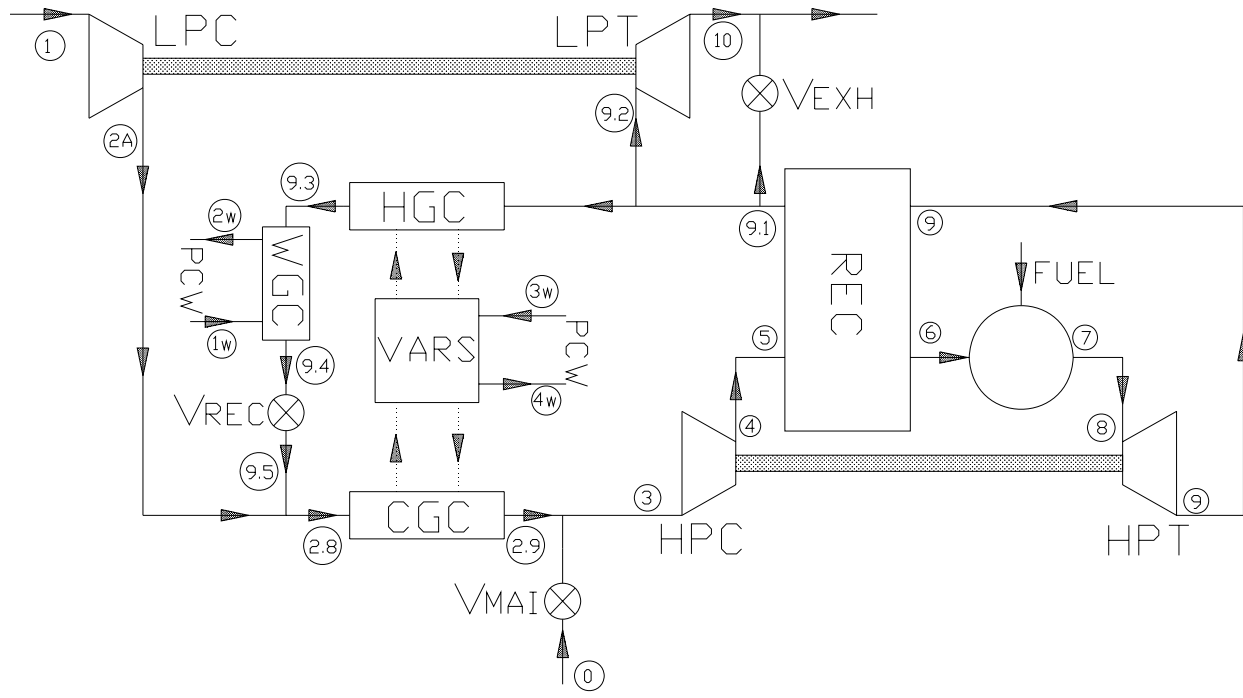


Figure 1-1. Block diagram of HPRTE flow path.

## CHAPTER 2 LITERATURE REVIEW

### **History of Semi-Closed Cycle Concepts**

Innovations in the Brayton cycle have continued to improve the performance of gas turbine engines since their inception. One such improve, and perhaps the most pertinent to this work is the semi-closure of the Brayton cycle. Although little development has been done recently, the concept of semi-closure is nearly as old as gas turbines, as summarized by Gasparovic [1]. As early as 1940s, attempts were made at developing semi-closed gas turbine engines. The initial attempts at recirculating exhaust gases in a semi-closed cycle were plagued with corrosion associated with the heavy fuel oils of the time. Subsequent efforts only recirculated air in a secondary, “charging” circuit that added excessive complications and costs to the cycle.

In the late 1960s Gasparovic attempted to revive the previously abandoned idea of semi-closer, as fuel technology had progressed. He also presented the idea of semi-closure implemented with a low-pressure turbocharging system. In [1], he notes the potential of gas turbine engines of a given power to be made smaller, estimating a pound-per-horsepower of about 2/3 that of conventional engines. He also points out the advantage of part-load efficiency achieved by varying the low-pressure charging of the cycle. Specifically, he cites the Sulzer Brothers’ design for a 20 MW plant operating at 32% efficiency at full power, and at 28% efficiency at only half power. Again, this engine eventually failed due to excessive corrosion.

In recent years several research efforts at the University of Florida have once again revitalized the semi-closed, turbocharged, gas turbine engine referred to as the HPRTE. These studies have focused on many of the specific HPRTE attributes, as well as on various applications thought to be well suited by this cycle. However, most of the more recent, University of Florida studies were modeling analyses.

## Analytical Studies

Nemec [2] conducted studies on the HPRTE with a Rankine bottoming cycle. In his work, several bottoming cycle fluids were considered, as well as feedwater heating, superheating and recuperation in relation to optimizing the overall thermal efficiency. One apparent challenge in Nemec's analysis was matching the bottoming-cycle performance with that of the topping cycle. However, with the fluids and components considered, an optimal thermal efficiency of 54.5% was reported. Nemec notes that higher efficiencies are possible with the inclusion of different bottoming fluids and combined cycle components.

Landon [3] and Danias [4] performed several independent, but similar analytical studies on the HPRTE. Landon's analysis evaluated the suitability of several HPRTE configurations for marine applications and compared them with currently employed technology. Those results indicate significantly higher part-load efficiencies, resulting in a 24% increase in range for a given marine vessel. Danias' analysis also revealed similar qualities from two HPRTE cycles, but for helicopter applications. His model predicted an increase in non-dimensional range of up to 46% over a conventional helicopter engine resulting from the improved efficiency at off-design power levels. Danias' simulations also predicted design-point efficiency increases of 30-35% over the baseline engine, at the expense of a bearing a slightly larger and heavier recuperated engine.

MacFarlane [5] investigated the implications of extracting water from the HPRTE recirculation flow path. He also looked into any potential benefits of water re-injection into the cycle. His results show a maximum possible decrease of Specific Fuel Consumption (SFC) of about 8%. Furthermore, MacFarlane found that water extraction could also increase the specific power by about 4.5% over baseline. Re-injection of water back into the cycle seemed to increase SFC by about 2%, with little or no other impact on other performance parameters. However, it is

noted that the increase in SFC comes with the injection of water in its liquid phase, and that this increase would be less if the water were injected as steam.

Muley [6] carried out studies on the emissions-related effects of semi-closure. In his work, Muley focused primarily on how the formation of thermal  $\text{NO}_x$  was impacted by recirculating exhaust gases. He discovered that an impressive reduction of thermal  $\text{NO}_x$  could be realized by semi-closure of a gas turbine power cycle. This effect grew more pronounced with further dilution of the combustor inlet gases, yielding a decrease in thermal  $\text{NO}_x$  of about eight to nine orders of magnitude, depending also on the combustor inlet temperature.

Boza [7] was the first to perform a modeling analysis on the HPRTE power cycle combined with a VARS in 2003. In his modeling efforts, Boza uncovered some striking performance characteristics made possible by the combination of these cycles. He simulated a large engine (40 MW) and a small engine (100kW), and evaluated their performance when coupled to a Lithium-Bromide (Li-Br) VARS, considering both power and refrigeration as beneficial outputs. Auxiliary refrigeration was presented as a percentage of nominal power. For the large engine, Boza estimated a thermal efficiency of about 62% with 25% auxiliary refrigeration at 85°F ambient conditions. This efficiency dropped only two points for the same operating point on a 103°F day. Boza points out that even higher efficiencies are calculated if the auxiliary refrigeration is considered alongside of power in the efficiency definition. For the small engine Boza showed a thermal efficiency of about 43%, but with an additional 50% of auxiliary refrigeration, again on an 85°F day. The thermal efficiency of this engine dropped three points for the 103°F day. Boza also indicated that ambient conditions directly affected only the VARS performance. This highlights the combined-cycle feature that refrigeration and

efficiency can be interchangeable, and that auxiliary refrigeration can be shunted back into the HPRTE cycle to recover efficiency points if desired.

The most recent modeling work on the combined HPRTE/VARS cycle was completed by Khan [8] in 2006. Khan's model was intended to predict and optimize the design-point performance of a medium-sized engine with conservative, but modern efficiencies and temperature limitations. Khan's models added to Boza's work in that he accounted for the water condensation associated with the gas-path cooling, and explored the implications of using different refrigerants. The figure of merit used was a linear combination of efficiency, auxiliary refrigeration, and water extraction. His model predicted an attainable thermal efficiency of 40.5% at an optimal low-pressure-spool pressure ratio of two, and a turbine inlet temperature of around 2550°F. Khan also showed that 1.5 pounds of water could be extracted from the cycle for every pound of propane fuel consumed. Khan's results are similar to Boza's small-engine results with the exception of his predicted external refrigeration—38% of nominal power for a Li-Br cycle. This difference is probably related to Khan's accounting for water condensation.

### **Experimental Studies**

Several experimental research initiatives have also been carried out at the University of Florida to further explore characteristics of HPRTE performance and operation. One program in particular was funded by NASA in the late 1990s to evaluate a turbocharged Titan T62T32A gas turbine engine operating in a semi-closed cycle configuration. This program [9] proved many of the concepts upon which the HPRTE is founded. Though plagued by hardware problems unrelated to the focus of the research, HPRTE operations yielded power increases of up to 70% by turbocharging. Shortcomings in the fuel and control systems limited this test program from fully realizing the constant efficiency and SFC potentials of the HPRTE. However, some simple scaling arguments provided within [9] show that with more accommodating controls and fuel

components, the efficiency and SFC would remain much more constant for various operating points. The anticipated, positive impact of semi-closure on emissions also was validated within this test program. The HPRTE CO emissions were observed to be a factor of 25 less than the baseline values. This was thought to result from larger proportions of water in the working fluid due to recirculation. Spray coolers were also employed on the apparatus to aid in recirculation-gas cooling, and also contributed to a higher water concentration in the working fluid. The reduction of NO<sub>x</sub> emissions was also observed, but to a lesser extent than predicted by Muley in [6]. The potential for reduced NO<sub>x</sub> emissions was hindered by lower-than-expected recirculation flow rates and non-uniformities in the combustor temperature field. Other experimental efforts, detailed in [10] and also funded by NASA, focused on the development of more suitable combustors for stable, semi-closed engine operations.

Previous experimental efforts have, by necessity, incorporated some means of cooling to the recirculation gas path, as this is essential for reliable and efficient engine operation. Most frequently, one or more air-to-water intercoolers were employed to meet this need. To date, based on the apparent absence of any relevant literature, it seems as if no experiments have been performed on a semi-closed cycle gas turbine combined with a VARS, so the present study represents the first of its kind.

## CHAPTER 3 TESTING HARDWARE

An experimental apparatus was conceived for demonstrating the capabilities of the HPRTE/VARS combined cycle. This apparatus was centered around a Rover 1S-60 gas turbine engine and a custom-built VARS. In order to operate the combined cycle and successfully acquire useful data, a host of other components were necessary, such as facility cooling resources and instrumentation. This chapter describes each of the elements in the HPRTE/VARS combined cycle, their roles, and their specifications, where available.

### **Combined Cycle Components**

This section lists the various components relating to the combined cycle, along with a detailed description for each.

#### **Engine Characteristics and Specifications**

The Rover 1S-60 is a single spool turboshaft engine that was designed and manufactured in the late 1950s and early 1960s. It was primarily used for Auxiliary Power Units (APU) and fire-fighting water pumps before being used as an educational tool. The engine remained in production for about 20 years during which its safety, reliability, and longevity were well proven [11].

The engine utilizes a 19 blade, radial compressor and radial diffuser vanes with a design flow rate of about 1.33 lbs/s (0.603 kg/s), and pressure ratio of 2.8:1. To accommodate the dilute oxygen concentrations in the semi-closed cycle, the reverse-flow combustor was modified by welding stainless steel straps over some of the dilution holes, forcing more gases—and more oxygen—into the primary zone. Modifications were also made to intercept the flow from the compressor, redirecting it through the recuperator before returning it to the combustor. The working fluid is then expanded across a 30-blade axial turbine. The nominal rated output of this

engine is 60 hp (45 kW) at a mechanically governed shaft speed of 46,000 rpm, with a thermal efficiency around 14%. The rotor speed is reduced in a gearbox on the front end of the engine to 3000 rpm, where a shaft transmits power to a water-brake dynamometer.

Further modifications were also made to the engine casing, replacing it with thicker steel. This was necessary before pressurized operations could be safely attempted since the pressure within the casing was expected to increase by as much as a factor of two.

### **Recuperator**

The recuperator is a custom unit designed and fabricated by Elanco. It is a single-pass tube-and-shell heat exchanger with 672, 0.375-inch (9.53 mm) stainless steel tubes extending 27 inches (69 cm) through the shell-side. The tubes are enclosed with 14-inch (36 cm) diameter, 40 gauge stainless steel [12]. The hot-side inlet is attached to the turbine exhaust ducting with a V-band clamp, while the hot-side uses an 8-bolt flange to connect to downstream ducting. The cold-side ducting attaches with 12-bolt flanges. The recuperator design effectiveness is about 0.51 [12].

### **Turbocharger**

The turbocharger used was a Garret GT 4294-731376-1, with a turbine scroll Area to Radius (AR) ratio of 1.44. This turbocharger was chosen primarily for its superb compressor efficiency, which would delivery higher pressure ratios with relatively cooler turbine-side inlet temperatures. Additionally, the Garret 4294 was shown by an off-design model to match well with desired HPRTE operating points [13]. The turbocharger relies on an independent oil pump, dry sump, and oil cooler to provide its lubrication requirements.

### **Heat Exchangers**

Three heat exchangers were made necessary by the recirculation of hot exhaust gases to the front end of the engine. All three are arranged in series in the recirculation line, and each is

named according to the qualitative state of the recirculation gases entering it: the Hot Gas Cooler (HGC), Warm Gas Cooler (WGC), and Cold Gas Cooler (CGC).

### **Hot gas cooler (HGC)**

The HGC is a custom heat exchanger designed and fabricated by Energy Concepts in Annapolis Maryland for this application. End-to-end, it is 36 inches (91 cm) long, and transitions from six inch Outside Diameter (OD) ducting, to a 12 inch (30 cm) OD shell, and back to the six inch ducting. No baffles are employed within the heat exchanger, and all stainless steel construction is used. The tube-side heat transfer medium is a strong solution of ammonium and water. There is intended to be phase change within the HGC tube-side, since it serves as the vapor generator for the VARS.

### **Warm gas cooler (WGC)**

The WGC was necessary if sub-ambient inlet temperatures were to be possible. It serves the purpose of rejecting heat to ambient (though it uses a cooler-than-ambient medium) before recirculating gases are last cooled by the CGC. The WGC is an air-to-water heat exchanger that makes use of the facilities chilled water circuit. Chilled water makes two passes in the tube-side, while the recirculation gases turn through several baffles on one shell pass. Again, Elanco designed and manufactured the WGC using all stainless steel construction. The design effectiveness of this heat exchanger is 0.85 [12].

### **Cold gas cooler (CGC)**

The CGC was also constructed of stainless steel by Energy Concepts, and functioned as the evaporator for the VARS. This heat exchanger is, in principle, capable of chilling the High Pressure Compressor (HPC) inlet gases to sub-ambient temperatures. It is longer than the HGC—about 48 inches (1.2 m)—with the same types of transitions on each end, and also uses no baffles within. Ideally, the heat transfer medium is pure, liquid ammonia undergoing phase

change with a few degrees of superheat upon exiting the CGC. The gases on the shell side consist of recirculation gases mixed with fresh air from the Low Pressure Compressor (LPC).

### **Dynamometer**

The dynamometer is contemporary with the Rover 1S-60 and was sold as an integral package with the engine. It is a water-brake manufactured by Heenan & Froude (now Froude Hofmann) and is equipped with a mechanical tachometer. The spring balance with which the dynamometer was originally equipped was replaced with a load cell and reader. The original, mechanical tachometer is also supplemented with an optical tachometer directed at reflective tape on the Power Take-Off (PTO).

### **Ducting**

The ducting used throughout the HPRTE rig was six-inch (15 cm) OD aluminized steel with a thickness of 0.070 inches (1.78 mm). It was manufactured for use as exhaust pipe for large trucks, and was chosen for its availability, low cost, and light weight. Pipe-to-pipe connections were made using 0.375 inch (9.53 cm) thick, 12-bolt custom flanges which were welded to each pipe-end.

## **Facility Resources**

There were several of the building assets that were both useful and essential for conducting engine runs. These dealt primarily with the issue of removing heat from the engine room. The building chilled water circuit served to remove heat from the power and refrigeration cycles, while the ventilation systems available helped to maintain uniform temperatures within the EGDSL during engine runs.

### **Chilled Water**

The building in which the EGDSL is situated utilizes a closed-circuit Process Chilled Water (PCW) system to function as a cooling medium for several labs in the building. This

system was tapped into and can be accessed from one of two headers in the EGDSL: one on the north wall, and one on the south wall. Each header is capable of delivering about 35 gpm (2.2 kg/s), or one header can deliver about 64 gpm (4.0 kg/s). All of the heat rejected from the recirculation gas path ultimately finds its way into this cooling circuit. The VARS is cooled by the south header, and the WGC by the north header. The PCW circuit in turn rejects its heat to a stacked plate heat exchanger elsewhere in the building, which has a maximum heat transfer rate of almost 200 TR (703 kW). PCW temperatures are typically controlled to be around 55 °F (286 K), but by altering the PCW control scheme can be made as cool as 42 °F (279 K).

### **Fans and HVAC**

To impede the accumulation of harmful exhaust fumes within the testing facility, two fans have been employed to move fresh air through the EGDSL. An existing air conditioning unit also exists in the EGDSL, the service of which is shared with a neighboring room. While this unit does little to cool the room during engine operations, it does help to move more fresh air from elsewhere into the EGDSL.

### **Vapor Absorption Refrigeration System (VARS)**

The VARS is a custom refrigeration unit designed and built by Energy Concepts. The VARS is a unique, single-effect, ammonia-water absorption refrigeration system with a maximum evaporator heat load of 19 TR (67 kW), at a COP of 0.85. The VARS interacts with the HPRTE via the HGC and CGC described above, and rejects heat from the absorber and condenser through the south PCW header.

### **Overview of Build Configurations**

To help ensure that all of the hypothesized attributes of this combined cycle could be demonstrated and explored, several small, progressive steps were taken with the experimental apparatus. With some changes in the apparatus different components were chosen and

implemented, and with other changes the same components were used, but in a different configuration. The configurations generally progressed such that different capabilities were accentuated with different configurations, ultimately arriving at an apparatus capable of exploring all of the HPRTE/VARS combined cycle attributes. There were four different build configurations: Build 1, Build 2A, Build 3, and Build 4.

### **Build 1**

Build 1 was one of the first HPRTE testing platforms utilized in this series of tests. It was the configuration used for some of the previous research work discussed in Chapter 2. A block diagram of Build 1 is shown in Figure 3-1.

The Build 1 configuration initially relied on a single, air-to-water heat exchanger to reject all of the heat from the recirculated gas line. This is the HGC shown in Figure 3-1.

Subsequently, a surrogate VARS evaporator was added to the recirculation flow path to investigate the effects of additional, low-temperature recirculation cooling. Also, new water extraction hardware was designed and built to accommodate the newly addition condensation location. The evaporator was part of a small, vapor compression refrigeration system capable of yielding about one ton (3.5 kW) of cooling. It was installed within a 0.250-inch (6.35 mm) thick steel box that previously served to house a filter. A photograph of this installation is shown in Figure 3-2.

The improvised evaporator yielded limited success in furthering the water extraction for Build 1. However, an important point was made clearer. Significant water extraction could still be attained without cooling all of the recirculated gas mixture down to its saturation temperature. The cold tubes accomplished the local cooling of gases near to the tube surfaces, and successfully condensed appreciable quantities of water.

Overall, Build 1 tests were successful in proving the concept of water extraction from the HPRTE. However, no efforts were made to pressurize this engine configuration.

## **Build 2A**

It was believed that the second phase of this research would permit pressurized engine operations, and greater gas-path cooling. Before moving prematurely to a ducting configuration incorporating a VARS, more simulated VARS cooling was used instead. This decision was influenced by the availability of two air-to-water heat exchangers in the EGDSL. These could be implemented practically, allowing more to be learned about recirculation cooling in a reasonable amount of time. This successive ducting configuration was referred to as Build 2A. A block diagram of the Build 2A configuration is provided in Figure 3-3.

Build 2A utilized two, tube-and-shell heat exchangers to reject gas-path heat to the building PCW circuit. A summative 40-50 TR (140-175 kW) was consistently removed from the recirculation line with these two coolers. This helped to demonstrate some of the concepts related to VARS integration since the means by which the recirculation gases are cooled are arbitrary. These two heat exchangers simulated the VARS vapor generator and evaporator to some extent, though the cooling medium (PCW) was different.

In addition to yielding exceptional water extraction results, the Build 2A configuration provided some valuable information about pressurized operations. It was observed that some means of throttling is necessary between the LPT inlet and LPC exit in order to pressurize. Otherwise, the exhaust gases may flow the wrong way through the LPC, out to ambient, since, depending on the ducting configuration, this can be the less resistive path. Having this fact reinforced experimentally was found useful when considering the next build configuration.

### **Build 3**

The next build configuration was called Build 3. In this configuration, one of the air-to-water heat exchangers was replaced with the vapor generator of the VARS. Also, one more heat exchanger, the CGC, was added to the recirculation line. The CGC is the evaporator in the VARS and provides the opportunity to condense more water than the previous build with a lower temperature heat transfer medium. Furthermore, Build 3 was the first configuration to utilize the new, modified Rover 1S-60 engine. The new engine was equipped with a much thicker casing made necessary by higher pressure operations. It was feared that the Rover 1S-60, as originally manufactured, would have ruptured with the greater HPC exit pressures within. Lastly, the Build 3 configuration benefited from a new Garret 4294 turbocharger. This turbocharger was chosen because it was more capable of higher pressure ratios, given the same, relatively cool recuperator exit temperature. With the previous turbocharger, models showed that pressure ratios of 2:1 were unattainable with the relatively low LPT inlet temperature. Plans were originally in place to duct some of the hot, High Pressure Turbine (HPT) exit gases around the recuperator, but the replacement of the old turbocharger with newer technology was more practical. A block diagram of the Build 3 configuration is shown in Figure 3-4.

One characteristic of the Build 3 configuration was that the LPC exit gases mixed with the recirculation gases immediately downstream of the CGC. This was beneficial in that the pressure drop between the LPC exit and HPC inlet was minimal. However, the drawback to this mixing location was that the LPC exit flow was cooled only by mixing with the cooler recirculation gases. At higher LPC pressure ratios, and LPC exit temperatures, the mixed temperature of the HPC inlet gases would be approaching the limit imposed by the manufacturer. In consequence, a move to the final configuration was made.

## **Build 4**

The final configuration, Build 4, involved only a small change in the gas path. The abovementioned LPC exit mixing location was moved to an elbow directly upstream of the CGC. By so doing, the mixed recirculated exhaust gases and fresh LPC air would all pass through the CGC together to be cooled. Initially, this may seem to be no different, in a thermodynamic sense, as the same quantity of heat is removed from the gas path whether mixing is done before or after the CGC. However, by mixing before the CGC, the flow rate, and Reynolds number passing through it increased from 60% to 100%, depending on the recirculation ratio and LPC flow rate. Moreover, the CGC inlet temperature will generally be increased by the mixing, since the LPC exit temperatures were usually higher than the WGC exit temperatures. These two effects, higher Reynolds number and higher inlet temperature, were expected to increase the effectiveness of the CGC. Thus, for the same conditions, the HPC inlet temperatures were expected to be lower for Build 4 than Build 3. A block diagram of Build 4 is shown in Figure 3-5.

## **Data Measurement**

Testing of the HPRTE/VARS combined cycle necessitated the use of various types of instrumentation. This section describes in detail all of the hardware and software used to measure and acquire experimental measurements.

### **Data Acquisition Hardware**

The Data Acquisition (DAQ) hardware is here defined as the equipment between all transducer wire terminations and the data output. Hence, there are two components that provide this throughput of information: a National Instruments chassis, and a personal computer. The purpose of the DAQ hardware is to receive the raw, analog signals from various transducers and, after filtering and amplification, convert each of them into a digital signal. From this point a

1200 MHz Personal Computer (PC) operating with 256 Mb of RAM received the digital stream and readied it for the DAQ software.

The DAQ hardware used for these experiments consisted of one chassis, four modules and four terminal blocks. The chassis is a model SCXI 1000, and provided a low-noise environment in which signal conditioning can be performed by the modules. A 50-pin cable conveyed the data to a PCMCIA card installed within the PC.

Two SCXI 1102 modules were employed for the acquisition of thermocouple signals—one for the HPRTE temperatures, and one for the VARS temperatures. The SCXI 1102 modules were equipped with 32 differential, analog channel inputs, not including one Cold-Junction-Compensation (CJC) channel. Additionally, each channel was amplified with a gain of either one or 100 at the discretion of the user. Each channel in the 1102 modules was also equipped with a three-pole lowpass filter rejecting 60Hz noise. SCXI 1300 terminal blocks were used with each of the SCXI 1102 modules for the thermocouple wire terminations.

One SCXI 1100 module was utilized to condition all of the pressure transducer, load cell, and tachometer reader signals. The SCXI 1100 also had 32 differential channels and an onboard programmable gain instrument amplifier. All channels were also equipped with a jumper-selectable (four Hz or ten kHz cutoff), single-pole filter. Wiring for this module was terminated in a SCXI 1303 terminal block.

One SCXI 1126 module was necessary for the acquisition of all instrumentation having a frequency output. It was equipped with eight isolated channels with filtering, and a software programmable frequency-to-voltage conversion circuit. This module used a SCXI 1327 terminal block for its wire terminations. Within this terminal block was a selectable 1:1 or 100:1 voltage attenuation switch for each channel.

## **Data Acquisition Software**

The software used for processing the data signals was LabVIEW 7.1. It is also a National Instruments product, and therefore interfaces very well with the DAQ hardware. LabVIEW is a graphical programming environment that allows instrumentation signals to be monitored, manipulated or scaled, and appended to a data file, all in real-time. This type of interface was essential to monitoring key parameters on both the power and refrigeration sides of the combined cycle.

## **Instrumentation**

In general, five types of measurements were made in testing the HPRTE/VARS: temperature, pressure, flow rate, rotational speed, and load. Thermocouples were exclusively used for temperature measurements. For pressure measurements, diaphragm-type pressure transducers were implemented to provide the DAQ with an analog signal. In addition to these, redundant manometers and mechanical pressure gauges were used for some of the more vital pressure measurements. Where measured directly, liquid flow rates were acquired by either turbine or paddle-wheel, self-powered flowmeters. The only rotational speed measurement, dynamometer speed, was made with an optical tachometer, and load measurements were performed with load cells.

## **Thermocouples**

Three different types of thermocouples were used for temperature measurements: J-type, K-type, and T-type. In general, the K-type, J-type, and T-type thermocouples measured hot gas, warm gas, and cool liquid temperatures, respectively. Exceptions to this are on the VARS, where T-type thermocouples were used for all temperature measurements. Most of the thermocouples were 0.250 inches (6.35 mm) in diameter, and extended to approximately the centerline of the flow path.

### **Pressure transducers**

The pressure transducers used were all Omega PX138 series sensors. These transducers employed an eight VDC power source with a one VDC to six VDC output, and were equipped with temperature compensation up to 122 °F (323 K). There were four types of differential PX138 sensors used, classified by pressure range: 0-100 psi (689 kPa), 0-30 psi (207 kPa), 0-5 psi (34 kPa), and 0-1 psi (7 kPa). All of these sensors were installed near the ceiling of the EGDSL, where shielded cables then carried their signals to the SCXI 1303 terminal block.

### **Turbine and paddle-wheel flowmeters**

The fuel flow rate measurements were made using a Hoffer Flow Controls, low-flow liquid turbine flow meter, model number MF1/2X70B. It was situated immediately downstream of the fuel tank and generated a frequency output in proportion to the volumetric flow rate. For a constant viscosity, this flowmeter establishes a linear response, which is transmitted directly into the SCXI 1327 terminal block. After correcting for an initial offset, accuracies within around 1% are typical from this instrument.

Two paddle-wheel flow meters were used to measure the volumetric flow rate of PCW—one at each header in the EGDSL. These units were manufactured by Omega Engineering, model number FP-5300. These instruments came with CPVC pipe fittings that would ensure the proper number of pipe diameters were in place, both upstream and down stream of the flowmeters. These flowmeters also generated a linear frequency output over volumetric flow rate.

### **Optical tachometer**

Dynamometer speed measurements were accomplished with a Monarch ROS-5W optical sensor and ACT-3 reader. The sensor was placed about 0.5 inches (1.3 cm) from the PTO, the circumference of which was covered with electrical tape. A single strip of reflective tape was

placed over the electrical tape, triggering the optical sensor once per dynamometer revolution. The reader displayed the dynamometer speed in the control room, but also provided a 0-5 VDC output, from which the DAQ hardware received its speed signal.

### **Load cells**

Two load cells were used during engine tests. The more important of the two was used to counter the dynamometer torque. This instrument was necessary for measuring the engine load, and in turn the net power output. The output from this load cell was interpreted and displayed by an Omega Engineering DP-145 multi-purpose reader. Unfortunately, the specifications for this particular load cell could not be located.

The second load cell was employed to measure the quantity of water being extracted from the HPRTE in real-time. A reservoir was suspended from this instrument, which was cantilevered from a small support structure. Several hoses conveyed the condensate from within the ducting into the reservoir over which they were suspended, also from the support structure. Thus, the real-time weight of the extracted water could be straightforwardly differentiated to obtain a flow rate. This particular load cell was an Omega Engineering platform load cell with a 72 lb (33 kg) capacity.

### **Gas analysis**

A Cosa 1600 IR analyzer was used to evaluate the composition of exhaust gas samples taken from the exhaust before leaving the EGDSL. It is a portable, five-gas exhaust gas analyzer. It quantifies carbon monoxide (CO), carbon dioxide (CO<sub>2</sub>), and unburned hydrocarbon (UBHC) concentrations using non-dispersive infrared technology. Diatomic oxygen (O<sub>2</sub>) and nitric oxide (NO) concentrations can also be measured using electrochemical sensors.

## **Mechanical instruments and analog readers**

The HPRTE/VARS experiments did not rely exclusively on the DAQ system for all values, but also utilized redundant sets of manually recorded data. This practice was adopted primarily to insure against the complete loss of data in the event of digital data corruption. Another benefit from practicing manual data recording stems from the fact that much of these data, particularly the pressures and differential pressures, were measured with different mechanical instruments. In these cases, the analog and digital sets of values could be compared to mutually ensure the reliability of both. However, this wasn't the case for the temperature measurements since the signal from each thermocouple bifurcated to an analog reader and the DAQ. Consequently, both values were always the same.

Each type of thermocouple had its own multiplexer and Omega DP460 reader. Thus, three multiplexer/reader pairs were implemented to display all of the HPRTE and VARS temperatures. Specifics on each of the temperature measurement locations and their respective thermocouples are provided in Table 3-1. The state points correspond with those shown in Figure 1-1.

All of the HPRTE pressure taps branched off to a redundant gauge of some sort. The more important of these pressures, deemed vital to engine health during experiments, were routed to their own individual gauge. This improved the visibility of important pressures. Other, less critical pressure hoses were each connected to one of two headers through its own valve. Each header was connected to a different Bourdon tube pressure gauge. The pressure panel operator could choose to view a specific pressure by simply opening the valve for that hose. After viewing and recording a pressure, the panel operator would then close the valve, and vent the header. The header would then be ready to receive a new pressure. Details on each of the state point gauges are shown in Table 3-2.

All of the differential pressures were treated similarly. Each differential pressure line going to a transducer also teed off to some sort of manometer. Manometers of various sizes and shapes were used, employing sundry fluids. Table 3-2 also presents the specifications for each of the manometers used, alongside the specific differential pressures for which they were used.

Lastly, the fuel flow rate utilized an additional rotameter, inline with the turbine flow meter. This device was always viewed helped validate the weak, self-powered signal of the turbine flowmeter. The rotameter outputs a mass flow rate, and is calibrated for a specific gravity of 0.835.

Table 3-1. Temperature locations and instrumentation.

State Point	Location	Thermocouple Type	Instrument Range	Expected Range of Values
0	Ambient	J	-40-1380°F (251-1022 K)	40-100°F (278-311 K)
1	LPC inlet	J	-40-1380°F (251-1022 K)	40-110°F (278-316 K)
2A	LPC exit	J	-40-1380°F (251-1022 K)	100-250°F (311-394 K)
2.9	CGC exit	J	-40-1380°F (251-1022 K)	40-120°F (278-322 K)
3	HPC inlet	J	-40-1380°F (251-1022 K)	40-120°F (278-322 K)
4	HPC exit	J	-40-1380°F (251-1022 K)	300-380°F (422-466 K)
5	HPR inlet	J	-40-1380°F (251-1022 K)	350-420°F (450-489 K)
6	HPR exit	J	-40-1380°F (251-1022 K)	580-620°F (578-605 K)
7	COMB exit	K	-320-2200°F (77-1478 K)	1300-1600°F (978-1144 K)
9	HPT exit	K	-320-2200°F (77-1478 K)	900-1200°F (755-922 K)
9.1	LPR exit	K	-320-2200°F (77-1478 K)	780-1100°F (689-866 K)
9.2	LPT inlet	K	-320-2200°F (77-1478 K)	780-1100°F (689-866 K)
9.3	WGC inlet	J	-40-1380°F (251-1022 K)	500-600°F (533-589 K)

State Point	Location	Thermocouple Type	Instrument Range	Expected Range of Values
9.4	WGC exit	J	-40-1380°F (251-1022 K)	110-185°F (316-358 K)
10	LPT exit	K	-320-2200°F (77-1478 K)	800-900°F (700-755 K)
1w	PCW supply	T	-320-660°F (77-622 K)	42-75°F (279-297 K)
2w	PCW return	T	-320-660°F (77-622 K)	42-85°F (279-303 K)
3w	PCW supply	T	-320-660°F (77-622 K)	42-75°F (279-297 K)
4w	PCW return	T	-320-660°F (77-622 K)	42-85°F (279-303 K)

Table 3-2. Pressure locations and instrumentation.

State Point	Location	Type of Instrument	Instrument Range	Expected Range of Values
0	Ambient	Internet Resource	N/A	736-788 mm-Hg
0-1	LPC inlet dP	Angle Manometer SG 0.827	0-2 in-H <sub>2</sub> O (0-4 mm-Hg)	0-2 in-H <sub>2</sub> O (0-4 mm-Hg)
0-2B	MAI dP	Angle Manometer SG 1.91	0-7 in-H <sub>2</sub> O (0-13 mm-Hg)	0-7 in-H <sub>2</sub> O (0-13 mm-Hg)
2A	LPC exit	Bourdon Tube Gauge	0-60 psig (0-414 kPa)	0-15 psig (0-103 kPa)
2.8-2.9	CGC dP	Manometer SG 1.0	0-60 in-H <sub>2</sub> O (0-112 mm-Hg)	0-48 in-H <sub>2</sub> O (0-90 mm-Hg)
3	HPC inlet	Bourdon Tube Gauge	0-60 psig (0-414 kPa)	-0.5-15 psig (-3.4-103 kPa)
4	HPC exit	Bourdon Tube Gauge	0-100 psig (0-689 kPa)	0-65 psig (0-448 kPa)
5	HPR inlet	Bourdon Tube Gauge	0-200 psig (0-1379 kPa)	0-65 psig (0-448 kPa)
6-7	COMB dP	Manometer SG 1.75	0-60 in-oil (0-197 mm-Hg)	0-50 in-oil (0-164 mm-Hg)
8	HPT inlet	Bourdon Tube Gauge	0-200 psig (0-1379 kPa)	0-60 psig (0-414 kPa)
9	HPT exit	Bourdon Tube Gauge	0-60 psig (0-414 kPa)	0-20 psig (0-138 kPa)
9.1	LPR exit	Bourdon Tube Gauge	0-200 psig (0-1379 kPa)	0-20 psig (0-138 kPa)
9.3	WGC inlet	Bourdon Tube Gauge	0-200 psig (0-1379 kPa)	0-20 psig (0-138 kPa)

State Point	Location	Type of Instrument	Instrument Range	Expected Range of Values
9.5	RCV dP	U-Tube Manometer SG 0.827	0-70 in-oil (0-109 mm-Hg)	0-65 in-oil (0-101 mm-Hg)
10	LPT exit	Bourdon Tube Gauge	0-200 psig (0-1379 kPa)	0-20psig (0-138 kPa)

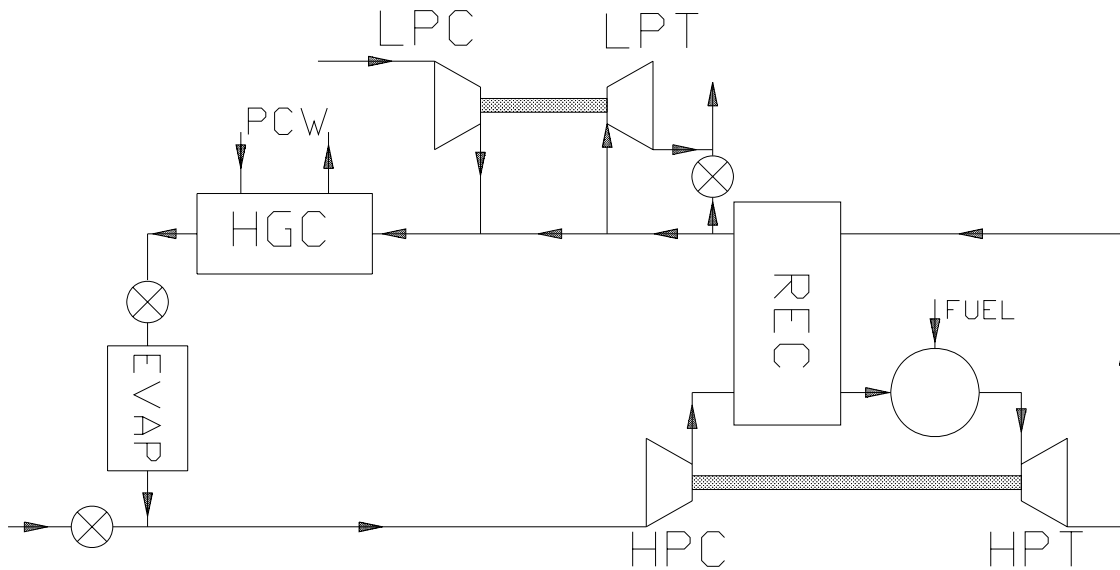


Figure 3-1. Block diagram of Build 1 configuration.

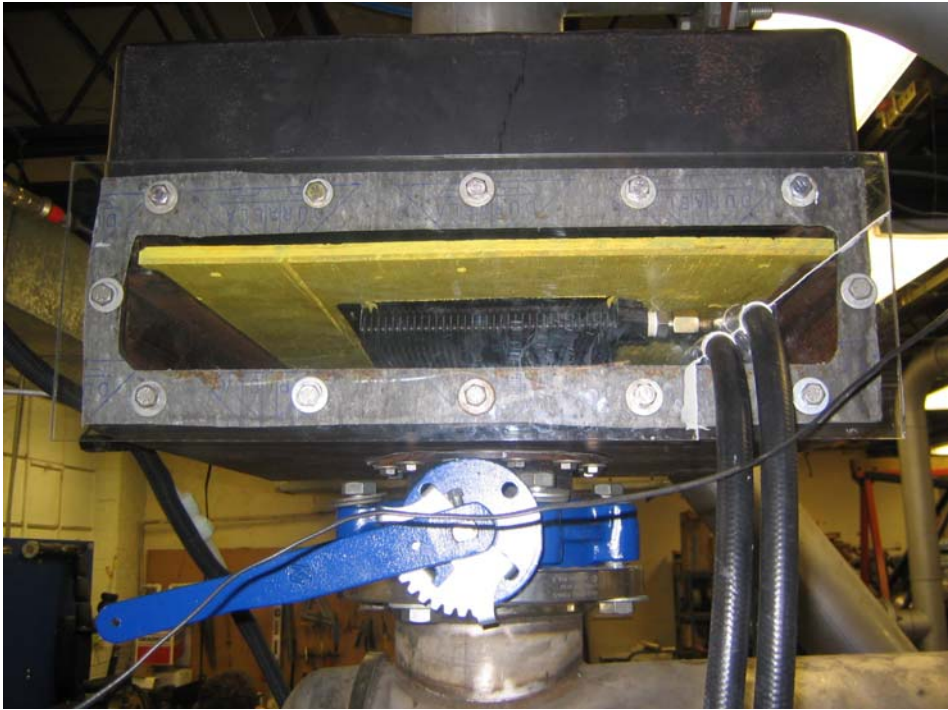


Figure 3-2. Photograph of Build 1 improvised evaporator installation.

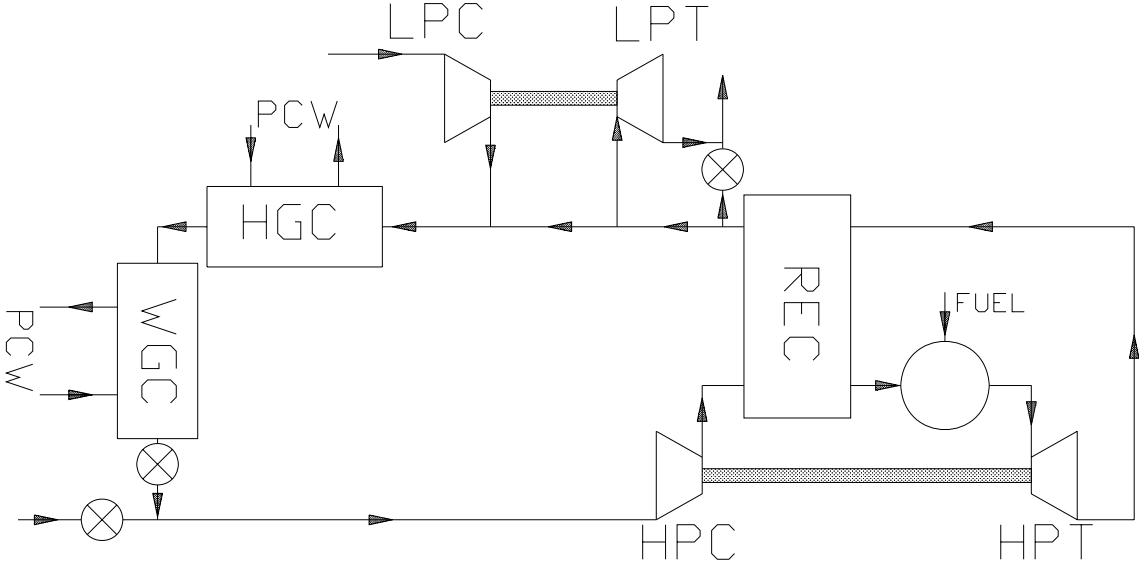


Figure 3-3. Block diagram of Build 2A configuration.



## CHAPTER 4 TEST PROCEDURES

### **Test Plan**

Before conducting an engine test, a test plan needed to be prepared so that time and fuel were not wasted making decisions during the run. First, the test plan identified the operating points to be evaluated. Then a plan was conceived to achieve each operating point since transitions into the pressurized regime were only successful after taking the proper steps in the correct order. Such a plan usually consisted of the gradual closing of the boost control valve ( $V_{EXH}$  in Figure 1-1), while carefully maintaining a reasonable recirculation ratio and fuel-to-air ratio using the recirculation valve ( $V_{REC}$  in Figure 1-1).

Contingency plans were also needed in case a particular operating point could not be reached. It was often the case, for example, that a desired pressure ratio could not be reached using the test plan. Instead of shutting down the engine and allowing the day's efforts to go to waste, it was deemed prudent to have a secondary objective for the same engine run. An example of some operating procedures is provided in Appendix A.

### **Engine/Component Preparation**

Prior to starting the HPRTE and VARS, it was essential that several, pre-planned steps be taken to ensure personnel safety, engine longevity, and data integrity. A thorough checklist was created for each engine run, and rigorously reviewed before that run. Quantities such as oil level, battery charge, PCW flow rate, etc. were confirmed as acceptable. Following these preparations, a regular startup procedure was employed in an attempt to further remove any question regarding the consistency and integrity of all engine runs. An example of these setup procedures is provided in Appendix B.

## **Instrument Preparation**

Additional actions were taken before engine runs specifically to prepare the instrumentation, DAQ hardware, and DAQ software. Some checks were made before every engine run, while others were less frequent. However, all were deemed necessary for acquiring consistent, accurate, and controlled data from the HPRTE/VARS combined cycle.

### **Transducer Offsets**

Since the DAQ hardware was equipped with CJC capabilities, there was little maintenance necessary for the thermocouple measurements. However, infrequent and random tests were employed to make certain that thermocouples were maintaining their accuracy and precision. Thermocouples were immersed in a small pool of boiling water away from the heated surface to ascertain whether or not the proper boiling temperature was being output. Thermocouples rarely deviated more than 1 °F (0.6 K) or so from the expected temperature. If one particular thermocouple was somewhat off at this temperature, then an offset was added to that signal within the DAQ software. Such a simple assessment may be flawed in that it is only performed at one temperature in the thermocouple range. It was assumed that the thermocouple linearity was retained, since calibrations at higher temperatures were not practical.

The pressure transducers also required that measures be taken to ensure consistent outputs. Periodically, the transducer calibrations were checked to verify that at least their pressure-over-voltage slope had remained the same. Any offsets in their outputs were addressed at the conclusion of engine runs, but before analysis of the data.

The linear calibration line frequently shifted up or down by a small amount. To correct for this several minutes of lead-in data were recorded before each engine startup. During the lead-in interval, all of the pressure transducers should have indicated a gauge pressure of zero. The lead-in data was averaged, and then subtracted from all subsequent data points for that engine run.

The intended result was that each pressure measured as zero psig (0 kPa) before startup and following shutdown.

The pressure transducers were powered with a variable output DC power supply. All transducer calibrations were performed with an excitation voltage of 8.11 VDC. Any drifts in this output were compensated for within the DAQ software. Before each raw voltage output was translated to a pressure, the signal was scaled according to the real-time excitation voltage (also read into the DAQ) relative to the calibration voltage. This effectively compensated and drift in the excitation voltage, since the transducer output voltages scale one-to-one with the excitation voltage.

### **Ambient Conditions**

The performance of any gas turbine engine depends greatly on the thermodynamic conditions of its environment. As such, the ambient temperature, pressure and humidity were measured or calculated. The ambient temperature was obtained from one of two J-type thermocouples. The first of these was mounted in front of the Main Air Inlet (MAI) valve ( $V_{MAI}$  in Figure 1-1). However, for most of the Build 4 engine runs this valve was closed and none of the HPRTE working fluid moved over that thermocouple. Thus, the second of these thermocouples, mounted in front of the LPC inlet bellmouth, was most often used to represent the ambient temperature. The two thermocouples usually measured different temperatures because of their locations. This resulted from the way in which air was drawn through the EGDSL. Fresh air from outdoors moved over the MAI thermocouple first, and then flowed over and around some of the hot ducting, heat exchangers, and engine surfaces before reaching the LPC inlet. Accordingly, the LPC inlet flow was a few degrees warmer than the MAI flow.

No barometers were used to directly measure the atmospheric pressure in the EGDSL. This value was obtained from the University of Florida Department of Physics Weather Station,

which publishes this data online. These values are updated every five minutes, and were recorded at the beginning and end of an engine run. The Weather Station website also stores 24 hour trends in case knowledge of barometric pressure variations during the run is desired.

The wet and dry bulb temperatures were measured directly within the EGDSL using a psychrometer. This measurement was repeated at the beginning of each trial during an engine run. At the conclusion of each run these temperatures were used with a psychrometric chart to obtain the humidity ratio and relative humidity for each trial.

## CHAPTER 5 DATA REDUCTION SCHEME

During the four months of engine testing, millions of data were acquired, along with the challenge of analyzing them. For the period of each engine run, there were 63 values being measured and recorded, once every 1.5 to two seconds. Each of these 63 pressures, temperatures and flow rates needed to be averaged, corrected where necessary, and then processed to arrive at performance parameters such as power, efficiency, heat load, etc. Thus, an algorithm was developed within the Matlab environment to carry out all of the statistical operations, and the reduction and organization of data. The methods employed to reduce the HPRTE data are detailed below. However, those measurements obtained from the VARS instruments were used exclusively for VARS operations, and were too few to suffice for a performance analysis. Consequently, only the power cycle data were analyzed.

As with any engineering analyses, some assumptions and approximations were necessary in order to have a complete set of equations. Since many of the desired performance parameters cannot be measured directly, each thermodynamic process and substance needed to be classified so that it would receive the proper treatment. Additionally, the geometric, fluid, and heat transfer properties of various components were often too complicated for the application of some analyses, further compelling the use of good engineering assumptions.

### **Gas Properties**

Given the primary role played by the working fluid in a power cycle, it is necessary to describe how these fluids are analytically treated. The HPRTE presents a unique flow path wherein many various thermodynamic processes take place: mixing of gases, power transfer to/from gases, heat transfer to/from gases, in addition to the condensation and subsequent

extraction of water. This section will describe the assumptions, approximations, and equations specific to the HPRTE gases.

### Enthalpy and Specific Heat

The working fluid within the power cycle was approximated as a thermally perfect gas, composed of N<sub>2</sub>, O<sub>2</sub>, CO<sub>2</sub>, water vapor (H<sub>2</sub>O), and CO, and as behaving in accordance with the perfect gas law shown in Equation 5.1.

$$P = \rho R_{MIX} T \quad (5.1)$$

Here the mass-specific gas constant,  $R_{MIX}$ , is computed with Equations 5.2, using knowledge (or assumed knowledge) of the chemical composition at a giving state point:

$$R_{MIX} = \frac{\bar{R}}{M_{MIX}} \quad (5.2a)$$

$$M_{MIX} = \sum_i y_i M_i \quad (5.2b)$$

where  $y_i$  represents the mole fraction of the  $i^{\text{th}}$  species being considered,  $M_i$  represents the molecular weight of the  $i^{\text{th}}$  species, and  $M_{MIX}$  represents the molecular weight of the mixture.

The variable,  $\bar{R}$ , is the universal gas constant.

For none of the calculations was the working fluid approximated as calorically perfect. Instead, a third-degree polynomial was used to obtain the constant-pressure specific heat ( $c_p$ ) of a given gas at a given temperature. The system used for obtaining  $c_p$  for one of the pure gases comprising the mixture is shown in Equations 5.3 [14].

$$\frac{c_p}{c_{po}} = 1 + a\tau + b\tau^2 + c\tau^3 \quad (5.3a)$$

$$\tau = \frac{T}{T_o} - 1 \quad (5.3b)$$

In Equations 5.3, the coefficients, a, b, and c, are particular to the pure gas being considered, and  $c_{p0}$  is the constant pressure specific heat of the pure gas at the reference temperature ( $T_0$ ) of 300K. In Equation 5.3b, T is the temperature of the pure gas, which is assumed to be the same as the mixture temperature. Following the computation of each constituent  $c_p$ , that of the gas mixture could be calculated using Equation 5.4.

$$c_{P,MIX} = \frac{1}{M_{MIX}} \sum_i y_i c_{P,i} M_i \quad (5.4)$$

The above describes only how, when necessary, the  $c_p$  was computed for a gas mixture at a single, given temperature. However, the more pertinent and more frequently occurring computations were the specific enthalpy changes ( $\Delta h$ ) within the various components. The  $\Delta h$  calculations were carried out directly by combining Equations 5.3 and integrating definitely over the measured temperature difference, per Equation 5.5.

$$\Delta h = \int_{T_{in}}^{T_{out}} c_p dT = c_{p0} \left[ T + a \left( \frac{T^2}{2T_0} - T \right) + \frac{bT_0}{3} \left( \frac{T}{T_0} - 1 \right)^3 + \frac{cT_0}{4} \left( \frac{T}{T_0} - 1 \right)^4 \right]_{T_{in}}^{T_{out}} \quad (5.5)$$

Here again, the  $\Delta h$  on the left-hand side of Equations 5.5 is for a single species within the gas mixture, and needs to be computed for each of the five constituents. Finally, the  $\Delta h$  of the gas mixture could be calculated using Equation 5.6.

$$\Delta h_{MIX} = \frac{1}{M_{MIX}} \sum_i y_i \Delta h_i M_i \quad (5.6)$$

It was often necessary to make use of an average  $c_p$  across certain of the thermodynamic processes. For example, some of the turbomachinery with large temperature differences needed an average specific heat ratio to use in efficiency calculations. For cases in which a temperature difference was measured, and  $\Delta h$  calculated, Equations 5.7 were used to obtain an average constant pressure specific heat ( $c_{P,AVG}$ ), and specific heat ratio ( $\gamma_{AVG}$ ).

$$c_{P,AVG} = \frac{\Delta h_{MIX}}{\Delta T} \quad (5.7a)$$

$$\gamma_{AVG} = \frac{1}{1 - \frac{R_{MIX}}{c_{P,AVG}}} \quad (5.7b)$$

## Gas Composition

Specialized instrumentation was employed to measure on the composition of gases throughout the HPRTE flow path. It was impractical, however, to directly measure gas samples from more than one location, because of the time needed to acquire just one sample. Consequently, assumptions were made allowing the gas composition to be followed through various, HPRTE processes effecting changes in the gas mole fractions. One substance of chief importance in this study was the content of water vapor contained within the working fluid. Since the HPRTE water extraction capability so strongly motivated this experimental endeavor, both the quantity of water extracted and the quantity *not* extracted were considered as key performance parameters.

A problem presented by the gas analyzer was that it failed to include a direct quantification of water vapor in the samples it measured. The analyzer only assessed the concentration of the following species: O<sub>2</sub>, CO<sub>2</sub>, CO, NO, and a methane equivalent of UBHCs. A persisting question was whether water vapor is considered by the machine when these concentrations are output, or if they are dry concentrations. Unfortunately, this question was never satisfactorily answered by the gas analyzer OEM, and some assumptions were necessary to complete the analysis. It was assumed that the gas analyzer provided dry concentrations, according to Equation 5.8,

$$n_{TOT} = n_{N_2} + n_{O_2} + n_{CO_2} + n_{CO} + n_{NO} + n_{UBHC} \quad (5.8)$$

where  $n_{TOT}$  represents the total number of moles being considered in a given sample. However

for this analysis, as it pertained to thermodynamic processes, the quantities of NO and UBHCs were ignored, since they were several orders of magnitude smaller than the other constituents. The CO mole fraction was also very small—less than 1%—but was retained for later service in determining combustion efficiency. Given the absence of N<sub>2</sub> concentrations from the gas analyzer output, Equation 5.9 was used to calculate the dry N<sub>2</sub> mole fraction, completing knowledge of the dry exhaust gas composition.

$$y_{N_2,DRY} = 1 - y_{O_2,DRY} - y_{CO_2,DRY} - y_{CO,DRY} \quad (5.9)$$

Attention was then turned to the estimation of water content in each of the gas analyzer samples, beginning with the assumption that the gas mixture was saturated upon reaching the analyzer. Affirming this assumption was the consistent presence of condensate droplets inside a transparent trap on the analyzer. Furthermore, this trap was consistently at or slightly above room temperature. Combined with atmospheric pressure data, the partial pressure of water vapor within the exhaust gases, P<sub>H<sub>2</sub>O</sub>, was then estimated using saturated water properties from [15, pp. 924-925], providing the water mole fraction.

$$y_{H_2O} = \frac{P_{H_2O}}{P_{ATM}} \quad (5.10)$$

Once again assuming the exhaust gases to behave as an ideal gas mixture, the summative partial pressures of the dry constituents, P<sub>TOT,DRY</sub>, was determined with Equation 5.11.

$$P_{TOT,DRY} = P_{ATM} - P_{H_2O} \quad (5.11)$$

Lastly, each of the dry mole fractions, y<sub>i</sub>, were corrected to include the water vapor, as shown in Equation 5.12,

$$y_i = \left( \frac{P_{i,DRY}}{P_{TOT,DRY}} \right) \left( \frac{P_{TOT,DRY}}{P_{ATM}} \right) \quad (5.12)$$

where  $P_{i,DRY}$  represents the partial pressure of the  $i^{\text{th}}$  dry exhaust gas constituent.

### Basic Equations and Assumptions

The overall data reduction scheme was composed of a series of analyses performed on each of the HPRTE components. In addition to the more obvious components such as compressors and heat exchangers, various sections of ducting are also analyzed as “components”, since many of these have some kind of thermodynamic process occurring within them. This section will provide a description of how each of the HPRTE components was analyzed, including equations and assumptions utilized.

#### Main Air Inlet (MAI)

The MAI admitted air to the HPRTE during startup. It is an elliptical nozzle (or bellmouth) with a 15.3 square-inch (98.7 cm<sup>2</sup>) throat area ( $A_{MAI}$ ). A pressure tap at the nozzle throat was used to measure the differential pressure,  $\Delta P_{MAI}$ , to atmosphere, and a J-type thermocouple measured the temperature of the inlet air,  $T_{MAI}$ . Atmospheric pressure and relative humidity were also measured to ensure use of the proper gas constant,  $R_{MAI}$ . While the MAI was used only as a metering device for some of the HPRTE airflow, it was closed and admitted no air for the majority of the Build 4 trials. Since the maximum Mach numbers at the throat were around 0.17 the air mass flow rate was arrived at using incompressible flow theory, and is shown below in Equation (5.8).

$$\dot{m}_{MAI} = A_{MAI} \sqrt{\frac{P_{ATM} \Delta P_{MAI}}{R_{MAI} T_{MAI}}} \quad (5.8)$$

## Low Pressure Compressor (LPC)

The LPC also employed a bellmouth at its inlet, as well as a pressure tap connected to instrumentation and a thermocouple at the inlet. The cross-sectional area of the LPC bellmouth throat is 17.7 square-inches (114 cm<sup>2</sup>). The method of calculating the mass flow rate is shown in Equation 5.9, and again derives from incompressible flow theory.

$$\dot{m}_{LPC} = A_{LPCI} \sqrt{\frac{P_{ATM} \Delta P_{LPCI}}{R_{LPCI} T_{LPCI}}} \quad (5.9)$$

The LPC power ( $\dot{W}_{LPC}$ ) was calculated using Equation 5.10:

$$\dot{W}_{LPC} = \dot{m}_{LPC} \Delta h_{LPC} \quad (5.10)$$

where  $\Delta h_{LPC}$  was computed via the methods outlined in the Gas Properties subsection above.

The efficiency of the LPC was calculated from the definition of isentropic efficiency:

$$\eta_{LPC} = \frac{PR_{LPC}^{\gamma_{LPC}-1} / \gamma_{LPC} - 1}{T_{LPCX} / T_{LPCI} - 1} \quad (5.11)$$

where  $PR_{LPC}$  is the pressure ratio across the LPC,  $T_{LPCX}$  represents the LPC exit absolute temperature, and  $T_{LPCI}$  represents the LPC inlet absolute temperature. The variable,  $\gamma_{LPC}$ , denotes the average specific heat ratio across the LPC, per the Gas Properties section above.

## Recirculation Venturi (RCV)

The RCV was used in the recirculation flow path exclusively as a metering device for the recirculating gas flow. It was situated after the WGC in a straight run of 6-inch (15 cm) ducting where the upstream pressure ( $P_{RCVI}$ ) and temperature ( $T_{RCVI}$ ) were measured, as well as the differential pressure ( $\Delta P_{RCV}$ ) from upstream of the venturi to the throat. The throat area was 6.605 square-inches (42.61 cm<sup>2</sup>). Like the two inlet bellmouths on the HPRTE, principles from incompressible flow theory were used to compute the velocity at the throat of the venturi, and in

turn, the mass flow rate. The equation used is shown in Equation 5.12,

$$\dot{m}_{RCV} = A_2 \sqrt{\frac{(P_{RCVI} + P_{ATM}) \Delta P_{RCV}}{R_{RCV} T_{RCVI}} \left[ 1 - \left( \frac{A_2}{A_1} \right)^2 \right]^{-1}} \quad (5.12)$$

where  $A_1$  and  $A_2$  are the inlet and throat areas, respectively.

A primary operating parameter, the recirculation ratio, was then defined as the ratio of recirculating gases to fresh air, as shown in Equation 5.13.

$$R = \frac{\dot{m}_{RCV}}{\dot{m}_{LPC} + \dot{m}_{MAI}} \quad (5.13)$$

### Hot Gas Cooler (HGC)

The hot-side of the HGC was bounded by two, K-type thermocouples and had approximately the same gas flow rate as that measured by the RCV. The difference in gas flow rate is small, but worth noting in Equation 5.14 as follows:

$$\dot{m}_{HGC} = \dot{m}_{RCV} + \dot{m}_{H_2O,WGC} \quad (5.14)$$

where  $\dot{m}_{H_2O,WGC}$  accounts for the water extraction from the flow path before reaching the recirculation venturi, but after the HGC. The heat load on the HGC hot side is computed as shown below.

$$\dot{Q}_{HGC} = \dot{m}_{HGC} \Delta h_{HGC} \quad (5.15)$$

No attempt was made to compute the effectiveness of this heat exchanger, as insufficient data existed on the cold side of the HGC—namely the cold side flow rate and fluid properties.

### Warm Gas Cooler (WGC)

Both the hot and cold sides of the WGC were instrumented with thermocouples. The cold-side utilized a paddlewheel flowmeter, and the hot-side flow rate was known to be the same as that of the HGC. Accordingly, both the WGC gas-side heat rate ( $\dot{Q}_{WGC,G}$ ) and water-side heat

rate ( $\dot{Q}_{WGCW}$ ) could be calculated as follows:

$$\dot{Q}_{WGC} = \dot{m}_{HGC} \Delta h_{WGC} + \dot{m}_{H_2O,WGC} h_{fg,WGC} \quad (5.16a)$$

$$\dot{Q}_{WGCW} = \rho_w \dot{V}_w c_{p,w} \Delta T_w \quad (5.16b)$$

In Equation 5.16b,  $\rho_w$  is an assumed water density of 62.4 lbm/ft<sup>3</sup> (1000 kg/m<sup>3</sup>),  $\dot{V}_w$  is the measured volumetric water flow rate in ft<sup>3</sup>/s,  $c_{p,w}$  is an assumed constant pressure specific heat for water of 0.998 Btu/lbm-R (4187 J/kg-K), and  $\Delta T_w$  is the measured temperature rise of the cooling water. In Equation 5.16a,  $h_{fg,WGC}$ , is the heat of vaporization. The heat of vaporization was found using data adapted from [15, pp. 924-925] after computing the water partial pressure, as shown below:

$$P_{H_2O} = y_{H_2O} (P_{WGC} + P_{ATM}) \quad (5.17)$$

where  $y_{H_2O}$  is the mole fraction of water vapor in the gas stream, and  $P_{WGC}$  is the inlet pressure of the WGC in units of psig. Again in Equation 5.16a,  $\dot{m}_{H_2O,WGC}$  denotes the quantity of water condensed in and extracted from the WGC. Important to note at this point is that only the total water extraction rate was directly measured—the summative water extracted from both the CGC and the WGC. Because there were no flow measurements for the individual streams, a crude, qualitative fraction was applied to the measured, total extraction flow rate, which estimated the quantity of condensate issuing from each extraction point. For example, this fraction was typically 60/40, for the WGC/CGC extraction rates.

It was most often the case that the two heat rates shown in Equations 5.16 were not equivalent. The gas-side heat rate always tended to be higher than the water-side. This was attributed to heat losses to ambient, which was straightforwardly found by adding the two heat rates.

Efforts were made to calculate the effectiveness of the WGC. The water condensation was one of the chief objectives motivating this experimental program. Thus, the proficiency of the WGC to condense water was regarded as one of the HPRTE performance parameters, and was accounted for in the effectiveness calculations, as detailed below. The effectiveness was calculated as shown,

$$e_{WGC} = \frac{\dot{Q}_{WGC}}{\dot{Q}_{\max,WGC}} \quad (5.18)$$

where  $\dot{Q}_{\max,WGC}$  is the maximum possible gas-side heat rate, as defined by Equation 5.19.

$$\dot{Q}_{\max,WGC} = (\dot{m}_{WGC,NC})\Delta h_{\max,SEN,NC} + \dot{m}_{\max,WGC,H2O} (\Delta h_{\max,SEN,H2O} + h_{fg,WGC}) \quad (5.19)$$

In Equation 5.19,  $\dot{m}_{WGC,NC}$  is the non-condensable gas flow rate,  $\Delta h_{\max,SEN,NC}$  is the change in enthalpy if the non-condensable gases are cooled to the water-side inlet temperature, and  $\dot{m}_{\max,WGC,H2O}$  is the estimated, maximum possible water extraction rate if the mixture is cooled to the cold-side inlet temperature. The variable  $\Delta h_{\max,SEN,H2O}$  represents the sensible change in enthalpy from cooling the water vapor to its initial dew-point. Again, this treatment effectively considers the flow as two separate streams—one condensable stream and one non-condensable stream—and rests on the assumption of an ideal gas mixture, even for the water near its vapor dome. Furthermore, it is understood that the interaction of the water vapor and the non-condensable stream will produce effects not captured by this analysis. Specifically, the water vapor will experience further sensible enthalpy changes below the initial dew-point, since the dew-point temperature will gradually decrease as more water is taken from the mixture.

### **Cold Gas Cooler (CGC)**

A mixing junction was situated directly upstream of the CGC where fresh air from the LPC joined with recirculating exhaust gases. Mixing junction calculations were necessary to find the

mixed, inlet temperature to the CGC, and are discussed in the Mixing Junction section later. The CGC exit temperature was acquired with a J-type thermocouple. The CGC heat rate was estimated with effectively the same equation as that used for the WGC, as shown in Equation 5.20:

$$\dot{Q}_{CGC} = \dot{m}_{RCV} \Delta h_{CGC} + \dot{m}_{H_2O,CGC} h_{fg,CGC} \quad (5.20)$$

where  $\dot{m}_{H_2O,CGC}$  represents the mass flow rate of water extracted from the CGC. Again in Equation 5.20  $h_{fg}$  appears, but has been recalculated at this point for both the reduced mole fraction of water vapor and gas pressure at this state point.

The effectiveness calculations performed for this heat exchanger were also identical to those of the WGC, shown above in Equations 5.18 and 5.19.

#### **Ducting Section 4-5**

This ducting component was defined by the ducting between the HPC exit thermocouple and High Pressure Recuperator (HPR) inlet thermocouples. A heat balance was deemed necessary for this ducting section due to the placement of the HPC exit thermocouple. The placement of this thermocouple by the OEM resulted in the measurement of HPC exit gases in the middle of an incidental heating process. Upon emerging from the diffuser, the HPC exit gases passed through an annular passage over hot, HPT inlet ducting before its egression from the engine. The result of this was significant heating between the two thermocouples defining this ducting section. This heating rate was computed using Equation 5.21:

$$\dot{Q}_{4-5} = \dot{m}_{HPC} \Delta h_{4-5} \quad (5.21)$$

where  $\dot{m}_{HPC}$  was calculated by applying the conservation of mass principle to the HPRTE, per Equation 5.22.

$$\dot{m}_{HPC} = \dot{m}_{MAI} + \dot{m}_{LPC} + \dot{m}_{RCV} - \dot{m}_{H_2O,CGC} \quad (5.22)$$

## High Pressure Compressor (HPC)

As mentioned above, there was significant heating of the gases leaving the HPC. One of the initial obstacles in characterizing the HPC performance was to determine the HPC adiabatic exit temperature. With the HPC exit thermocouple residing in the middle of this inadvertent heating, it was necessary to utilize some of the engine manufacture data on the HPC. Included within the engine documentation [16] was a uniquely formatted compressor map for the HPC that served this purpose. This map is shown in Figure 5-1, and provides the adiabatic HPC exit temperature as a function of corrected flow rate and corrected speed. The HPC inlet and adiabatic exit temperatures were then used to find its  $\Delta h$ , and in turn its work rate, as shown below.

$$\dot{W}_{HPC} = \dot{m}_{HPC} \Delta h_{HPC} \quad (5.23)$$

The HPC isentropic efficiency,  $\eta_{HPC}$ , was computed with the same equation as  $\eta_{LPC}$ , shown in Equation 5.11.

Similar to ducting section 4-5, a heat rate was defined to account for the temperature rise between the one-dimensionalized, adiabatic HPC exit and the HPC exit thermocouple. This heat rate, shown in Equation 5.24 was arbitrarily grouped among other HPC parameters and considered as a heating process immediately subsequent to compression, in order to maintain continuity of the flow path. The enthalpy change in this heating process ( $\Delta h_4$ ) was computed using the adiabatic HPC exit temperature found via Figure 5-1, and the temperature acquired by the HPC exit thermocouple.

$$\dot{Q}_4 = \dot{m}_{HPC} \Delta h_4 \quad (5.24)$$

## Combustor

The combustor presented several challenges during the formation of this data reduction algorithm. Principle among these was the less-than-ideal location of the combustor exit thermocouple. This thermocouple was situated about 14 inches (36 cm) from the flame, a radiation source approaching 3500 °F (2200 K), and only partway through the mixing of hot primary-zone gases and cool dilution gases. Moreover, for reasons discussed later, the HPT exit temperature was also difficult to ascertain, making it difficult and unreliable to back calculate the HPT inlet and combustor exit temperatures with a work balance. Thus, a different approach was adopted to estimate the combustor exit temperature as accurately as possible using the fuel flow rate, and combustor inlet conditions. Initial efforts approximated the combustor as a heater with no losses to ambient, and later evolved to estimate convective and radiative losses to ambient.

The rate of heat added to the working fluid in the combustor was estimated using Equation 5.25:

$$\dot{Q}_{COMB} = (\dot{m}_{FUEL} LHV) \eta_{COMB} - \dot{Q}_{CONV} - \dot{Q}_{RAD} \quad (5.25)$$

where LHV is the fuel lower heating value,  $\dot{Q}_{CONV}$  and  $\dot{Q}_{RAD}$  are the estimated convective and radiative rates of heat loss from the combustor to ambient. The type of fuel used for these experiments was diesel-2, and its LHV was assumed to be 18,300 Btu/lbm (42.6 MJ/kg). The combustion efficiency,  $\eta_{COMB}$ , was defined using the CO and CO<sub>2</sub> mole fractions ( $y_{CO}$  and  $y_{CO_2}$ ) obtained by the gas analyzer, and rests on the assumption that the exhaust gas composition was frozen between the combustor exit and the exhaust stack where gas samples were measured.

$$\eta_{COMB} = 1 - \frac{y_{CO}}{y_{CO_2}} \quad (5.26)$$

To estimate the two heat losses in Equation 5.25 the combustor was discretized into several sections defined by its geometric features. During engine runs, a surface probe was used to

obtain surface temperatures on the combustor. Equations 5.27 show how each of the heat losses were computed:

$$\dot{Q}_{CONV} = h \sum_i A_i (T_{SURF,i} - T_{AMB}) \quad (5.27a)$$

$$\dot{Q}_{RAD} = \varepsilon \sigma \sum_i A_i (T_{SURF,i}^4 - T_{AMB}^4) \quad (5.27b)$$

where in each case the losses from each discrete area ( $A_i$ ) and its corresponding surface temperature ( $T_{SURF,i}$ ) are summed over the surface of the combustor.  $T_{AMB}$  represents both the temperature of the ambient air and that of the radiative heat sink, and  $\sigma$  represents the Stefan-Boltzmann constant. In Equation 5.27b, the radiative heat exchange is approximated as that between two black bodies, and as such the emissivity,  $\varepsilon$ , is one. In Equation 5.27a,  $h$  is an assumed convection coefficient of about  $25 \text{ W/m}^2\text{-K}$ . Incropera and DeWitt [15, p. 8] suggest that this value is at the high end of the natural convection regime, and at the low end of the forced convection regime. The actual heat transfer environment around the combustor had a very low velocity flow passing over it, induced by the facility fans, and as such was judged as forced-free convection. In any case, the estimations obtained from Equations 5.27 were consistently less than 1% of  $Q_{COMB}$ .

Once the heat addition rate was computed from Equation 5.25, the enthalpy change of the working fluid in the combustor,  $\Delta h_{COMB}$ , was computed with Equation 5.28:

$$\Delta h_{COMB} = \frac{\dot{Q}_{COMB}}{\dot{m}_{COMB}} \quad (5.28)$$

where  $\dot{m}_{COMB}$  is simply the sum of  $\dot{m}_{HPC}$  and  $\dot{m}_{FUEL}$ . From this point, given the combustor inlet temperature, a subroutine was employed to iterate on the exit temperature until  $\Delta h$  equaled  $\Delta h_{COMB}$ . The iterative process was made necessary by the quartic polynomials, in temperature, that were used to compute  $\Delta h$  (Equation 5.5).

The equivalence ratio ( $\Phi$ ) was calculated using Equation 5.29:

$$\Phi = \frac{FA}{FA_{STOICH}} \quad (5.29)$$

where  $FA$  is the actual fuel-to-air ratio, and  $FA_{STOICH}$  is the stoichiometric fuel-to-air ratio. The fuel-to-air ratio was computed with Equation 5.30.

$$FA = \frac{\dot{m}_{FUEL}}{\dot{m}_{MAI} + \dot{m}_{LPC}} \quad (5.30)$$

It is important to note, as pointed out by Crittenden [17], that the calculations shown in Equations 5.29 and 5.30 fail to consider unburned oxygen contributions from the recirculation gases. Therefore, the combustion environment would actually be leaner than Equation 5.29 would imply, if there is recirculation flow.

### **Ducting Section 7-8**

This section of ducting exists between the combustor exit and the HPT inlet, and is characterized by its heat loss to gases exiting the HPC (Ducting Section 4-5). In a sense, these two segments of the HPRTE flow path can be viewed as an internal heat exchanger. The assumption is made both here and for Ducting Section 4-5 that this hypothetical heat exchanger is well insulated from ambient, since it is the cold-side that shares a surface with ambient air. Proceeding from this assumption, the heat lost by ducting section 7-8 is equated to the cumulative heat gained by the HPC exit gases before reaching the recuperator, per Equation 5.31.

$$\dot{Q}_{7-8} = -(\dot{Q}_4 + \dot{Q}_{4-5}) \quad (5.31)$$

The next step was to use this heat rate to find the enthalpy change,  $\Delta h_{7-8}$ ,

$$\Delta h_{7-8} = \frac{\dot{Q}_{7-8}}{\dot{m}_{COMB}} \quad (5.32)$$

and iterate to find its corresponding HPT inlet temperature, with the previously calculated combustor exit temperature.

### **High Pressure Turbine (HPT)**

As was previously mentioned, there were significant uncertainties in directly acquiring the HPT exit temperature. The OEM equipped the HPT exit with four compression fittings to accommodate four HPT exit thermocouples. These are situated around the circumference of the exhaust plane, 90 degrees apart. Specifically, the uncertainties arose from the apparent, highly stratified flow exiting the HPT. Each of the four thermocouples consistently indicated four, distinctly different temperatures differing by as much as 320 °F (178 K). Rotation of the thermocouples from one location to another confirmed that the phenomenon was particular to the temperature field around the HPT exit plane, and not the thermocouples themselves. It was believed that simply averaging the four temperatures would be a poor representation of the mixed, one-dimensional HPT exit temperature, since initial efforts to use a linear average resulted in erroneously high isentropic efficiencies ( $\eta_{HPT} > 100\%$ ). Consequently, a different approach was employed, seeing as enough information was available from elsewhere to complete the HPT analysis.

Instead of attempting to directly calculate the HPT power by means of the fluid  $\Delta h$ , a power balance was implemented, as shown in Equation 5.33:

$$\dot{W}_{HPT} = -\dot{W}_{HPC} - \dot{W}_{DYNO} - \dot{W}_{LOSS} \quad (5.33)$$

where  $\dot{W}_{DYNO}$  is the power absorbed and measured by the dynamometer, and  $\dot{W}_{LOSS}$  represents the power consumed by friction and pumps within the engine. The power losses were provided by the OEM [16] for each of components internal to the core engine: fuel pump, oil pump, bearing friction, and rotor friction. In addition, the total power loss data was conveniently added

by the manufacturer. All of these losses are shown as a function of rotor speed, and can be seen in Figure 5-2. A built-in Matlab function was utilized to interpolate from the total power loss curve using a cubic spline interpolation method.

The dynamometer power was calculated using measurements acquired from a load cell that countered the engine torque. For convenience, a straightforward equation was provided [16] by the dynamometer manufacturer, as shown below:

$$\dot{W}_{DYN} = \frac{F_{DYN} \omega_{DYN}}{4500} \quad (5.34)$$

where  $F_{DYN}$  and  $\omega_{DYN}$  are the force (in pounds) acquired by the load cell, and dynamometer speed (in rpm), respectively. The number in the denominator is the dynamometer constant, and accounts for the length of the dynamometer moment arm, and also for unit conversions such that  $\dot{W}_{DYN}$  is in units of horsepower.

Having found the HPT power, and with knowledge of the HPT flow rate, the enthalpy change across the HPT ( $\Delta h_{HPT}$ ) could then be computed with Equation 5.35.

$$\Delta h_{HPT} = \frac{\dot{W}_{HPT}}{\dot{m}_{COMB}} \quad (5.35)$$

Again with the component inlet temperature as a starting point, an iterative subroutine was used with  $\Delta h_{HPT}$  to find the HPT exit temperature. Upon calculation of the HPT exit temperature, the HPT isentropic efficiency was computed using Equation 5.36:

$$\eta_{HPT} = \frac{1 - T_{HPTX} / T_{HPTI}}{1 - PR_{HPT}^{1/\gamma_{HPT}}} \quad (5.36)$$

where  $T_{HPTI}$  and  $T_{HPTX}$  are the HPT inlet and exit absolute temperatures, respectively. The

variable,  $\gamma_{HPT}$  represents the average specific heat ratio across the HPT, and  $PR_{HPT}$  is the HPT pressure ratio defined in Equation 5.37.

$$PR_{HPT} = \frac{P_{HPTX} + P_{ATM}}{P_{HPTI} + P_{ATM}} \quad (5.37)$$

## Recuperator

For most of the Build-4 engine runs the recuperator was well insulated with a two-inch (5 cm) thick, ceramic blanket on top of another thin, fiberglass wrap. This effort was primarily made to simplify the data reduction algorithm, reducing or eliminating the difficult-to-ascertain heat loss to ambient from the recuperator. The surface temperature of the insulation was measured during engine runs, and a rudimentary analysis confirmed that losses to ambient were typically three to four percent of the heat transfer rate between the hot and cold streams. Nonetheless, the estimation of heat losses through the insulation was retained in the analysis.

For engine runs with the insulation in place, the hot-side heat rate calculation is shown in Equation 5.38 using the cold-side heat rate and the abovementioned heat rate to ambient:

$$\dot{Q}_{R,HOT} = -\dot{Q}_{R,COLD} + \dot{Q}_{R,AMB} \quad (5.38)$$

where  $\dot{Q}_{R,AMB}$  represents the heat losses to ambient, and  $\dot{Q}_{R,COLD}$  is the recuperator cold-side heat rate, computed with Equation 5.39,

$$\dot{Q}_{R,COLD} = \dot{m}_{HPC} \Delta h_{R,COLD} \quad (5.39)$$

where  $\Delta h_{R,COLD}$  was calculated with the two well-placed thermocouples bounding the cold-side of the recuperator. Similar to the combustor heat losses to ambient, the recuperator  $\dot{Q}_{R,AMB}$  was calculated by breaking the recuperator into three discrete areas and surface temperatures, and then applying Equation 5.40.

$$\dot{Q}_{R,AMB} = -h \sum_{i=1}^3 A_i \Delta T_i \quad (5.40)$$

The enthalpy change across the recuperator hot side was then calculated using Equation 5.41,

$$\Delta h_{R,HOT} = \frac{\dot{Q}_{R,HOT}}{\dot{m}_{COMB}} \quad (5.41)$$

which in turn enabled the recuperator hot-side inlet temperature (also the HPT exit temperature) to be re-calculated using the recuperator hot-side exit temperature. This new HPT exit temperature was compared to the previously calculated value to make sure they corresponded satisfactorily. From this point, the HPT exit temperature was used with  $\Delta h_{HPT}$  to again make redundant calculations of HPT inlet and combustor exit temperatures and ensure agreement with the previously calculated values.

For engine runs that took place before the insulation was utilized a slightly different method was employed. Due primarily to the large variations in the recuperator surface temperature, the heat rate to ambient was estimated with much less confidence. Additionally, this heat loss was considerably larger, and as such its uncertainty would weigh more heavily on the uncertainty of the hot-side heat rate. For this reason, redundant calculations were not made in these cases, and the recuperator hot-side heat rate was computed with Equation 5.42,

$$\dot{Q}_{R,HOT} = \dot{m}_{COMB} \Delta h_{R,HOT} \quad (5.42)$$

where in this case  $\Delta h_{R,HOT}$  was found using the previously calculated HPT exit temperature and the measured hot-side recuperator exit temperature. The ambient heat losses for the uninsulated cases were found by summing the hot-side and cold-side heat rates.

Lastly, the recuperator effectiveness was computed using Equation 5.43.

$$\varepsilon = \frac{\dot{Q}_{R,COLD}}{\dot{Q}_{R,MAX}} \quad (5.43)$$

Due to its lower average temperature and specific heat, the cold stream consistently had the lower heat capacity rate. Therefore, the cold-side stream is the only one that can achieve the maximum  $\Delta h$ , and the maximum heat transfer rate is defined in Equation 5.44,

$$\dot{Q}_{R,MAX} = \dot{m}_{HPC} \Delta h_{R,MAX} \quad (5.44)$$

where  $\Delta h_{R,MAX}$  was found using the recuperator cold-side and hot-side inlet temperatures.

### **Low Pressure Turbine (LPT)**

No flow rate measurements were practical given the ducting arrangement of the LPT, only pressures and temperatures at the LPT inlet and exit were acquired. However, a power balance with the LPC made a LPT flow rate estimate possible. This was accomplished by assuming a mechanical energy conversion efficiency,  $\eta_{MECH}$ , of 0.97 between the two, allowing the LPT work rate to first be estimated, as shown in Equation 5.45.

$$\dot{W}_{LPT} = \frac{-\dot{W}_{LPC}}{\eta_{MECH}} \quad (5.45)$$

After calculation of the enthalpy change across the LPT ( $\Delta h_{LPT}$ ) the LPT flow rate was estimated using Equation 5.46.

$$\dot{m}_{LPT} = \frac{\dot{W}_{LPT}}{\Delta h_{LPT}} \quad (5.46)$$

A LPT map plotting corrected flow rate over LPT pressure ratio was also available to provide a redundant flow rate estimate. The two values consistently agreed satisfactorily with one another.

The LPT isentropic efficiency was calculated using Equation 5.36 with LPT pressures and temperatures substituted.

### **Mixing Junctions**

There were several mixing junctions in the HPRTE flow path. Only one of these, however, required an energy balance to find the mixed exit temperature. This mixing junction

existed just upstream of the CGC, where the LPC exit gases mix with recirculation gases issuing from the WGC. In this case, the mixing process was treated as adiabatic. Furthermore, the temperatures and specific heats of the two inlet streams were close enough to one another to justify the approximation of constant specific heats. Used here only, this approximation permitted the temperature of the exit stream to be straightforwardly found using Equation 5.47, which presents the calculation using generalized variables.

$$T_3 = \frac{2(\dot{m}_1 c_{p,1} T_1 + \dot{m}_2 c_{p,2} T_2)}{(\dot{m}_1 + \dot{m}_2)(c_{p,1} + c_{p,2})} \quad (5.47)$$

In Equation 5.47, the subscript, 3, denotes a variable pertaining to the mixed, exit stream, and the subscripts 1 and 2 denote variables pertaining to the two inlet streams. The specific heat of the mixed, exit stream is approximated as the linear average of the two inlet streams' specific heats.

Changes in gas composition were also tracked across mixing junctions. It should be pointed out that water extraction locations were also classified as mixing junctions. Although there was no mixing taking place, per se, a sort of “un-mixing” of fluids was occurring. Inclusion of water extraction locations with the more typical mixing junctions allowed use of the same equations, generalized for gas composition bookkeeping. The mass flow rate leaving a mixing junction was plainly found with Equation 5.48:

$$\dot{m}_3 = \dot{m}_1 \pm \dot{m}_2 \quad (5.48)$$

where the sign of the second mass flow rate is determined by whether the fluid stream is entering or exiting the mixing junction. Where in Equation 5.47 the subscripts 1 and 2 denoted the two *inlet* streams, they shall henceforth denote the two *known* streams, since information about these two streams is known, and information pertaining to stream 3 is unknown. Next, the molecular weights of the two known streams ( $M_{1,2}$ ) were computed using Equation 5.2b and the mole flow rates of all three were found using Equations 5.49:

$$\dot{n}_{1,2} = \frac{\dot{m}_{1,2}}{M_{1,2}} \quad (5.49a)$$

$$\dot{n}_3 = \dot{n}_1 \pm \dot{n}_2 \quad (5.49b)$$

where again, in Equation 5.49b, the sign of the second known stream depends whether it's mixing with stream 1, or exiting the flow path. From here, the mole flow rates of each stream were multiplied with their corresponding vector of mole fractions to obtain mole flow rates of each pure substance within each of the known streams, as shown below.

$$\begin{bmatrix} \dot{n}_{N_2} \\ \dot{n}_{O_2} \\ \dot{n}_{CO_2} \\ \dot{n}_{H_2O} \\ \dot{n}_{CO} \end{bmatrix}_{1,2} = \dot{n}_{1,2} \begin{bmatrix} y_{N_2} \\ y_{O_2} \\ y_{CO_2} \\ y_{H_2O} \\ y_{CO} \end{bmatrix}_{1,2} \quad (5.50)$$

Finally, the mole flow rates from the known streams were used to find the mole fraction vector of the unknown stream, as seen in Equation 5.51.

$$\begin{bmatrix} y_{N_2} \\ y_{O_2} \\ y_{CO_2} \\ y_{H_2O} \\ y_{CO} \end{bmatrix}_3 = \frac{1}{\dot{n}_3} \begin{bmatrix} \dot{n}_{N_2} \\ \dot{n}_{O_2} \\ \dot{n}_{CO_2} \\ \dot{n}_{H_2O} \\ \dot{n}_{CO} \end{bmatrix}_1 \pm \frac{1}{\dot{n}_3} \begin{bmatrix} \dot{n}_{N_2} \\ \dot{n}_{O_2} \\ \dot{n}_{CO_2} \\ \dot{n}_{H_2O} \\ \dot{n}_{CO} \end{bmatrix}_2 \quad (5.51)$$

In the special case of water extraction locations, the sign in front of stream 2 was negative, and the mole fraction vector elements of stream 2 were all zero, except for the fourth element, which was one.

### Propagation of Uncertainty

In addition to reducing and interpreting the experimental data, a thorough propagation of uncertainty analysis was performed. To complete the uncertainty analysis, classical methods were employed as presented by Holman [18]. For a given dependent parameter, R, with n

independent parameters as shown in Equation 5.52,

$$R = f(x_1, x_2, \dots, x_n) \quad (5.52)$$

the uncertainty of R was computed using Equation 5.53,

$$\omega_R = \left[ \left( \frac{\partial R}{\partial x_1} \right)^2 \omega_{x_1}^2 + \left( \frac{\partial R}{\partial x_2} \right)^2 \omega_{x_2}^2 + \dots + \left( \frac{\partial R}{\partial x_n} \right)^2 \omega_{x_n}^2 \right]^{1/2} \quad (5.53)$$

where  $\omega_{x_n}$  is the uncertainty of the  $n^{\text{th}}$  independent parameter. Equation 5.53 was applied to find the uncertainty of all the parameters discussed in the above section.

All uncertainties of reduced parameters stemmed from one of three possible sources: instrumentation error, data acquisition error, and miscellaneous transient behavior, either real or artifact. This concept is generalized by Equation 5.54.

$$\omega_X = \omega_{X,INST} + \omega_{X,DAQ} + \omega_{X,TRAN} \quad (5.54)$$

Ideally, all three sources would be comparable and small. However, it is believed that the three contributions usually differed considerably, and were most frequently dominated by the third term. Typically, data were collected over a period ranging from five minutes to 15 minutes, and during this time nearly all of the temperatures, pressures, and flow rates either climbed, fell, or fluctuated to some degree. Since the objective was to characterize a single, steady operating point by averaging several hundred data points, many of the uncertainties were often taken as one standard deviation from the mean. For some parameters, such as ambient temperature, there was very little fluctuation aside from some noise in the signal. In such cases, the uncertainty in the instrument itself was the dominating source of error.

Error derived from the AD conversion of signals was considerably smaller than the other two sources. 16-bit resolution was used within the DAQ system to curb quantization errors, and the time between samples was sufficiently large to avoid any appreciable aperture errors.

Occasional testing was also carried out to spot-check for significant non-linearity errors made by the AD conversion.

In general the uncertainty of all the measured values was taken to be the greater of the instrument error and one standard deviation from the mean value. Only one standard deviation was thought necessary because the data were typically skewed by relatively few outliers. These outliers could result from several occurrences, e.g. the momentary loss of a thermocouple signal, or indeterminate electromagnetic interference. The dynamometer water supply pressure would also fluctuate erratically due to other plumbing loads in the building. This often caused brief excursions in the engine load, engine speed, fuel flow rate, and other parameters as well.

Instrument uncertainties for thermocouples, pressure transducers, and other instruments can be found in Table 5-1.

### **Data Adjustments**

The reduced data described in the above sections were obtained from a very particular engine and combination of components. Consequently, some of the capabilities of this combined cycle were veiled by excessive pressure drops, poor VARS performance, and high ambient/PCW temperatures. In addition, comparisons between these experimental results and other experiments or models needed to be made on the same basis. For these reasons, classical, partially non-dimensional parameters were used to present the data in a properly scaled form. The corrected parameters chosen are explained in greater detail by Volponi [19], and are shown in Table 5-2.

As mentioned above, the pressure drops in the HPRTE ducting was high enough to obscure the experimental results. Specifically, when transitioning into the pressurized regime, the HPT was initially back-pressured in order to accelerate the LPT. This resulted in a premature increase in the HPT exit and inlet temperatures, such that very little or no margin was left for loading the

engine by the time the LPC exit pressure rose appreciably. Furthermore, various leaks in the ducting and engine casing intensified with increasing boost due to the increased pressure within, resulting in an un-metered loss of working fluid. Consequently, nearly all of the pressurized data sets were at or near maximum HPT inlet temperatures, and at reduced engine speeds with no load on the dynamometer, resulting in an uninformative scatter of net power around zero. This necessitated a supplementary modeling approach to approximate the net power if the pressure drops had been different, since in reality this can be an arbitrary design choice.

### **Pressure Drop Considerations**

In the interest of better evaluating the HPRTE performance, several adjustments were made to the raw data, and a supplementary modeling approach was employed. In this modeling approach, the empirical pressure drops in the recirculation flow path and within the recuperated engine. This provided an upper-bound estimate of HPRTE power and efficiency in the absence of any pressure drops. The first pressure adjustment reduced the hot-side recuperator and recirculation pressure drops to zero by setting the HPT exit pressure equal to the HPC inlet pressure. The second adjustment eliminated the core-engine pressure drop by raising the HPT inlet pressure to the HPC exit pressure.

The above adjustments translate to increased net power in that the HPT pressure ratio is increased, resulting in a greater temperature ratio and temperature difference. The new HPT expansions began from the same temperatures, but were completed at lower temperatures. The lower HPT exit temperatures were calculated by assuming the HPT efficiency to be constant in all cases. Though no maps were available for this turbine, this was judged as a fair approximation when considering a map generated by AXOD [20] in Figure 5-3. There it can be seen that the HPT efficiency is approximately 85% for a wide range of corrected speeds and pressure ratios bounding the range of values seen in experiments. The adjusted HPT exit

temperature was computed using Equation 5.55,

$$T_{HPTX} = T_{HPTI} \left\{ 1 - \eta_{HPT} \left[ 1 - \left( \frac{P_{HPTX}}{P_{HPTI}} \right)^{\gamma_{HPT} - 1 / \gamma_{HPT}} \right] \right\} \quad (5.55)$$

where  $\eta_{HPT}$  is 0.85. Having estimated the adjusted HPT exit temperature, the adjusted net work output from the HPRTE was computed using Equation 5.56.

$$\dot{W}_{NET} = \dot{m}_{COMB} \Delta h_{HPT} - \dot{W}_{HPC} \quad (5.56)$$

In the interest of further generalizing the reduced results, it can also be seen from Equation 5.56 that the friction work has been ignored in this computation. The HPC work term,  $\dot{W}_{HPC}$ , was calculated using Equation 5.23.

Table 5-1. Uncertainty of instruments

Instrument	Uncertainty
T-Type Thermocouples	Greatest of 0.9 °F (0.5 K) or 0.4%
J-Type Thermocouples	Greatest of 2.0 °F (1.1 K) or 0.4%
K-Type Thermocouples	Greatest of 2.0 °F (1.1 K) or 0.4%
0-30 Pressure Transducers	0.1% of F.S. (typical), 0.5% (max)
0-100 Pressure Transducers	0.1% of F.S. (typical), 0.5% (max)
Differential Pressure Transducers	0.1% of F.S. (typical), 0.5% (max)
Chilled Water Flowmeters	0.5%
Fuel Flowmeter	1.0%
Water Extraction Load Cell	0.2 % of F.S.
Dynamometer Load Cell	Unknown
Engine Speed Optical Tachometer	3 rpm

Instrument	Uncertainty
Gas Analyzer	UBHC: 20 ppm CO: 0.03% CO <sub>2</sub> : 0.6% O <sub>2</sub> : 0.2% NO: 10 ppm

Table 5-2. Data scaling parameters [19].

Parameter	Corrected Parameter
Rotor Speed	$N^* = \frac{N}{\sqrt{\theta}}$
Gas Mass Flow Rate	$\dot{m}^* = \frac{\dot{m}\sqrt{\theta}}{\delta}$
Power	$\dot{W}^* = \frac{\dot{W}}{\delta\sqrt{\theta}}$
Temperature	$T^* = \frac{T}{\theta}$
Pressure	$P^* = \frac{P}{\delta}$

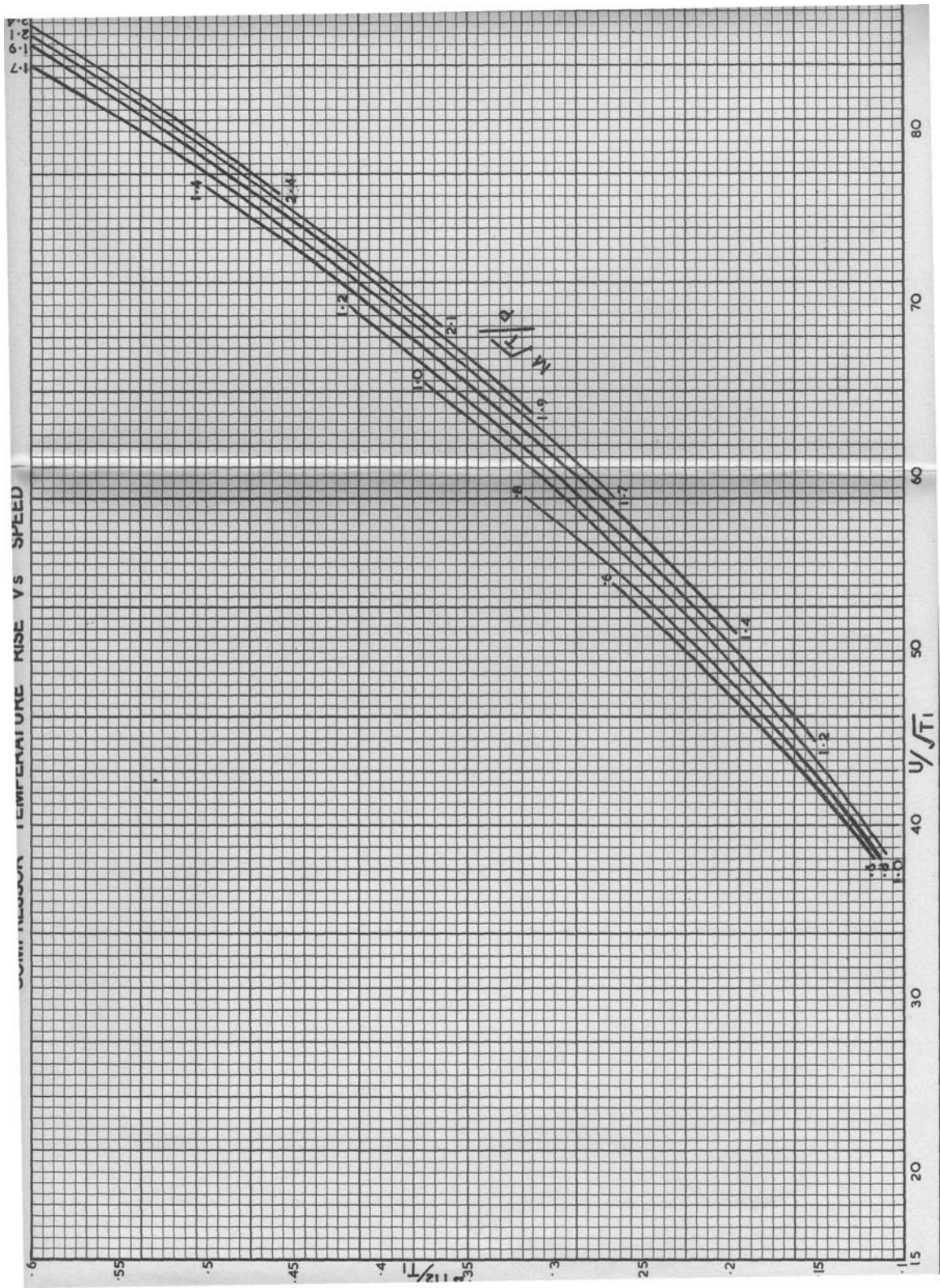


Figure 5-1. Map used for finding the HPC adiabatic exit temperature, shown as a function of corrected flow rate and corrected speed [16].

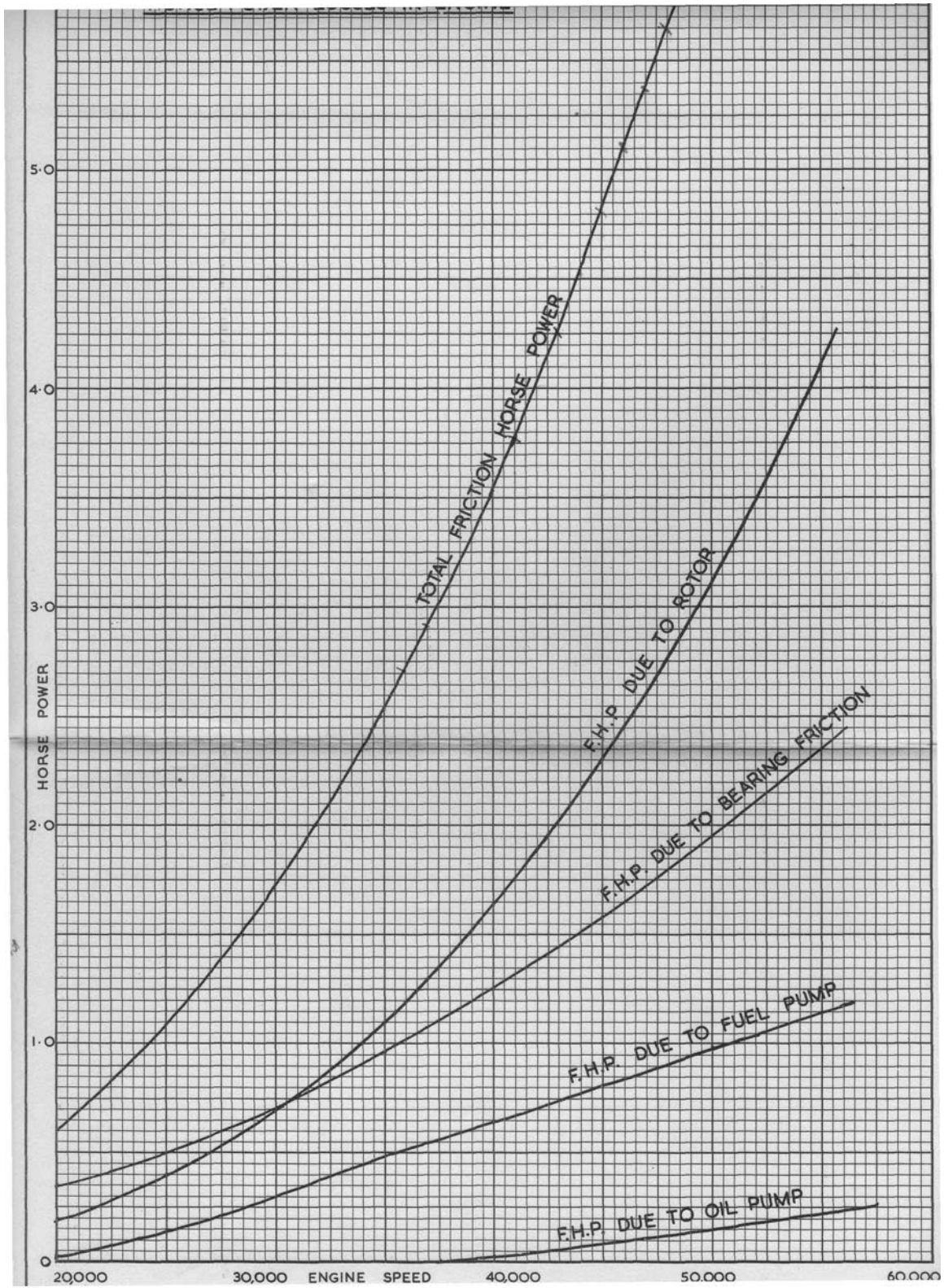


Figure 5-2. Rover 1S-60 internal power losses as a function of rotor speed [16].

### Rover Turbine Efficiency Map

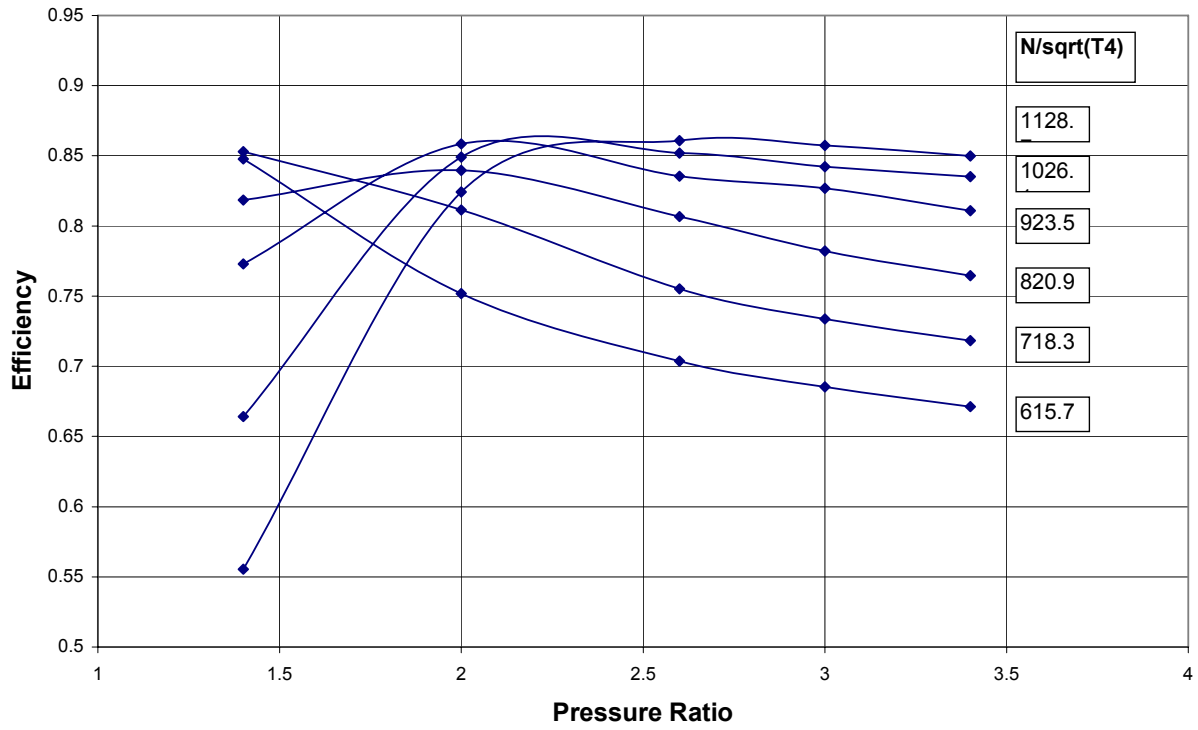


Figure 5-3. Rover 1S-60 turbine map generated by AXOD [20].

## CHAPTER 6 EXPERIMENTAL RESULTS

The experimental apparatus described in Chapter 3 was operated according to the procedures discussed in Chapter 4 on 13 occasions to yield 34 distinct sets of working data. The data reduction algorithm outlined in Chapter 5 was then applied to the data, providing the relevant performance parameters. As was mentioned in Chapter 5, all but five of these data sets were idle runs, this was due primarily to excessive pressure drops and a slightly mismatched turbocharger. Since no load was applied to the dynamometer, the resulting data—specifically the net power and efficiency—were less informative, as shown in Figure 6-1. Since the engine was in a sense loaded by back-pressuring the HPT, the steps outlined at the end of Chapter 5 were taken to estimate the power consumed by the various loss mechanisms and present the adjusted power. All of the adjusted, reduced data generated by the methods discussed in Chapter 5 are tabulated in Appendix C. Worth noting is that all of the data sets were at or near the maximum sustainable HPT inlet temperature, and as such represent full power engine runs, while other operating parameters such as recirculation ratio and LPC pressure ratio were varied. For conciseness the values previously referred to as adjusted power will henceforth be referred to as power, since it is the only power of interest.

Gas turbine engines exhibit a particularly strong dependence on ambient conditions, namely pressure, temperature, and humidity. However the HPRTE is unique in that the inlet pressure of the core engine can be changed by controlling the LPC pressure ratio. Furthermore, when coupled with the VARS, the HPC inlet temperature can also, in principle, be changed at the will of designers and operators. For these reasons,  $\theta$  and  $\delta$ , the classical correction parameters defined in Table 5-2, were calculated using the HPC inlet conditions instead of the

ambient conditions, since ambient conditions possess little influence over the HPRTE performance.

Although most turbine engines, including the Rover 1S-60, have the capability of operating at various speeds, no attempts were made in these experiments to capture data at off-design speeds. However, as the HPT was back-pressured and the turbocharger accelerated, there was significant speed-droop resulting from the mechanical governor, which helps to validate the idea that the engine was, in effect, being loaded. Additionally, the corrected speed ( $N^*$ ), defined in Table 5-2 showed even greater variance, since the HPC inlet temperature fluctuated as well. Since  $N^*$  refers performance parameters to standard ambient conditions, it was used as a dependent parameter in place of engine speed ( $N$ ). In the interest of characterizing the performance of this engine, several plots were generated. The first of these is Figure 6-2, which plots corrected power ( $P^*$ ) and thermal efficiency against  $N^*$ . Also included within Figure 6-2 is the adjusted power before inlet-condition corrections ( $P$ ). A peculiar characteristic of the  $P$  and  $P^*$  data is that they have opposite slopes when plotted over  $N^*$ . This results from the fact that the scaling parameters generally demonstrated a dependence on engine speed. Ideally, any range of HPC inlet pressures and temperatures could be actualized at any operating point (any  $N^*$  for example), but due to the operational boundaries of the engine and VARS, these inlet conditions were coupled with engine speed.

The scaling parameters,  $\theta$  and  $\delta$ , are shown over  $N^*$  in Figure 6-3 for comparison with Figure 6-2. It can be seen in Figure 6-3 that both scaling parameters increase when decreasing  $N^*$ . In the case of  $\delta$ , this trend is more straightforward. The higher LPC pressure ratios (essentially the same values as  $\delta$ ) were attained only at lower engine speeds, because increased operation of the turbocharger directly caused the speed-droop, as described in the Data

Adjustments section of Chapter 5. The  $\theta$  trend also appears to follow speed, but more directly correlates with LPC pressure ratio, with some random fluctuations as well. Again, as the turbocharger was accelerated, greater flow rates were diverted from the exhaust and driven through the LPT and through the recirculation flow path. In addition, as the HPT back-pressure initially rose, the HPT pressure ratio decreased until the LPC could be accelerated enough to compensate, increasing the HPC inlet pressure. This caused the exhaust gas temperature (EGT) to climb. As the engine speed dropped, the HPT pressure ratio continued to fall as well, further increasing EGT. These two consequences of pressurization—increased recirculation flow and temperature—combined with one another to greatly increase the heat load on the VARS generator (the HGC) in particular, but on the WGC and CGC also. The resulting heat loads taxed the VARS and the WGC exceedingly and always effected an increase in HPC inlet temperatures. Thus,  $\theta$  tended to scale with LPC pressure ratio, and in turn speed. The relationship between  $\theta$  and LPC pressure ratio is shown in Figure 6-4. When considering the trends in Figure 6-3, it is important to point out that  $\theta$  itself appears in the  $N^*$  parameter as shown in Table 5-2. As a result, the obvious decrease in  $N^*$  when decreasing  $N$  is compounded by the related upsurge in HPC inlet temperature.

After considering the trends of the correction parameters relative to  $N^*$ , the opposite slopes of  $P$  and  $P^*$  can be better understood. Since both  $\theta$  and  $\delta$  appear in the denominator of  $P^*$ , and both have downward slopes over  $N^*$ , it is more reasonable to expect the results shown in Figure 6-2 provided the denominator of  $P^*$  ( $\delta\sqrt{\theta}$ ) changes faster than its numerator ( $P$ ). In general,  $P$  would be expected to scale one-to-one with HPC inlet pressure such that a given increase in  $\delta$  would be accompanied by an equivalent increase in  $P$ . However, competing effects somewhat

mitigated the desired power-pressure relationship. Power is plotted against LPC pressure ratio in Figure 6-5.

Figure 6-5 shows the power obtained from the adjusted data, as well as the power predictions of a model developed by Khan [8, 12]. The model is a steady-state, one-dimensional thermodynamic model of the HPRTE/VARS. The adjusted experimental power and modeled power differ significantly, as seen in Figure 6-5. An initial, sharp rise in P is observed over LPC pressure ratio, but a weaker dependence at higher pressure ratios. The modeled results, however, predict a steady, linear increase in power over LPC pressure ratio. The magnitude of power predicted by the model is most likely lower due to the inclusion of friction, parasitic horsepower, and pressure drops by Khan, in an effort to most accurately represent this engine and its configuration. The adjusted power, shown in blue, was an upper-bound estimate using neither pressure drops nor friction power. The anticipated rise in P is more directly related to the engine mass flow rate, which itself depends on the HPC inlet pressure assuming the inlet temperature is held fast by the VARS. In actuality the inlet temperatures crept up with the higher LPC pressure ratios (Figure 6-4), lessening the density and potential mass flow rate, although this was a weak effect. A more prevailing detraction from the potential flow rate was the speed-droop also associated with higher inlet pressures (Figure 6-3). The deceleration of both the HPC and HPT caused a diminution in the flow rate through, and pressure ratio across each. With the reduced pressure ratios came also the reduction of temperature ratios, and therefore smaller temperature differences across the high pressure turbomachinery. In consequence, while the mass flow rate did manage to rise alongside of the LPC pressure ratio, the HPC and HPT temperature differences dropped. Figure 6-6 illustrates these opposing trends in a dimensional sense, while Figure 6-7 shows the same data, but normalized. The mass flow rate data in Figure 6-7 are

normalized by their minimum, and the delta-T data by their maximum. In this way the percent changes in each of these parameters can be viewed, and the slopes compared. It can be seen in Figure 6-7 that despite the abovementioned mitigating factors, the percent increase in mass flow rate was greater than the decline in turbomachinery temperature differences. The manner in which these parameters influence power can be seen in Equations 5.56 and 5.23. Another suspicion that can be verified in Figure 6-7 is that the mass flow rate increase was less than expected. This is realized by noting that the slope of percent-change-in-flow-rate regression line indicates only an 84% increase in flow rate, per unit increase in LPC pressure ratio. Again, with ideal hardware and control schemes, an approximate 100% increase in flow per unit LPC pressure ratio increase is expected.

The engine mass flow rate and corrected mass flow rate are shown over  $N^*$  in Figure 6-8 for comparison with Figure 6-2. The trends in Figure 6-8 are similar to those in Figure 6-2 in that the uncorrected values bear a downward slope and the corrected values an upward slope. This comparable behavior can in like fashion be explained by the relationship  $\theta$  and  $\delta$  exhibit with  $N^*$ . One difference to be noted is the relatively gentle slope of corrected flow rate over  $N^*$ , where  $P^*$  demonstrated a much closer relationship with  $N^*$ . However,  $\theta^{0.5}$  appears in the numerator of the corrected flow rate parameter, and in the denominator of the corrected power parameter. Thus the downward trend of  $\theta$  with increasing  $N^*$  serves to somewhat lessen the impact of  $\delta$  instead of augmenting it, as was so for  $P^*$ . Thus a greater mass flow rate (and  $\theta$ ) at lower speeds was more than balanced by the greater HPC inlet pressure.

Having considered the dependence upon inlet conditions and mass flow rate, other non-dimensional parameters and their effects on power were also explored. In particular, two cycle parameters were thought to have a significant bearing on power: the HPC pressure ratio, and the

overall Cycle Temperature Ratio (CTR). The CTR is defined as the ratio of the maximum, absolute cycle temperature (HPT inlet temperature) to minimum absolute cycle temperature (HPC inlet). These parameters' influence can most easily be understood by examining a temperature-entropy (T-S) diagram with an ideal Brayton cycle, shown in Figure 6-9.

The diagram in Figure 6-9 shows all temperatures normalized to the inlet temperature such that CTR appears on the ordinate. Three different cycles are shown on the T-S plot for comparison: a baseline cycle, a higher CTR cycle at the same pressure ratio as baseline, and a higher HPC pressure ratio at the same CTR as baseline. The baseline cycle follows the path 1-2-3-4, and the power-per-unit-mass is equivalent to the area contained by the cycle, areas A plus B. The second cycle follows the path 1-2-5-6, and clearly yields a significantly higher specific power with areas A, B, and C. The third cycle follows the path 1-7-8-9. This cycle differs in that it adds to the specific power with area D, but subtracts from specific power by surrendering area B. In general, there will be a net gain in specific power, but a cycle having different proportions when sketched on a T-S diagram could conceivably break even or lose specific power. For this reason, specific power is expected to scale more strongly with CTR than with HPC pressure ratio, as is made evident by the data shown in Figure 6-10.

Figure 6-10 shows specific power over CTR, but the data are grouped according to their HPC pressure ratios so that the influence of each cycle parameter can be examined independently. Regression lines were added only to better illustrate trends made less distinct by the data-scatter. Several of the lines are fit to only three to four data points, and their slopes can be misleading. The data in Figure 6-10 clearly show the closer relationship between CTR and specific power. Additionally, at a constant CTR, specific power climbs somewhat with HPC pressure ratio, but to a lesser, even diminishing extent at higher pressure ratios.

In Figure 6-11,  $P^*$  is also presented over CTR for various HPC pressure ratios. The data in Figure 6-11 indicate a somewhat stronger influence of HPC pressure ratio on  $P^*$  than of CTR on  $P^*$ . This is most likely related to the closer dependence of HPC pressure ratio on  $N^*$ . HPC pressure ratio followed  $N^*$  very closely, where CTR had much less dependence thereupon, as shown by Figure 6-12. Though, incidentally, the HPC inlet temperature (the denominator in CTR) did tend to follow speed, that relationship is not as strongly coupled as that of HPC pressure ratio and  $N^*$ . Furthermore, the HPT inlet temperature had no reason to trend with speed since it is an independently controlled variable, and all of these data sets were maintained at or near the engine maximum HPT inlet temperature.

The cycle thermal efficiency may also be expected to behave similarly relative to CTR and HPC pressure ratio. The efficiency data exhibit more scatter than the power data, and for this reason two separate figures are used to show their dependence on CTR and HPC pressure ratio. Figure 6-13 shows efficiency over CTR and Figure 6-14 plots it over HPC pressure ratio. In both charts the thermal efficiency demonstrates to a small extent the anticipated, upward trend with CTR and HPC pressure ratio. Though these data are more widely dispersed, the stronger correlation with CTR can again be discerned. It is more likely that the ostensible, direct relationship between HPC pressure ratio and thermal efficiency is artifact, since the higher pressure ratios happened to coincide with the higher CTRs. More importantly, the higher pressure ratios also occurred together with higher corrected speeds. Figure 6-15 shows that the HPC isentropic efficiency increased with  $N^*$  as it approached the design speed of 46,000 rpm. The more efficient HPC operation probably contributed the most to any apparent relationship between overall thermal efficiency and HPC pressure ratio. Any similar effects from the HPT efficiency are lost, since it was fixed at 0.85 for the power adjustment calculations. Overall,

there was little variation in thermal efficiency, largely because all of the data points are at full-power.

A principal dimensionless parameter associated with the HPRTE is the recirculation ratio (R) defined by Equation 5.13. This parameter indicates the extent to which the engine is operating within the semi-closed regime. It is generally controlled by changing the LPC pressure ratio, but also depends on the differential pressure between the hot-side recuperator exit and HPC inlet state points. In a physical sense, this is the pressure drop of the recirculation circuit. The Build 4 engine configuration was equipped with a valve in the recirculation flow path with which to vary this differential pressure. This valve, shown as  $V_{REC}$  in Figure 1-1, proved essential in making transitions into the pressurized regime and providing a finer control over recirculation flow rate, and over R.

Figure 6-16 shows the recirculation ratios against LPC pressure ratio. Again, the modeled results are included for comparison. The experimental data in Figure 6-16 are discretized into two distinct bands. This stems from the necessity to throttle the recirculation valve for operational reasons. Specifically, as the turbocharger was brought online by partially closing the exhaust valve ( $V_{EXH}$  in Figure 1-1), the recirculation flow rate would climb much more quickly than the LPT flow rate. Left unchecked, this would result in excessively high recirculation ratios for the combustor being used, and subsequent engine shut-downs. Thus, restriction of the recirculation flow was essential to keeping the engine running stably until the turbocharger came up to speed. Once this was accomplished, the transition from partially closed to fully open was promptly executed. For data sets in which  $V_{REC}$  was about 50% open or less, the recirculation line was considered as “restricted”, while for all other data sets, it was considered “unrestricted”. This discretization of data into only two groups for a valve with continuous operation was

appropriate, as this particular valve was very seldom between half-open and full-open. The two trends exhibit the same shape as each other, but are shifted apart. This is due to the dependence of R upon the pressure drop through the recirculation line, since the restricted values (higher pressure drop) are translated downward from the unrestricted values (lower pressure drop). The experimental trends resemble the modeled trend, though they are shifted downward. This indicates that the model simulated the performance of a HPRTE having an even less restrictive recirculation line. The higher recirculation flows resulted in R values that could barely be achieved in practice with the Build 4 combustor. The model also predicted a turnabout in the trend at higher pressure ratios, though with the Build 4 configuration, these higher pressure ratios could not be achieved. The experimental results do, however, exhibit the same upwardly concave shape as the modeled results, indicating that they would likely change direction if higher pressure ratios were reached.

An important role of semi-closure is to reduce the flow rate of fresh air necessary to operate the cycle. As more of the working fluid is composed of recirculated exhaust gases, the demand for fresh air is decreased as shown in Figure 6-17. For higher values of R the experimental air flow rates appears to remain somewhat constant. These data correspond with the data sets recorded when moving through the transition into the pressurized regime. As mentioned above, when  $V_{EXH}$  was initially closed, the recirculation flow rate rose more quickly than the LPC pressure ratio, and in turn air flow rate. Essentially, the data in Figure 6-17 are very similar to the data in Figure 6-16, but with the ordinate and abscissa exchanged. This is also seen in the modeled air flow rate trend. The modeled trend is double-valued when shown over R, pointing to the relationship between LPC flow rate and LPC pressure ratio. Again, the

experimental trends have a steeper slope at lower R values, and may also mimic the modeled trend if the Build 4 configuration could advance further into the pressurized regime.

In addition to reducing the air flow rate, semi-closure also serves to reduce the exhaust flow rate of the system as well. Beyond decreasing the size of the turbocharger, a lower exhaust flow rate will also decrease the heat signature of the HPRTE, which can be paramount in some applications. Since the air flow rate and exhaust flow rate differ very little, the data in Figure 6-17 can also be used to approximate the exhaust flow rate over R.

Semi-closure also changes the HPRTE combustion environment. Since the combustor inlet gases are being diluted with exhaust gases, the stoichiometry within the reaction zone changes with R at a given total flow rate. Figure 6-18 shows how the equivalence ratio increases with R alone. The experimental trends appear to agree well with results predicted by the model. Though the modeled recirculation ratios were much higher, the slopes of all three trends are very similar. The experimental data in Figure 6-18 separate into the two bands, but show some intermingling of the restricted and unrestricted cases at higher R values. This points to the dependence of equivalence ratio on other operating parameters as well. Clearly, in Equation 5.29, the equivalence ratio depends on the air and fuel flow rates. However, with all of these data sets at full power, this is expected to be influenced more by the air flow rate, which appears in the denominator and was more varied in its values. The equivalence ratio can therefore be related to another, primary operational parameter, the LPC pressure ratio, as demonstrated in Figure 6-19. The experimental data in Figure 6-19 tend to deviate less from their respective bands. The experimental and modeled trends bear a close likeness to the trends in Figure 6-16, which reflects the similar, inverse relationship with air-flow-rate that R and equivalence ratio share.

The more pertinent way in which R affects the combustion environment can be measured in the composition of the exhaust gas. The impact of R on emissions is here quantified by the concentrations of NO and CO, the least desirable constituents existing in significant amounts. The concentrations of these two gases in the exhaust mixture are shown in Figure 6-20. As expected, and is typically the case, a reduction of the NO concentration is compromised by a corresponding increase in CO. This results from the opposite dependences of their equilibrium concentrations on temperature and O<sub>2</sub> concentrations. The formation rate of NO scales linearly with the product of O<sub>2</sub> and N<sub>2</sub> concentrations, and with temperature cubed. As R is increased, the N<sub>2</sub> concentration remains relatively unchanged while the O<sub>2</sub> concentration drops off, as affirmed by the data in Figure 6-21. The N<sub>2</sub> data in Figure 6-21 indicate a slight rise with R, but regression lines were added to help illuminate the difference in slopes. It is clear that the decrease of O<sub>2</sub> concentration over R is faster than the rise in N<sub>2</sub> concentration. While this dilution of gases detracts from the conditions for NO formation, it also diminishes the rate at which CO can further oxidize to form CO<sub>2</sub>. Consequently, the CO concentrations can be seen to rise with R. Another influential factor is the temperature at which these reactions are taking place. The effects of lessening the O<sub>2</sub> concentration are two-fold in that the flame temperature in the primary zone of the combustor is also reduced. This reduction in temperature further serves to suppress NO formation, but again, this effect will also reduce the reaction rate to finish oxidizing CO.

An unexpected phenomenon is evident in Figure 6-20. At the high end of the R range, the NO concentration takes a marked upward swing. This turnabout cannot be rationalized with any of the above arguments, since, at still higher R values, all of the NO-diminishing effects are increasingly present. The most likely reason is related to a minor deficiency in the HPRTE

hardware. The original rover combustor was modified to accommodate recirculation flow by welding straps over some of the dilution holes. This forces more of the oxygen-dilute gases through the combustor primary zone for combustion with the intention of restoring oxygen to the reaction. While this first modification worked well for moderate R values ( $R < 1.3$ ), it proved to be insufficient in redirecting  $O_2$  at higher R values. As R was increased, the stoichiometry in the primary zone would progressively become leaner. Instabilities of the flame would then follow, viewed as violent flickering in the combustor view port, until the flame relocated downstream to the dilution holes, where more oxygen was present. After the flame relocated, the geometry of the combustion environment changed, with a greatly increased time for NO forming reactions to take place.

A particular benefit of cooling the recirculated exhaust gases is the opportunity to extract the resulting water condensate. However, before this can be achieved to an appreciable extent, the exhaust recirculation mixture must first be cooled to its dew-point. This was accomplished with the VARS heat exchangers and the WGC, and relied on the performance of each. Unfortunately, the VARS employed for these experiments was somewhat undersized to provide the refrigeration necessary for respectable water extraction.

Another non-dimensional parameter is introduced to present the water extraction data: the mass flow rate of extracted water, normalized by the fuel mass flow rate. This Water to Fuel Ratio (WFR) is plotted against the LPC pressure ratio in Figure 6-22. The theoretical maximum for WFR on a volume basis is around one, which, on a mass basis, equates to approximately 1.2, though these values can only be approached at high recirculation ratios. Taking this into consideration, it can be said that the water extraction performance was respectable at lower LPC pressure ratios. However, the WFR subsequently drops as the tests moved further into the

pressurized regime. The modeled results predicted a much higher WFR throughout the pressurized regime. However, the model also simulated an ideal VARS equipped with sufficient refrigeration capacity to maintain a constant, 59 °F (519K) CGC exit temperature. Thus the modeled WFR depended only on the gas properties at the CGC inlet, and not on VARS performance.

There are two competing effects relating to HPRTE operation that most directly contribute to WFR: R and LPC pressure ratio. Greater concentrations of water in the CGC inlet gas mixture will lead to a greater potential for water extraction by raising the dew-point temperature. The recirculating gas by itself has a high water concentration, but is dried considerably when mixed with the fresh air from the LPC. Thus, the greater values of R can be expected to yield higher WFR values, and R drops with increasing pressure ratio, following the trend seen in Figure 6-22. However, the effect of increasing the pressure in the recirculation line (increasing the LPC pressure ratio) should raise the saturation pressure of the water vapor along with its dew-point, initiating water extraction earlier in the cooling process. Regardless of these two factors contending with one another, the fact remains that the VARS and heat exchangers must perform well for appreciable water extraction to be realized. The overriding factor that governed water extraction performance was undoubtedly the suffering performance of the VARS and WGC at higher LPC pressure ratios. The heat load on the three recirculation line heat exchangers is related to the LPC pressure ratio by the recirculation flow rate, which was driven upward with LPC pressure ratio by throttling  $V_{EXH}$ , as shown by the data in Figure 6-23.

The recirculation gas mixture did reach its dew-point in the CGC most of the time, but by this point the refrigeration capacity was usually exhausted. Although there were no means available to directly measure the humidity within, the saturated state of the gas was made evident

by noteworthy quantities of liquid water finding its way through leak-paths in the ducting of the HPC. Figure 6-24 illustrates how the dew-point temperature changed with the LPC pressure ratio. Figure 6-24 also shows the increases in CGC inlet and exit temperatures associated with further pressurization of this HPRTE rig. It is apparent that, though the dew-point temperature did increase with LPC pressure ratio, the evaporator temperatures increased at a greater rate. The water extraction rate should roughly scale with the difference between the inlet dew-point temperature and CGC exit temperature. Although the CGC temperature difference increased at higher pressure ratios, the CGC exit temperature still climbed quickly enough to approach the dew-point temperature, lessening the water extraction rate.

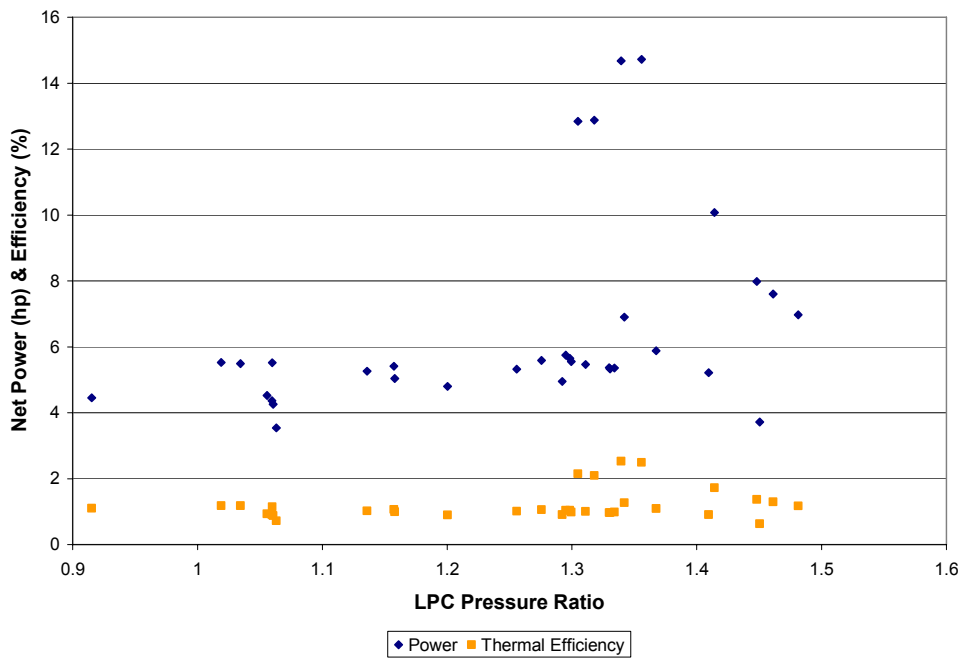


Figure 6-1. Actual net power output from Build 4 engine runs.

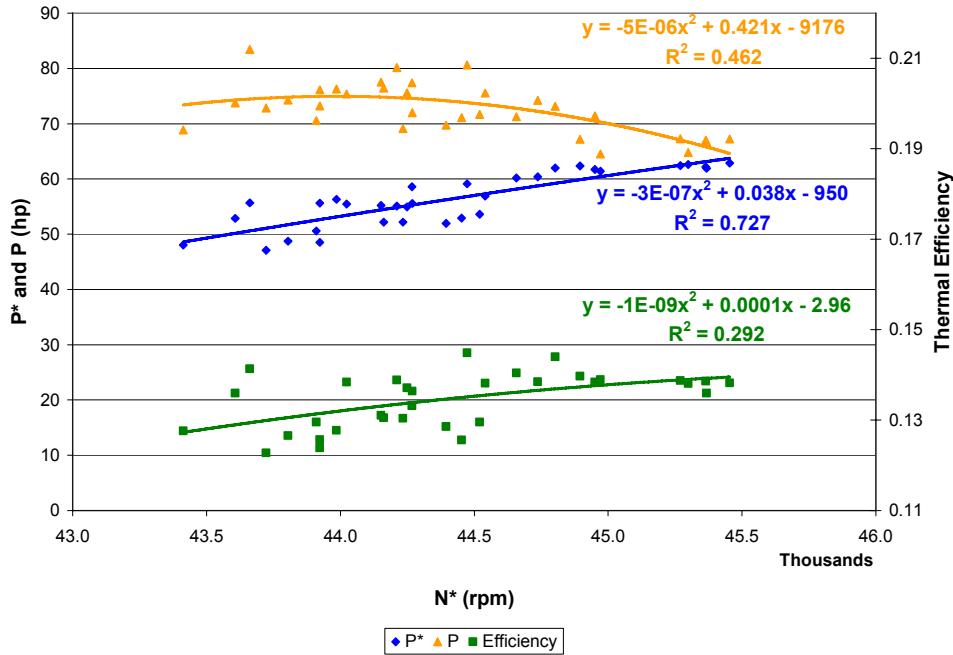


Figure 6-2. Corrected Power, power, and thermal efficiency over corrected speed.

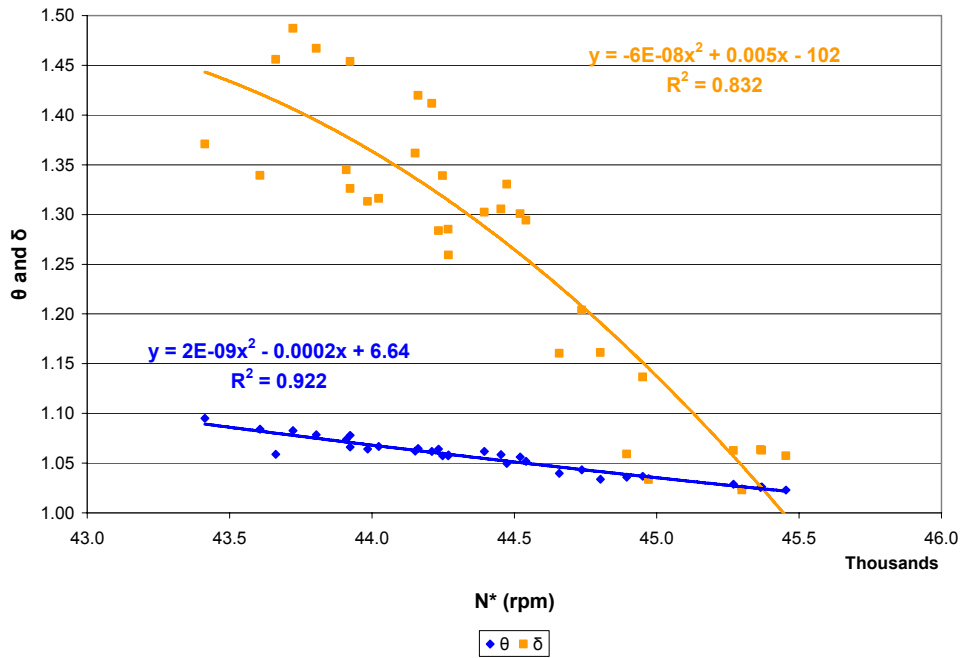


Figure 6-3. Scaling parameters versus corrected speed.

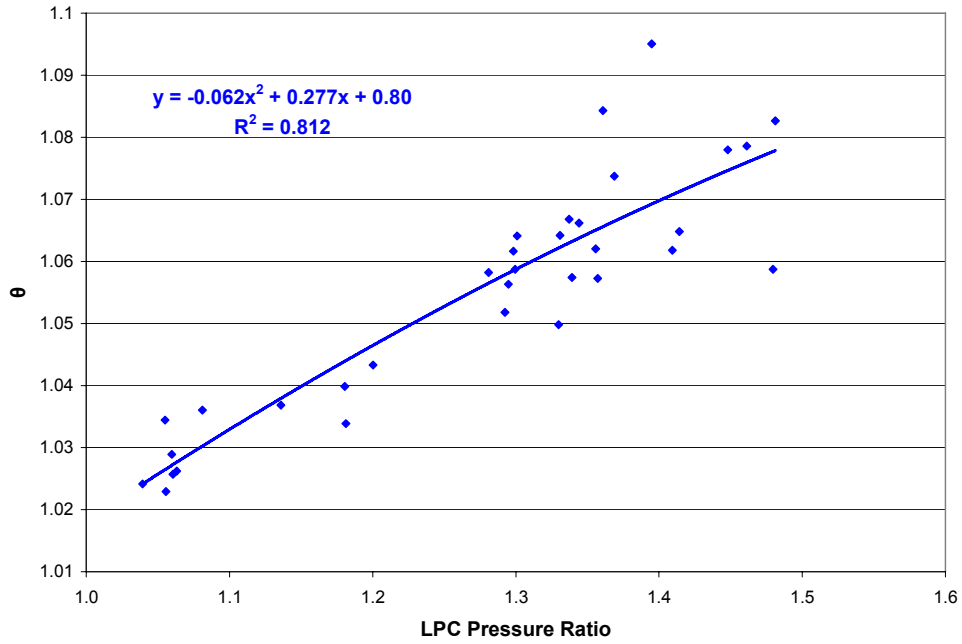


Figure 6-4. Theta versus LPC pressure ratio.

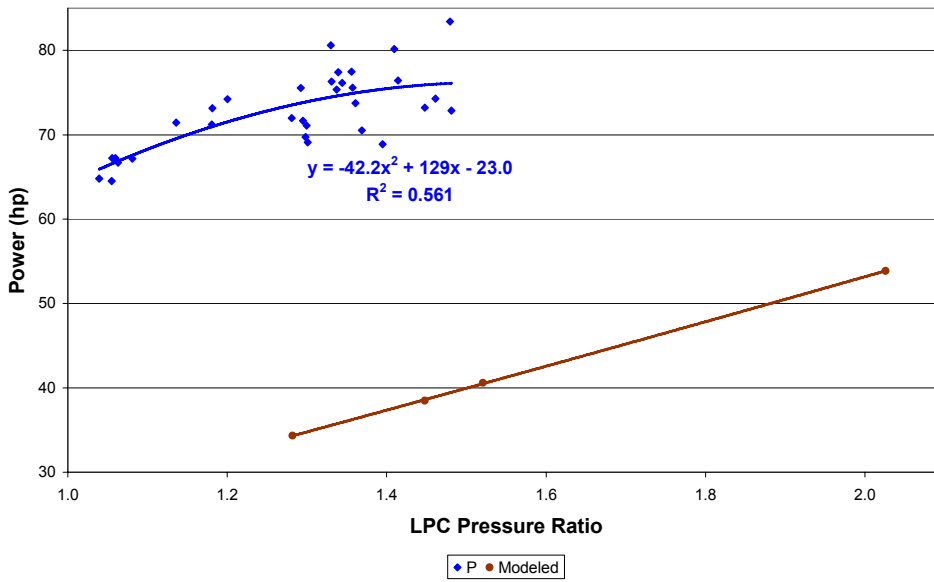


Figure 6-5. Power versus LPC pressure ratio.

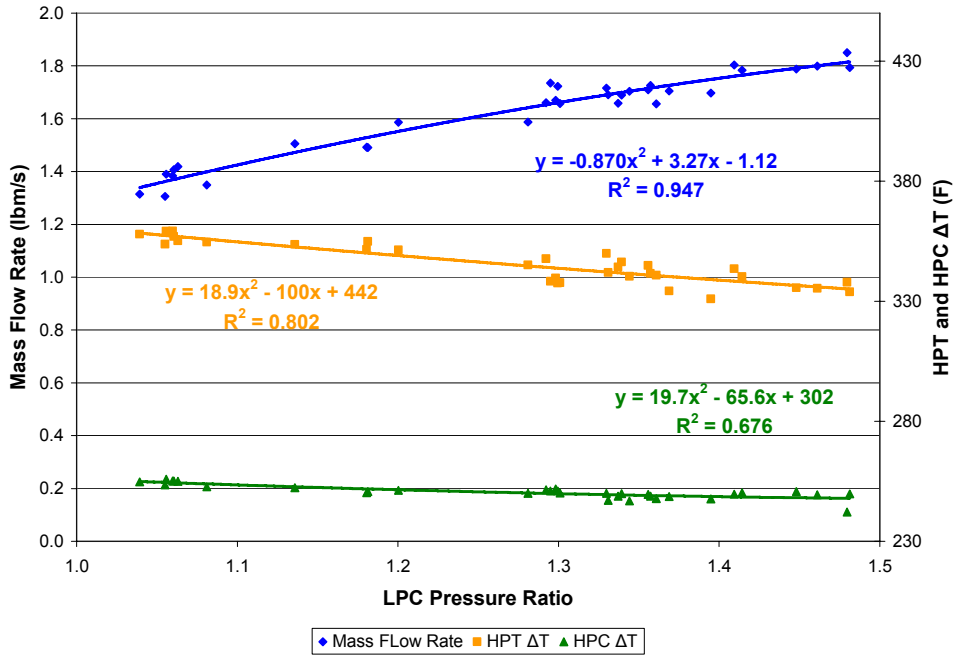


Figure 6-6. High pressure turbomachinery temperature differences and mass flow rate versus LPC pressure ratio.

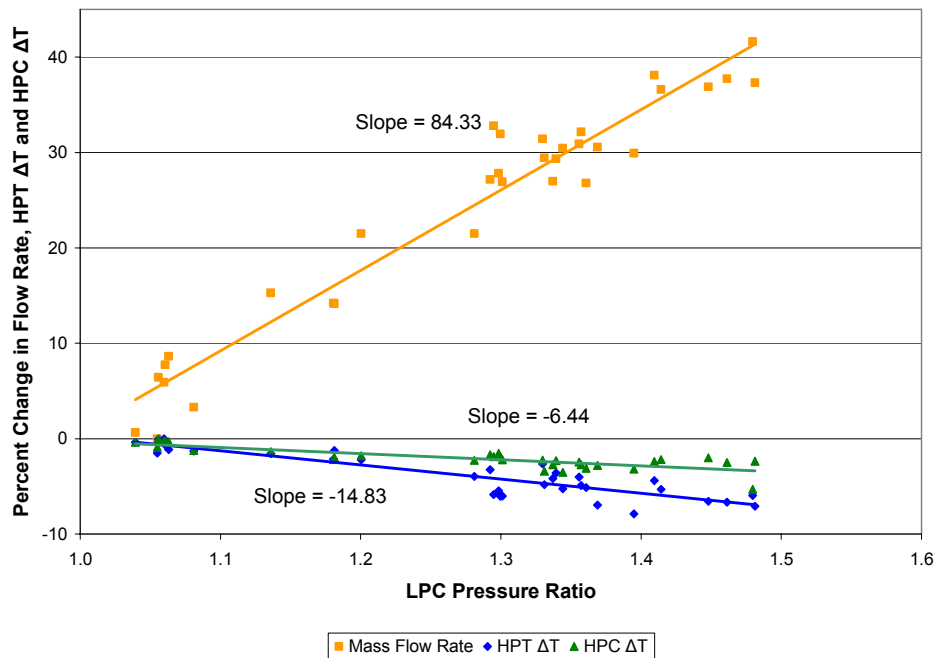


Figure 6-7. Percent change in high pressure turbomachinery temperature differences and mass flow rate versus LPC pressure ratio.

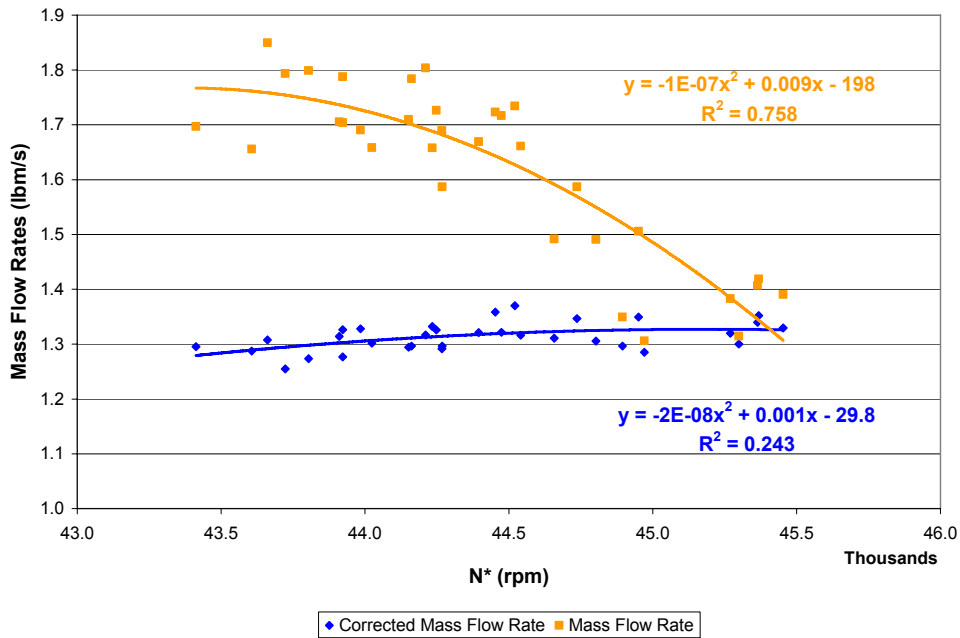


Figure 6-8. Flow parameters versus corrected speed.

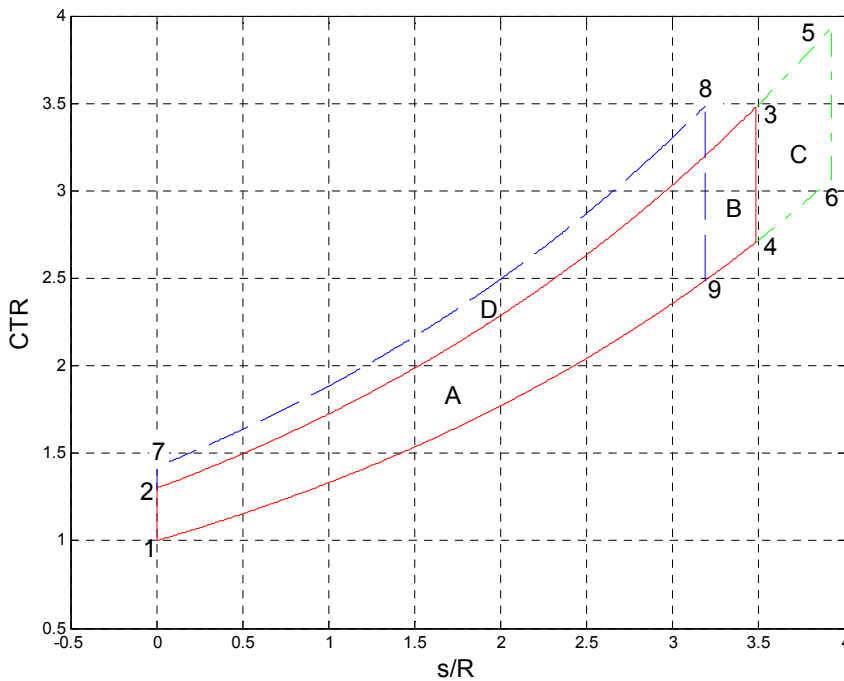


Figure 6-9. Generalized effects of HPC pressure ratio and CTR on specific power, illustrated on a T-S diagram.

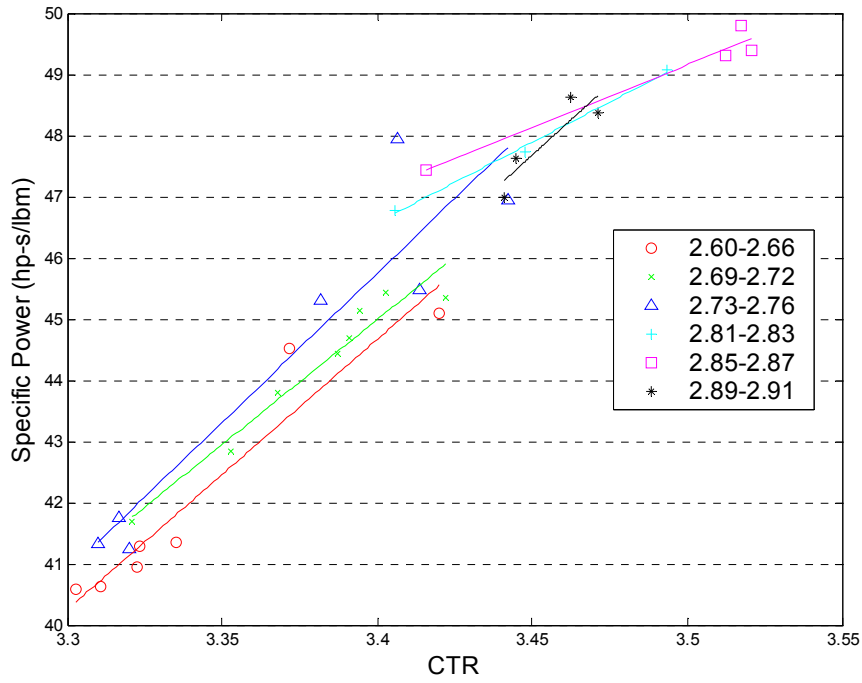


Figure 6-10. Specific power versus CTR, for various HPC pressure ratios.

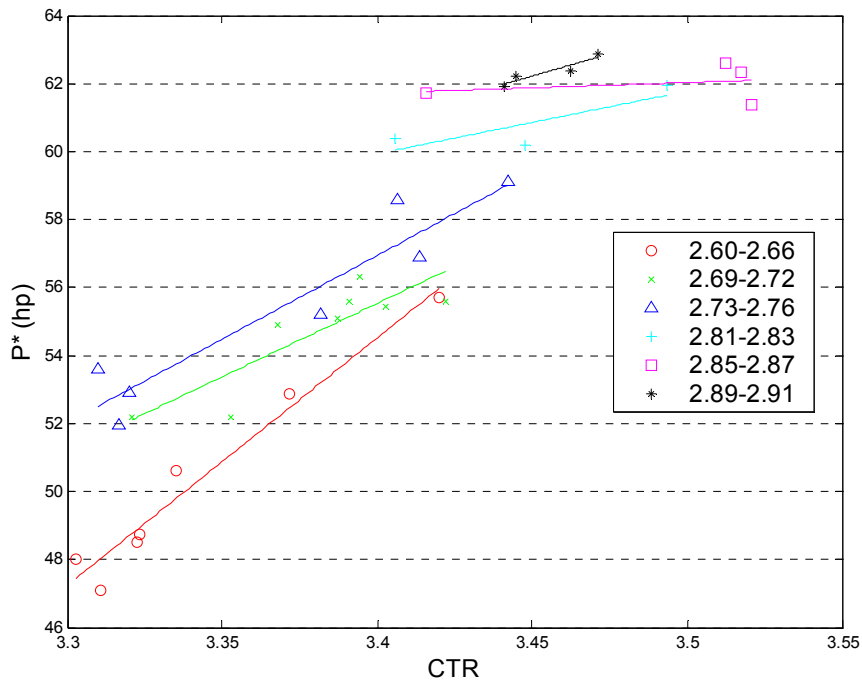


Figure 6-11. Corrected power versus CTR for various HPC pressure ratios.

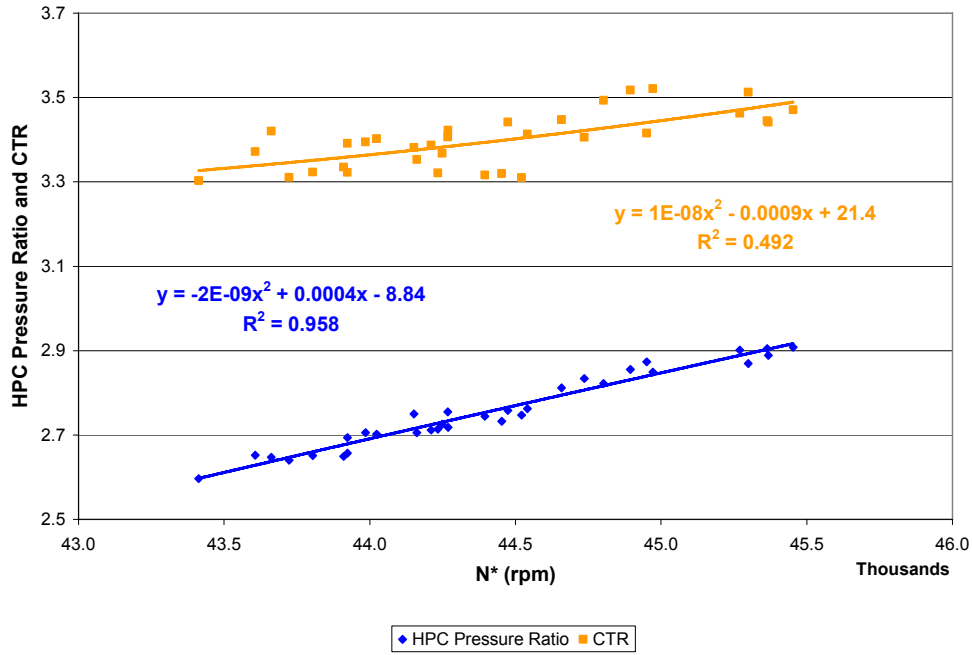


Figure 6-12. HPC pressure ratio and CTR versus corrected speed.

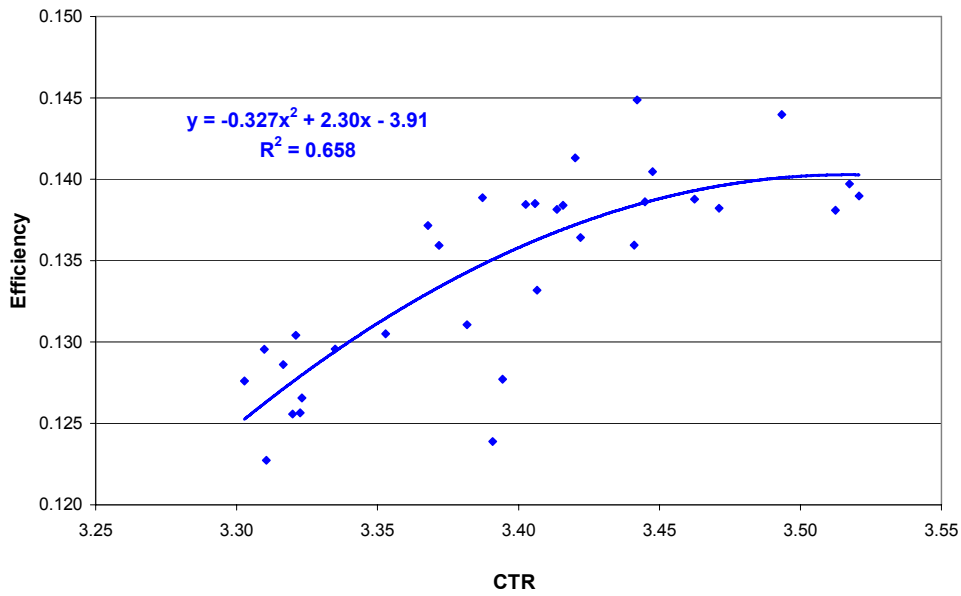


Figure 6-13. Thermal efficiency versus CTR.

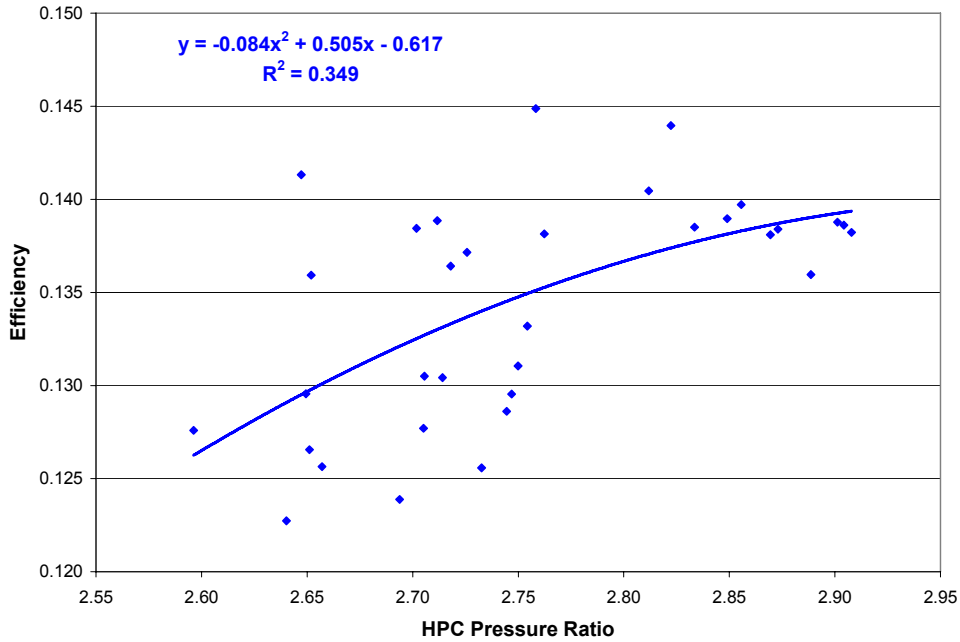


Figure 6-14. Thermal efficiency versus HPC pressure ratio.

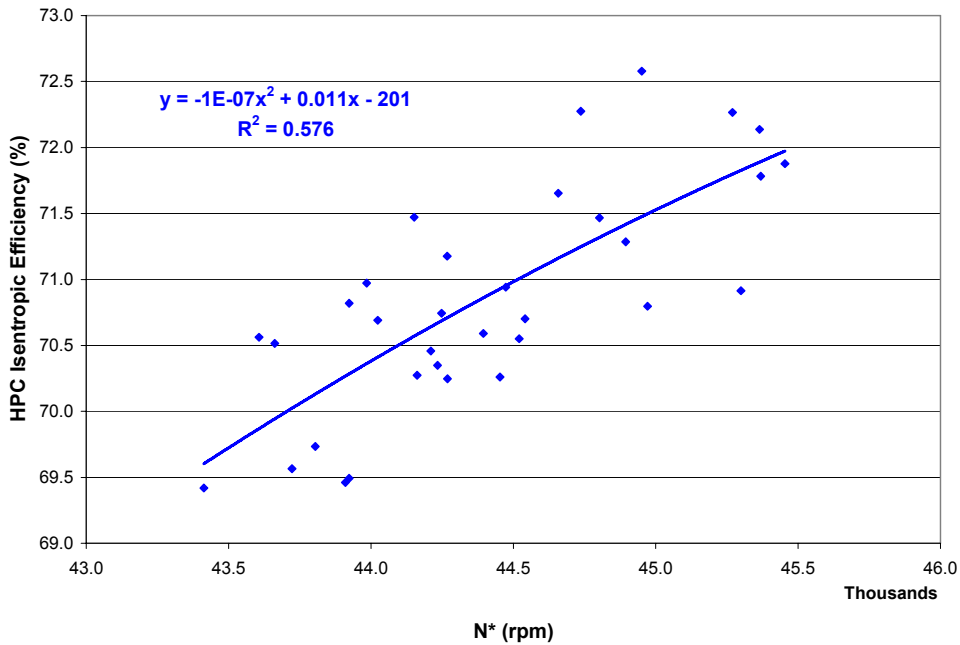


Figure 6-15. HPC isentropic efficiency versus corrected speed.

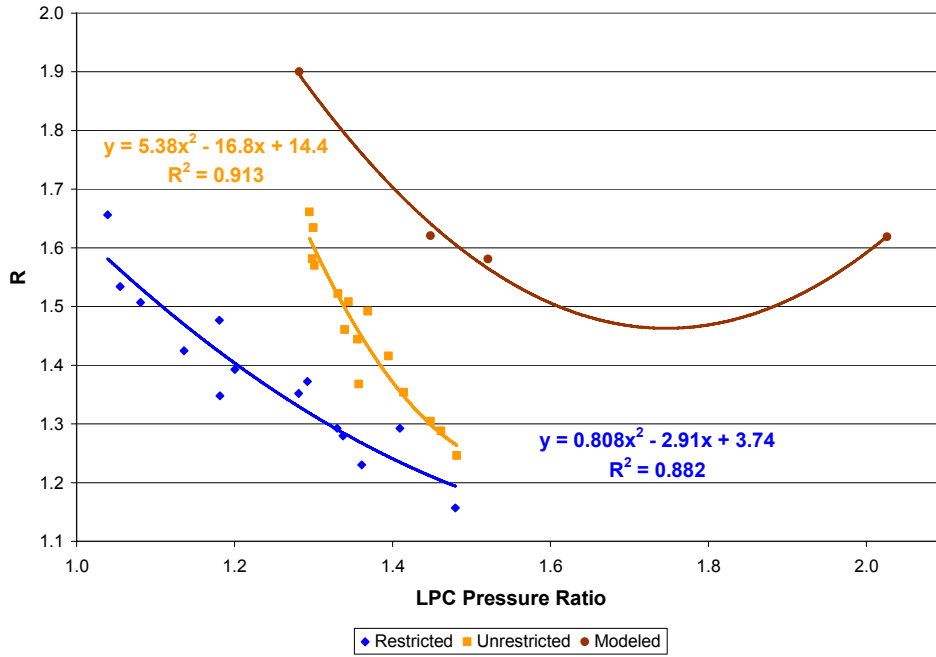


Figure 6-16. Recirculation ratio versus LPC pressure ratio.

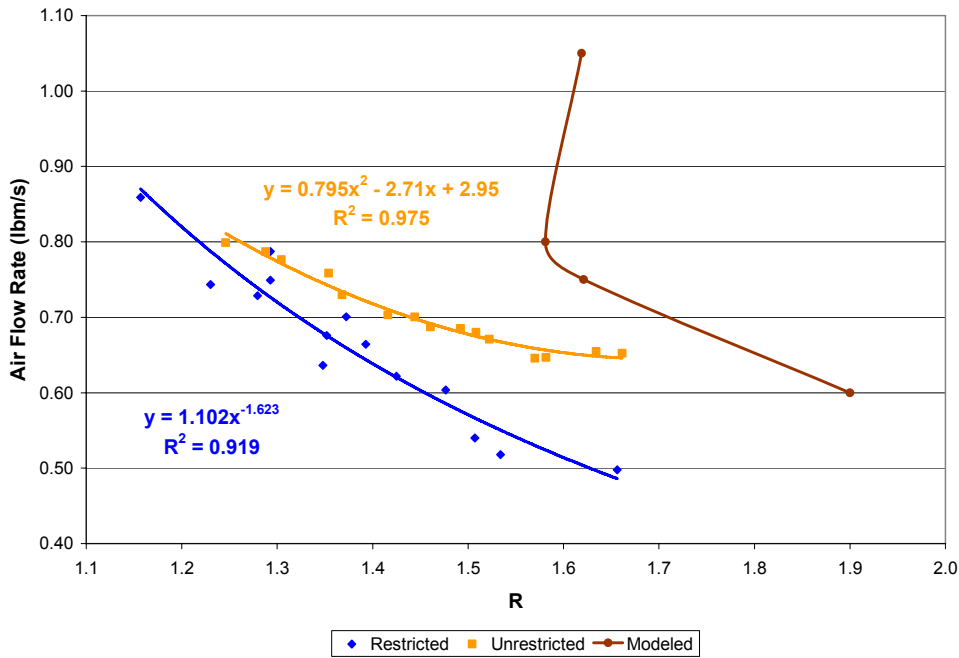


Figure 6-17. Fresh air flow rate versus recirculation ratio.

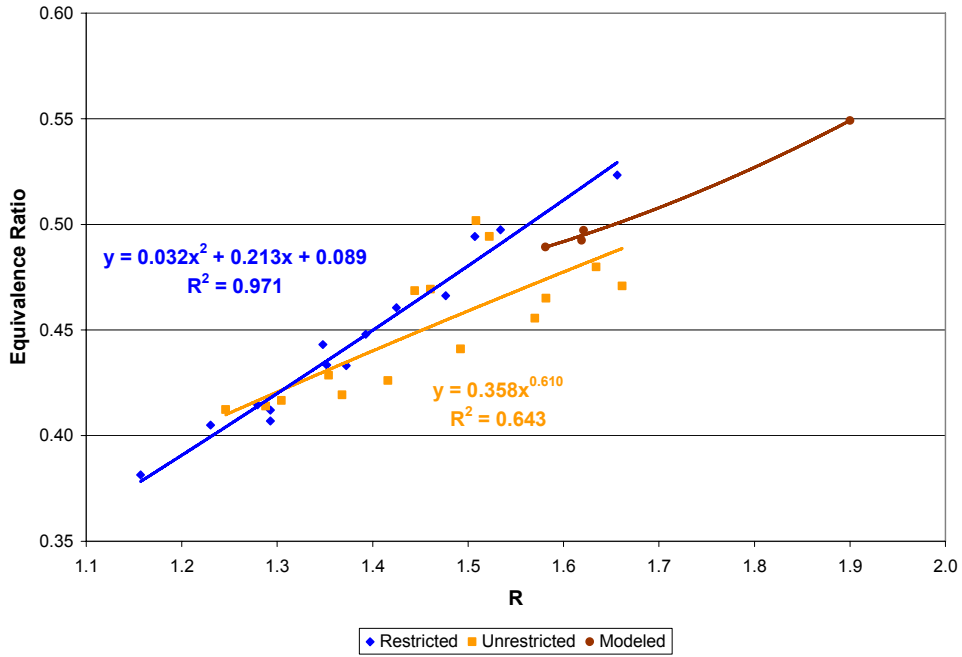


Figure 6-18. Equivalence ratio versus recirculation ratio.

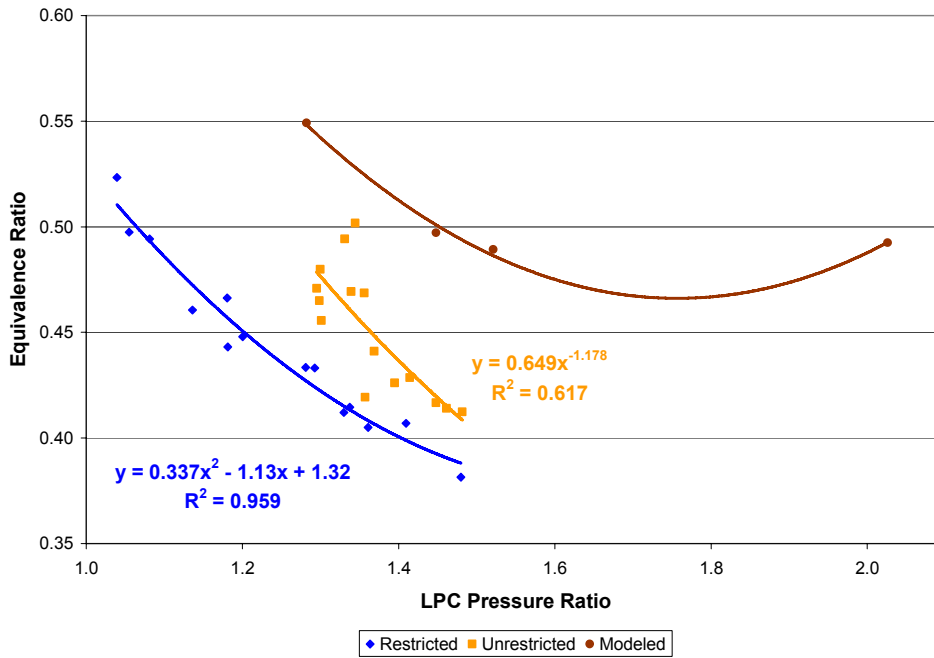


Figure 6-19. Equivalence ratio versus LPC pressure ratio.

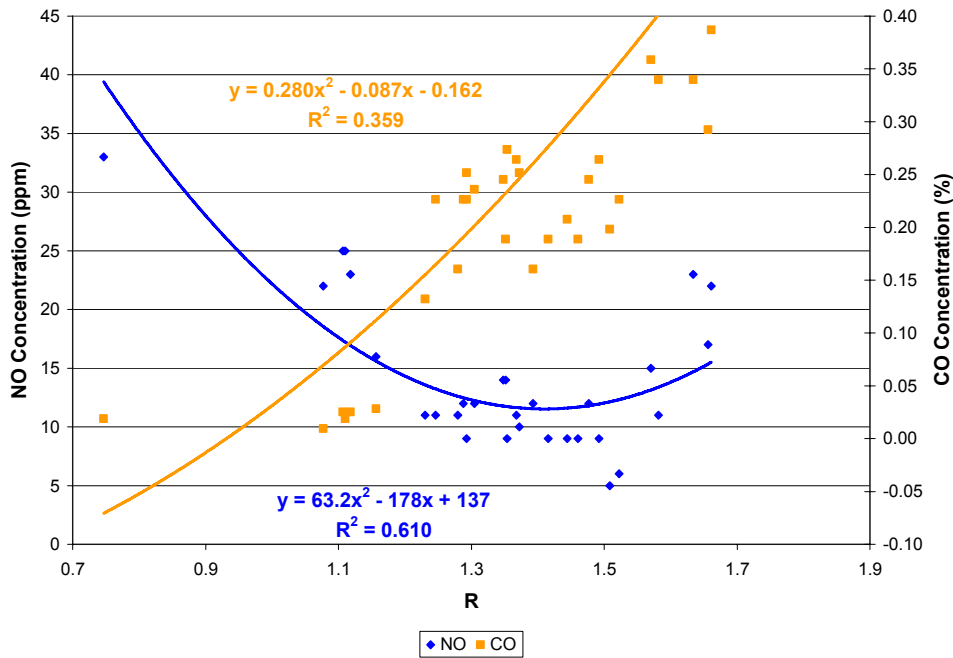


Figure 6-20. Nitric oxide and carbon monoxide concentrations versus recirculation ratio.

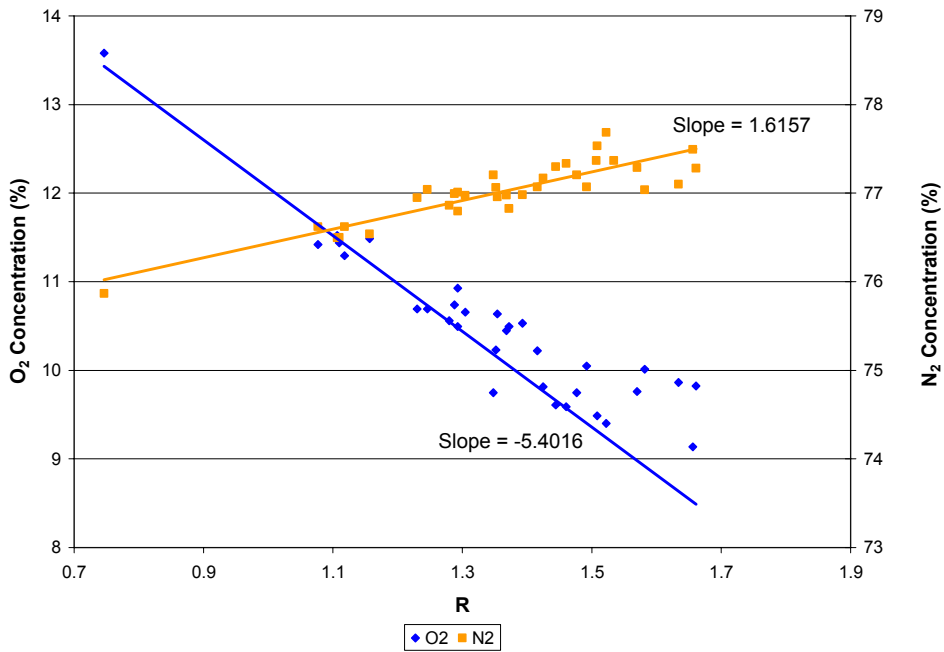


Figure 6-21. Oxygen and nitrogen concentrations versus recirculation ratio.

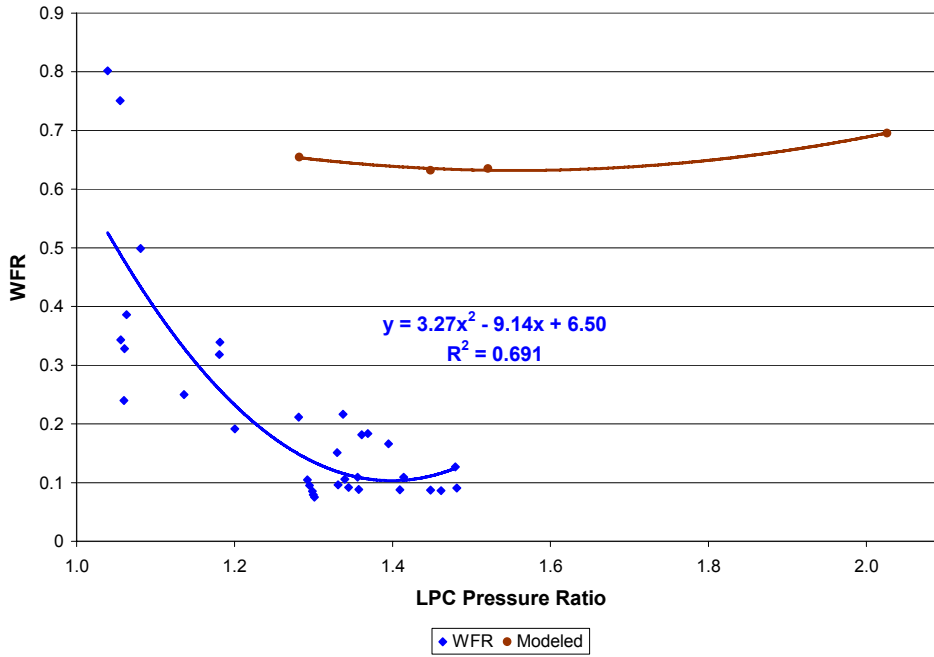


Figure 6-22. Water-to-fuel ratio versus LPC pressure ratio.

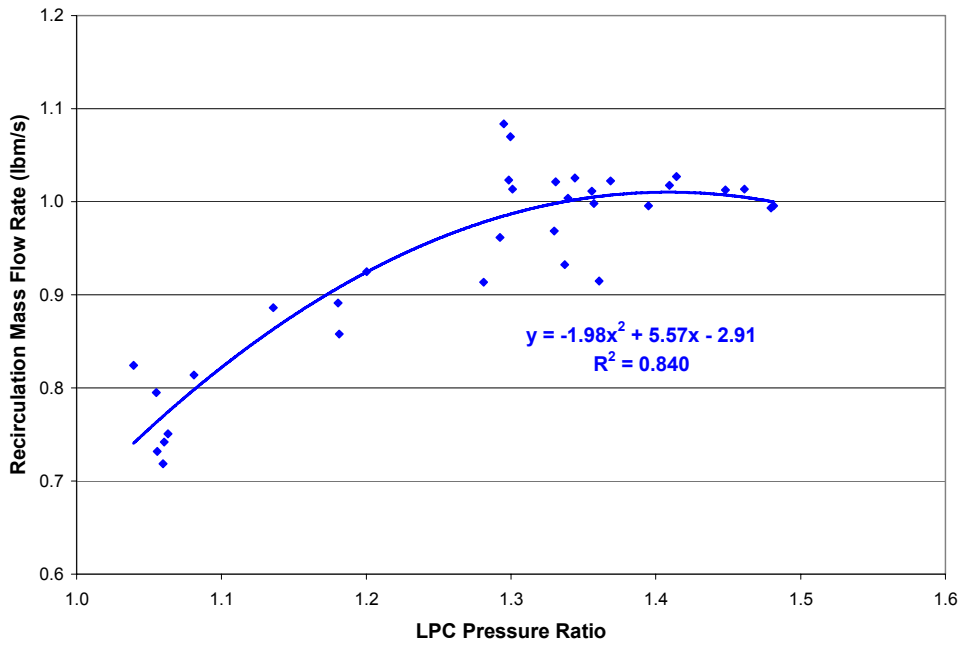


Figure 6-23. Recirculation flow rate versus LPC pressure ratio.

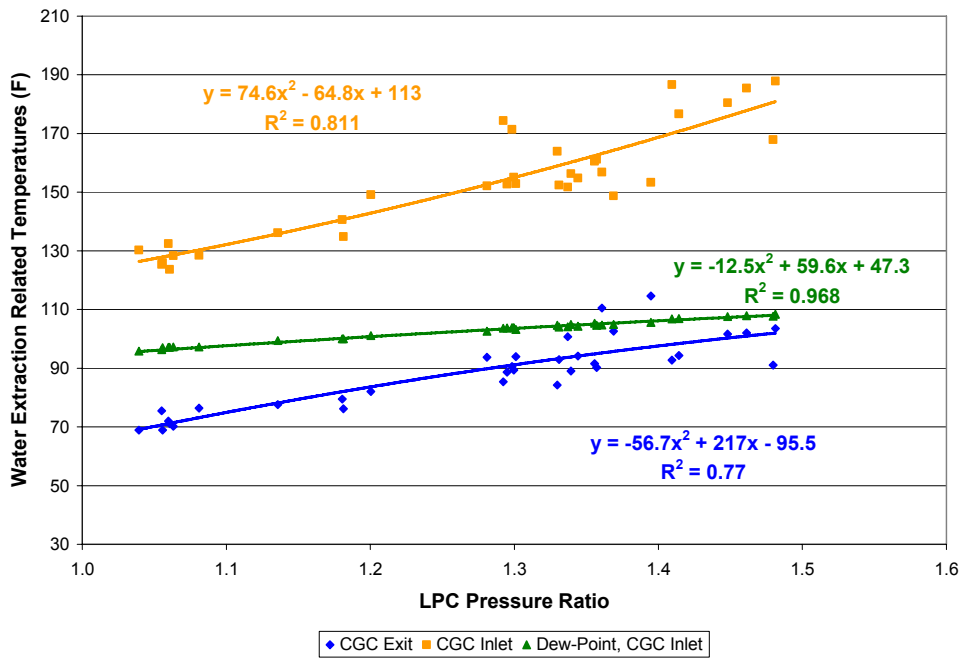


Figure 6-24. Temperatures related to water extraction versus LPC pressure ratio.

## CHAPTER 7 CONCLUSIONS AND RECOMMENDATIONS

### Summary

Following these experimental efforts, several conclusions can be drawn about the overall success of the study, and about the theoretical capabilities offered by the HPRTE/VARS combined cycle. Throughout this research, four engine configurations were tested and progressively altered in order to arrive at an experimental apparatus best suited for operating the HPRTE/VARS, and for demonstrating its qualities. It was shown that the VARS hardware can be successfully integrated with pressurized and semi-closed engine ducting, and driven by the hot recirculating gases, resulting in a synergistic combination of cycles. The successful operation of the HPRTE was also demonstrated, as the HPRTE was pressurized and semi-closed to various degrees. Despite operational limitations presented by certain components, data were acquired and adjusted to successfully prove the following theoretically proposed concepts:

- The HPRTE power output can be increased/decrease by diverting exhaust flow through/around the LPT, varying the pressure ratio across the turbocharger, and the total mass flow rate through the engine.
- The HPRTE efficiency can remain approximately constant for a variety of power levels, since the dimensionless operating point of the engine changes very little, or not at all during power transitions.
- The emission of  $\text{NO}_x$  from the HPRTE is reduced as R is increased.
- The mass flow rates of air into and exhaust gas out of the HPRTE are reduced as R is increased.
- Significant quantities of water can be condensed and extracted from the recirculating gases.

The performance of the HPRTE/VARS can be hindered by certain of its components. The pressure drop in the recirculation line was the primary detraction from the power-making potential of the engine. On this engine rig, the pressure difference between the HPT exit and

HPC inlet significantly reduced the HPT pressure ratio, raising the HPT exit temperature near to its limit. When this occurred, there was little or no margin remaining in HPT temperatures to apply a load using the dynamometer. Gas leaks in the ducting and engine casing were also suspected to have an adverse effect on net power, though the extent to which they detracted from the total flow rate remains uncertain.

While an ideal engine would operate at a constant speed throughout the pressurized regime, this engine, equipped with a mechanical governor, was subject to a reduction in speed as the engine was pressurized. The speed-droop was small, but discernable. A small decrease in corrected flow rate was observed at the engine speed lessened, as well as a drop in both the HPC and HPT pressure ratios. With the drop in pressure ratios followed a drop in both temperature ratios, and in turn the temperature differences (proportional to net power) across the HPC and HPT. Despite the departure from its design speed, the HPRTE/VARS suffered only a small decrease in thermal efficiency, barely evident in the data scatter.

The VARS described in Chapter 3 was designed specifically for this application, but was intended for a slightly different ducting configuration, feeding cooler gases to the HGC. In actuality, the HGC inlet gases were approximately 300-400 °F (167-222 K) hotter than designed for, increasing the HGC effectiveness. This effectively shifted the optimal VARS operating point to much lower HGC and CGC flow rates, and caused the VARS to be overwhelmed at higher heat loads. This effect prohibited significant water extraction rates from being realized at higher LPC pressure ratios, because the CGC temperatures rose much faster than the dew-point temperature. Substantial water extraction was however accomplished at lower LPC pressure ratios where R was highest and the VARS performed respectably.

## **Recommendations**

Through the course of these HPRTE/VARS experiments, much was learned about the positive attributes of the combined cycle, and about its limitations. The range of operations and performance of this combined cycle were found to be limited by several details associated with its hardware. Difficulties and uncertainties were also encountered while completing the data reduction and interpretation due to inadequacies in the instrumentation. These experiences have served to generate several recommendations that would improve the quality of future HPRTE/VARS experimental endeavors.

Significant improvements can result from utilizing a VARS having a wider range of operations. This is believed as key since the HPRTE itself is capable of operating with a variety of flow rates, temperatures, and pressures in the recirculation flow path. An ideal VARS would possess more capacity and a more sophisticated control scheme to maintain a constant HPC inlet temperature, and perhaps excess refrigeration capacity. This would most strongly impact the water extraction rate from the HPRTE. While the HPC inlet (CGC exit) temperature remains constant, the dew-point temperature would increase with LPC pressure ratio, increasing the water extraction rate. The production of excess refrigeration from the VARS would also be a favorable quality, and would allow for a new dimension of operations to be investigated. Specifically, this would permit experiments where excess refrigeration can be traded for engine efficiency and water extraction, or vice versa.

The potential of an HPRTE to make power could be greatly increased if the pressure drops in the recirculation line are kept minimal. The VARS heat exchangers used in these experiments were relatively compact, and it would be tolerable in research-oriented applications if they were somewhat larger. This would serve to reduce the back-pressure on the HPT and restore some margin in the HPT exit temperature for engine loading. Another point worth noting is that

engines with higher pressure ratios should suffer less from a given differential pressure across the recirculation line. These experiments saw engine recirculation differential pressures of up to 4 psi (28 kPa), which resulted in a 20% reduction in the HPT pressure ratio. The same differential pressure with a higher HPT pressure ratio should be a less significant detraction from the HPT temperature difference.

The range of HPRTE operation could also be markedly enhanced by employing a variable geometry turbocharger (VGT). VGTs have the ability to vary the AR ratio on their turbine housings, allowing for a variety of LPT flow rates for a given LPT pressure ratio. This would all but eliminate the challenge of selecting one turbocharger with a constant AR ratio to match the variety of recirculation ratios and LPC pressure ratios seen by the HPRTE. A VGT would also most likely eliminate the need for a recirculation valve. The recirculation valve has functioned primarily to restrict recirculation flow after the wastegate ( $V_{EXH}$ ) is initially closed, diverting more flow through the LPT. When operating in this way, the recirculation pressure drop is higher than necessary. A VGT would function with a larger AR ratio during initial pressurization, and may further do away with the need for a wastegate. It may be preferable, however, to retain the service of a wastegate as it would allow multiple R-versus-pressure-ratio lines on which to operate.

Future HPRTE configurations may also benefit from additional water extraction points directly upstream of the HPC inlet. Condensate was observed on several occasions leaking from flanges in this location, confirming the presence of liquids in the ducting near the HPC inlet. The gas entering the HPC can be saturated with water vapor (ideally it always is) and has even been observed as “misty” with tiny, suspended water droplets. While the small droplets entering the HPC can be a performance enhancement, they can also present a problem if they coalesce on

the ducting walls, or become too large for the HPC rotor being used. This can result unnecessary erosion of the compressor wheel.

The last recommendation following this work relates to instrumentation, and would be found most useful in applications where the water extraction potential is exploited—the inclusion of a duct-mounted humidity sensor. This instrument would significantly increase the ease of data reduction, eliminating many of the approximations and assumptions discussed in Chapter 5. A more reliable knowledge of this quantity would result in a much more accurate dew-point temperature, heat exchanger effectiveness, and overall quantification of water extraction performance.

APPENDIX A  
OPERATING PROCEDURES FOR HPRTE/VARS

Starting Procedure:

Prior to Start:

1. Turn on the VCR Recorder, turn VHS Camera to CAMERA .
2. Do a communications check.
3. Plug in ARU. Place the ARU in standby by rotating spring return switch clockwise. The YELLOW light should come on.
4. Turn on the condensate removal pumps.

Engine Start:

1. Turn on the DC circuit breakers local to the skid. Red indicator light should come on locally and in the Control Room
2. Move the Speed trim Valve to half way between open and shut.
3. Check open the High Pressure Fuel Manual Isolation Valve. Valve handle cross-line with the fuel pressure line.
4. Move S1 to ON.
5. Check Oil Pump #1 to Bypass.
6. Check Fuel Pump to Bypass (S9).
7. Check Oil Pump #2 to Normal.
8. Turn Oil Pump #2 to On. Confirm pressure light on before continuing.
9. Check fuel pump Off.
10. Check Air Pressure light on.
11. Move Ignition switch to ON. This enables the ignition system and the starter
12. Check the 12VDC starter Off.
13. Check Spray Cooler switch Off.

14. Check the Combustor Air Valve Off.
15. Check the solenoid Fuel Valve Off.
16. Press the RUN button. The lighted button and the control room indicator light should come on.
17. Press and Hold the START button. Check Fuel Pressure light on. The fuel valve solenoid energized light should be Off.
18. At 300 PRM (or 40 PSIG fuel pressure), turn the Solenoid Fuel Valve on. Verify ignition and increase in engine speed.
19. Release the start button when green light (starter solenoid energized) goes out.
20. Engine speed should increase to self-sustaining, about 2700 dyno RPM. Wait until fuel has burned off in the sight glass, if necessary. Slowly move the Speed Trim valve to full OPEN, rotated down. Engine speed should increase to approximately 3000 RPM as read on the Dyno.
21. Turn the DC exciter and Local switch to Off. Verify local oil pressure.

Recirculation, ARU, Dyno, and Turbocharged Operation:

1. Open ARU V14. ARU V13 can be opened 1 ½ turns to hasten warm up.
2. Slowly open the Recirculation Isolation Valve to until recirc DP=1.6.
3. Partially close the Main Air Inlet Valve. MAI DP=0.5 in.-H<sub>2</sub>O oil max. Recirc DP=6.5". Recirc ratio=0.6.
4. Close the Dyno outlet valve until the flow is about 5 GPM and pressure is 28 to 30 PSIG.
5. ARU System pressure will rapidly build up. When the ammonia receiver pressure reaches 210 psig, open the condenser cooling water valve to maintain pressure around 235 psig, but below 250 psig. Run data shows about 4 gpm is appropriate at full dyno load (no boost). Discharge weak solution if required.
6. Adjust solution flow to 3.2 gpm by throttling V13 if required.
7. Slowly adjust the Boost control pressure to 8.0 PSIG. Verify Boost Control Valve stem position is 28% open. To avoid burner instability use the Recirculation Control Valve to keep R less than 1.0. Flame transition should occur near this setting.

### Recirculation Setting and Steady-State Operations:

1. Adjust HRVG Heat Load to 23TR using Recirc and Boost control valves. During this time ARU should be adjusted to limit T-HPCI below 90F. Record data as necessary. Purge non-condensables and remove solution as necessary.

PR LPT may be 1.0.

2. Increase HRVG heat load within stable limits. Record data Column 3 and 4. Recirculation control and Boost control maybe used to achieve PR LPT up to 1.8.

### Shut Down:

1. Remove Dyno load slowly from engine.
2. Open Boost Control valve to 7.5 PSIG. Restrict Recirc control to DP=16" (about 45 degrees). Open MAI.
3. Reduce engine speed to 2900 RPM using the Speed Trim Valve.
4. Close the Manual Fuel Shut Off Valve.
5. Press the STOP button.
6. Move the Fuel Valve switch to Off.
7. Turn Off VCR.

### Post Shut Down:

1. Limit soak-back to under 380<sup>0</sup>F. Motor the engine for 30 seconds as necessary.
2. Turn ARU off. Close ARU valves V14 and V2.
3. Collect Data sheets.
4. Review Tape immediately. Synchronize data sheets and data stream with unusual events.
5. Critique and review the test run. Check for signs of fluid leaks. Reconfigure the engine for a quick restart.

APPENDIX B  
SETUP PROCEDURES FOR HPRTE/VARS

Support Systems:

Site Chill Water:

1. Slowly open the source and return overhead isolation valves.

Cooler Chill Water:

1. Connect the process water hoses to the cooler.
2. Supply water to the coolers by opening all isolation valves.
3. Verify main cooler flow by listening for flow noise. Record initial flows:
4. Record minor leaks for later resolution.

ARU Chill Water:

1. Connect the process water hoses to the ARU.
2. Supply water to the cooler by opening all isolation valves.
3. Verify main cooler flow by listening for flow noise.
4. Record minor leaks for later resolution

Boost Control Valve and Waste Gate Control Air:

1. Set supply air regulator by the South door to 40 psig.
2. Ensure the Supply, Boost Control and Waste Gate Bleed toggles are closed.
3. Ensure the Waste Gate Isolation toggles are open.
4. Verify the Supply Air Pressure at the control panel is between 25 and 30 psig by adjusting the South door regulator in 1. above.
5. Open the Fisher Control Regulator until the Boost Control Air gage reads 15 psig. This opens the 6" Boost Control valve completely.
6. Visually verify the position of the Boost Control Valve is full open by observation of the valve stem indicator.

7. Verify the turbocharger Waste Gate Regulator is set to 20 psig.
8. Verify operation of the Turbocharger Waste Gate with an assistant listening for actuation, from full open to full closed, by closing the Waste Gate Isolation Toggle and opening the Waste Gate Bleed Toggle.
9. Reset the toggles for Waste Gate position Full open : Isolation Toggle Open/Bleed Toggle closed.

#### 12 Volt Battery Check

1. Unplug the battery charger and store the charger.
2. Throw the isolation switch.
3. Verify each start battery has a cold reading of 13.2 volts minimum. This ensures that the batteries are fully charged. Record Voltage:
4. Verify each ignition battery has a cold reading of 12.6 volts minimum. This ensures that the batteries are sufficiently charged. Record Voltage:

#### Fuel Supply

1. Verify Gravity and speed trim lines to engine skid. Open the ROVER side of the gravity system. Place the speed trim valve in the open position, rotated down. Shutting this valve will trim engine speed and eventually shut the engine down.
2. Purge the fuel Pump accumulator to charge with air and rig for remote valve operation.
3. Using the battery charger AC supply, plug in the fuel transfer pump and verify High and Low speed operation.
4. Check fuel level by sight glass and control panel gage, minimum  $\frac{3}{4}$  full. Fill as necessary.
5. Fill the seven gallon tank under the fuel cabinet, if required.
6. Check the entire fuel cabinet and hoses for leaks.
7. Have a full 5 gallon fuel can standing by in the fuel closet, if required.
8. Dry and position the skid drip pan and the fuel drain drip pan.

#### Oil Levels

1. Verify Rover engine oil level. Refill with single viscosity 10W oil as necessary up to half way between the high and low markings.
2. Safety wire the dipstick.
3. Verify Turbocharger oil level. Fill with 10W-30 oil as necessary as not to flood the turbo oil scavenge port. Visually check the condition of the oil.

#### Dyno Setup and Oil Cooler Process Water

1. Crack open the Turbocharger Lube Oil Cooler water supply tap.
2. Route system drain lines outside under the main overhead door.
3. Fully open the water supply to the Froude Dyno. Purge Dyno.
4. Verify the in-line Rota meter is reading 6.9 GPM. Adjust Dyno inlet and outlet valve to full open.
5. Verify the water brake is fully unloaded, that is, the geared handle is full to the CCW position.
6. Verify the gear lock remains disengaged.
7. Visually confirm gland leakage.
8. Confirm discharge flow from four drain lines. They are; 1.)The Rover oil cooler, 2.) The dyno, 3.) The dyno drip pan and 4.) The Turbocharger Lube Oil Cooler.

#### Water Recovery

1. Attach the Water Recovery Reservoir to the load cell.
2. Supply AC power to the drain pumps and turn them on. Verify rotation

### Inlet, Recirculation and Exhaust Start-up Check

1. Check the exhaust system to ensure all penetrations are covered and joints are tight.
2. Verify that the Boost Control Valve is fully open.
3. Verify that the Rover Inlet Isolation Valve is fully open
4. Verify the Waste Gate Valve is fully open.
5. Verify the Rover Recirculation Valve is fully shut.

### Engine room Preparation

#### Room Ventilation:

1. Open the main bay door about five feet (to marked line).
2. Turn on the lab ventilation fan and the compressor room fan.
3. Turn the air conditioning thermostat bypass, at the north wall, to “on”.

#### Lab Over-watch:

1. Check the lab area for debris that could be ingested into the engine or present a tripping hazard.
2. Attach the Safety Chain at the hall outside the Lab.
3. Move fire extinguishers to areas in the lab where they are readily accessible.
4. Visitor Policy: all visitors should be checked in, briefed, and supplied with safety equipment before the run set-up begins. Optimally, all visitors should be supplied with Listen-Only communication head gear. No late or unannounced visitors are allowed.
5. Put the scatter shields in place for turbocharged runs, if required.

### Gas Analysis and Data Acquisition

1. Refer to the gas analysis set up procedure, separate from this document.
2. Verify that all thermocouples are reading properly by both the analog and digital data acquisition systems. Confirm conformance to the instrumentation map. This should be completed a day in advance of the run.

3. Verify that all pressure taps are reading properly by both the analog and digital data acquisition systems. Confirm conformance to the instrumentation map. This should be completed a day in advance of the run.
4. Verify the analog pressure, temperature, and manometer reading legends are clearly displayed on the panel near the instruments.
5. Record the initial reading from the Water Recovery load cell on the Data Sheet.

#### ARU Setup

1. Check if the solution receiver is at least one quarter full. If it is lower than 1/4, see troubleshooting guide.
2. Check all the valve positions according to valve tag list.
3. Check closed V13 wide (pump bypass).
4. Record the initial Solution Receiver tank level.
5. Record the initial NH3 Receiver Tank level.
6. Set V14 shut (pump discharge).
7. V15 at 3-turn open, Set by Supplier (Mattingly) (col feed).
8. Adjust water valves V26 and V27 to get 2 gpm in condenser and 10 gpm in absorber. Record initial flows:
9. Turn power switch on. Panel lights should go from Red to Yellow until HRVG inlet air becomes hot. Then the Green light will come on starting the solution pump and opening the solenoid valves.

#### Video and Audio Recording

1. Set up the VCR in the lab. Run the cables to the control room to the video monitor.
2. Set up the microphone to record the communications loop. Hook this into the VCR sound input.
3. Insert a new VCR tape for the day's activity. Ensure tape is recording on E.P. (extended play).
4. Synchronize TIME and DATE.
5. Complete a system check to be sure that all the monitoring and recording systems are working correctly. This system is used to verify the data set switch points and aids in improving each subsequent runs through lessons learned.

#### Personnel Safety Equipment and Communications

1. All personnel should wear appropriate clothing for an environment where high temperature piping, heavy equipment and high speed rotating equipment exist, i.e., long sleeve shirt, long pants, closed-toe and –heel shoes, and no loose fitting items or jewelry. TURN OFF CELL PHONES.
2. Check all the communication gear. Check batteries. All units should be on the same channel and in Push-To-Talk (PTT) mode. All units should be on TX, not INT. Use channel A.
3. All personnel and visitors should have hearing protection, either communication sets or ear muffs.
4. All personnel and visitors should have eye protection.

APPENDIX C  
ADJUSTED EXPERIMENTAL DATA

Provided below is the reduced data for all of the successful Build 4 engine runs. Each engine run is identified as B4-X, where X represents the run number. Each run had between one and five separate trials. The reduced parameters shown were calculated after the data adjustments were made, according to the discussion in Chapter 5.

Table C-1. Data from runs B4-1 and B4-2.

Run	B4-1		B4-2		
Trial	1	2	1	2	3
<b>Main Air Inlet</b>					
Ambient Temperature (F)	69.3	70.7	84.9	86.5	87.8
Ambient Pressure (psia)	14.7	14.7	14.7	14.7	14.7
Ambient Humidity Ratio	0.0189	0.0189	0.0171	0.0174	0.0174
Mass Flow Rate (lbm/s)	0.00	0.00	0.00	0.00	0.00
<b>Low Pressure Compressor</b>					
Inlet Temperature (F)	96.0	96.0	95.6	97.3	98.7
Gamma	1.40	1.40	1.40	1.40	1.40
Shaft Power (hp)	2.8	4.3	8.9	7.9	13.0
Isentropic Efficiency (%)	54.9	54.8	66.6	71.0	73.3
Pressure Ratio	1.06	1.08	1.18	1.18	1.28
Flow Rate (lbm/s)	0.52	0.54	0.64	0.60	0.68
Corrected Flow Rate (lbm/s)	0.54	0.56	0.66	0.62	0.70
<b>High Pressure Compressor</b>					
Inlet Temperature (F)	76.9	77.7	76.6	79.7	89.2
Inlet Pressure (psia)	15.2	15.6	17.1	17.1	18.5
Adiabatic Exit Temperature (F)	330.4	330.3	327.3	329.9	339.2
Gamma	1.38	1.38	1.38	1.38	1.38
Shaft Power (hp)	115.4	119.2	131.0	130.9	139.4
Isentropic Efficiency (%)	70.8	71.3	71.5	71.7	70.2
Pressure Ratio	2.85	2.86	2.82	2.81	2.72
Total Gas Flow Rate (lbm/s)	1.31	1.35	1.49	1.49	1.59
Corrected Flow Rate (lbm/s)	1.29	1.30	1.31	1.31	1.30
<b>Combustor</b>					
Fuel Flow Rate (lbm/s)	0.018	0.019	0.020	0.020	0.020
Phi	0.50	0.49	0.44	0.47	0.43
Combustion Efficiency	91.7	91.7	96.6	96.6	97.3
Combustor Exit Temperature (F)	1472	1463	1485	1474	1480
<b>High Pressure Turbine</b>					
Inlet Temperature (F)	1429	1430	1414	1400	1419
Inlet Pressure (psia)	43.3	44.4	48.2	48.0	50.3
Gamma	1.31	1.31	1.32	1.32	1.32

Run	B4-1		B4-2		
Trial	1	2	1	2	3
Shaft Power (hp)	-180.0	-186.4	-204.1	-202.1	-211.4
Isentropic Efficiency (%)	85.0	85.0	85.0	85.0	85.0
Expansion Ratio	2.85	2.86	2.82	2.81	2.72
Corrected Flow Rate (lbm/s)	0.82	0.83	0.84	0.85	0.86
Recuperator					
Hot Side dT (F)	-176.6	-165.9	-120.4	-122.5	-136.1
Hot Side Heat Rate (Btu/s)	-78.5	-82.6	-88.5	-85.7	-89.9
Cold Side dT (F)	218.3	223.2	217.2	210.0	207.4
Cold Side Heat Rate (Btu/s)	72.6	76.7	82.5	79.9	84.2
Heat to Ambient (Btu/s)	-5.9	-5.9	-5.9	-5.8	-5.7
Effectiveness	0.32	0.32	0.32	0.31	0.32
Low Pressure Turbine					
Inlet Temperature (F)	899	910	938	926	937
Inlet Pressure (psia)	17.5	17.9	19.4	19.1	20.5
Gamma	1.33	1.33	1.34	1.34	1.34
Shaft Power (hp)	-2.8	-4.3	-8.9	-7.9	-13.0
Isentropic Efficiency (%)	35.8	45.5	53.2	52.1	58.7
Expansion Ratio	1.19	1.21	1.32	1.30	1.39
Flow Rate (lbm/s)	0.36	0.39	0.47	0.45	0.52
Corrected Flow Rate (lbm/s)	0.49	0.52	0.58	0.57	0.61
Hot Gas Cooler					
Gas Side dT (F)	-427.7	-431.6	-431.8	-412.6	-410.4
Gas Side Heat Rate (Btu/s)	-91.4	-94.1	-98.8	-98.0	-99.9
Warm Gas Cooler					
Gas Side dT (F)	-393.4	-389.9	-405.6	-398.5	-405.3
Water Side dT (F)	11.0	12.1	12.5	13.3	14.1
Gas Side Heat Rate (Btu/s)	-86.8	-85.6	-91.9	-93.6	-96.4
Water Side Heat Rate (Btu/s)	59.1	61.5	65.8	69.1	73.2
Heat Loss to Ambient (Btu/s)	-27.7	-24.1	-26.1	-24.4	-23.2
Effectiveness	0.73	0.71	0.70	0.69	0.68
Cold Gas Cooler					
Gas Side dT (F)	-49.9	-52.0	-58.6	-61.2	-58.3
Gas Side Heat Rate (Btu/s)	-23.1	-22.2	-25.1	-25.9	-25.2
Overall Performance					
R	1.53	1.51	1.35	1.48	1.35
Power (hp)	64.5	67.2	73.1	71.2	72.0
Thermal Efficiency (%)	13.90	13.97	14.40	14.05	13.64
Average Water Extraction Rate (gph)	5.81	4.00	2.88	2.69	1.86
Average Fuel Flow Rate (gph)	9.21	9.54	10.08	10.06	10.47

Table C-2. Data from runs B4-3 and B4-5.

Run	B4-3			B4-5	
Trial	1	2	3	1	2
<b>Main Air Inlet</b>					
Ambient Temperature (F)	85.2	86.5	87.2	86.0	87.0
Ambient Pressure (psia)	14.8	14.8	14.8	14.7	14.7
Ambient Humidity Ratio	0.0186	0.0186	0.0186	0.0169	0.0169
Mass Flow Rate (lbm/s)	0.00	0.00	0.00	0.00	0.00
<b>Low Pressure Compressor</b>					
Inlet Temperature (F)	95.0	95.0	95.0	95.5	97.8
Gamma	1.39	1.39	1.40	1.40	1.40
Shaft Power (hp)	16.7	18.3	2.7	15.8	17.1
Isentropic Efficiency (%)	72.4	71.4	39.4	77.7	78.8
Pressure Ratio	1.34	1.36	1.04	1.37	1.39
Flow Rate (lbm/s)	0.73	0.74	0.50	0.69	0.70
Corrected Flow Rate (lbm/s)	0.75	0.77	0.51	0.71	0.73
<b>High Pressure Compressor</b>					
Inlet Temperature (F)	93.6	102.7	71.5	97.2	108.3
Inlet Pressure (psia)	19.3	19.7	15.0	19.8	20.1
Adiabatic Exit Temperature (F)	342.4	350.6	326.3	345.9	355.9
Gamma	1.38	1.38	1.38	1.38	1.38
Shaft Power (hp)	145.0	144.4	116.9	149.1	147.9
Isentropic Efficiency (%)	70.7	70.6	70.9	69.5	69.4
Pressure Ratio	2.70	2.65	2.87	2.65	2.60
Total Gas Flow Rate (lbm/s)	1.66	1.66	1.31	1.71	1.70
Corrected Flow Rate (lbm/s)	1.30	1.29	1.30	1.31	1.30
<b>Combustor</b>					
Fuel Flow Rate (lbm/s)	0.021	0.021	0.018	0.021	0.021
Phi	0.41	0.40	0.52	0.44	0.43
Combustion Efficiency	97.6	98.0	96.1	96.2	97.3
Combustor Exit Temperature (F)	1477	1495	1514	1435	1458
<b>High Pressure Turbine</b>					
Inlet Temperature (F)	1423	1437	1406	1398	1416
Inlet Pressure (psia)	52.3	52.2	43.1	52.4	52.3
Gamma	1.32	1.32	1.32	1.32	1.32
Shaft Power (hp)	-220.4	-218.1	-181.7	-219.7	-216.8
Isentropic Efficiency (%)	85.0	85.0	85.0	85.0	85.0
Expansion Ratio	2.70	2.65	2.87	2.65	2.60
Corrected Flow Rate (lbm/s)	0.86	0.86	0.84	0.87	0.87
<b>Recuperator</b>					
Hot Side dT (F)	-128.5	-132.2	-127.4	-140.3	-143.8
Hot Side Heat Rate (Btu/s)	-91.5	-95.2	-75.9	-91.6	-93.7
Cold Side dT (F)	201.5	210.2	209.4	196.4	202.1
Cold Side Heat Rate (Btu/s)	85.5	89.2	69.9	85.7	87.9
Heat to Ambient (Btu/s)	-6.0	-6.0	-6.0	-5.9	-5.8
Effectiveness	0.32	0.32	0.30	0.32	0.32

Run	B4-3			B4-5	
Trial	1	2	3	1	2
<b>Low Pressure Turbine</b>					
Inlet Temperature (F)	950	964	921	923	941
Inlet Pressure (psia)	21.5	21.8	17.0	21.2	21.5
Gamma	1.34	1.34	1.34	1.34	1.34
Shaft Power (hp)	-16.7	-18.3	-2.7	-15.8	-17.1
Isentropic Efficiency (%)	61.4	63.1	21.6	61.5	61.7
Expansion Ratio	1.45	1.47	1.16	1.44	1.46
Flow Rate (lbm/s)	0.56	0.57	0.32	0.55	0.57
Corrected Flow Rate (lbm/s)	0.63	0.64	0.46	0.63	0.63
<b>Hot Gas Cooler</b>					
Gas Side dT (F)	-418.5	-420.4	-409.8	-383.6	-389.9
Gas Side Heat Rate (Btu/s)	-104.0	-102.6	-90.5	-104.4	-103.5
<b>Warm Gas Cooler</b>					
Gas Side dT (F)	-412.2	-418.0	-399.8	-424.7	-435.6
Water Side dT (F)	14.8	15.0	11.7	16.2	16.3
Gas Side Heat Rate (Btu/s)	-100.1	-99.2	-91.8	-112.4	-112.1
Water Side Heat Rate (Btu/s)	74.0	75.1	65.2	79.1	81.8
Heat Loss to Ambient (Btu/s)	-26.0	-24.1	-26.6	-33.3	-30.4
Effectiveness	0.69	0.68	0.72	0.70	0.70
<b>Cold Gas Cooler</b>					
Gas Side dT (F)	-51.0	-46.2	-61.4	-46.1	-38.7
Gas Side Heat Rate (Btu/s)	-23.4	-21.0	-27.6	-21.5	-18.1
<b>Overall Performance</b>					
R	1.28	1.23	1.66	1.49	1.42
Power (hp)	75.4	73.7	64.8	70.5	68.9
Thermal Efficiency (%)	13.85	13.59	13.81	12.96	12.76
Average Water Extraction Rate (gph)	1.97	1.64	6.27	1.67	1.49
Average Fuel Flow Rate (gph)	10.80	10.76	9.31	10.80	10.71

Table C-3. Data from runs B4-7 and B4-8

Run	B4-7				B4-8
Trial	1	2	3	4	1
<b>Main Air Inlet</b>					
Ambient Temperature (F)	85.1	86.0	87.7	88.1	84.2
Ambient Pressure (psia)	14.8	14.8	14.8	14.8	14.7
Ambient Humidity Ratio	0.0186	0.0186	0.0190	0.0200	0.0189
Mass Flow Rate (lbm/s)	0.00	0.00	0.00	0.00	0.00
<b>Low Pressure Compressor</b>					
Inlet Temperature (F)	90.3	92.5	93.3	94.1	90.1
Gamma	1.40	1.40	1.40	1.39	1.39
Shaft Power (hp)	18.1	13.3	14.9	15.6	27.7
Isentropic Efficiency (%)	69.8	72.5	73.3	73.3	69.6
Pressure Ratio	1.36	1.30	1.33	1.34	1.48
Flow Rate (lbm/s)	0.73	0.65	0.67	0.68	0.86
Corrected Flow Rate (lbm/s)	0.75	0.66	0.69	0.70	0.88
<b>High Pressure Compressor</b>					
Inlet Temperature (F)	88.7	92.2	92.3	93.3	89.5
Inlet Pressure (psia)	19.7	18.9	19.3	19.5	21.4
Adiabatic Exit Temperature (F)	337.5	342.3	339.4	340.1	331.7
Gamma	1.38	1.38	1.38	1.38	1.39
Shaft Power (hp)	151.2	146.0	147.1	148.1	157.5
Isentropic Efficiency (%)	70.7	70.3	71.0	70.8	70.5
Pressure Ratio	2.73	2.71	2.71	2.69	2.65
Total Gas Flow Rate (lbm/s)	1.73	1.66	1.69	1.70	1.85
Corrected Flow Rate (lbm/s)	1.33	1.33	1.33	1.33	1.31
<b>Combustor</b>					
Fuel Flow Rate (lbm/s)	0.021	0.020	0.023	0.024	0.023
Phi	0.42	0.46	0.49	0.50	0.38
Combustion Efficiency	96.1	94.9	96.8	97.2	99.6
Combustor Exit Temperature (F)	1427	1417	1521	1545	1473
<b>High Pressure Turbine</b>					
Inlet Temperature (F)	1387	1373	1414	1415	1418
Inlet Pressure (psia)	53.6	51.2	52.2	52.5	56.6
Gamma	1.32	1.32	1.32	1.32	1.32
Shaft Power (hp)	-226.8	-215.2	-223.4	-224.2	-240.9
Isentropic Efficiency (%)	85.0	85.0	85.0	85.0	85.0
Expansion Ratio	2.73	2.71	2.71	2.69	2.65
Corrected Flow Rate (lbm/s)	0.86	0.86	0.89	0.90	0.88
<b>Recuperator</b>					
Hot Side dT (F)	-98.3	-98.5	-108.3	-105.3	-109.4
Hot Side Heat Rate (Btu/s)	-96.1	-90.6	-97.1	-98.0	-110.9
Cold Side dT (F)	203.3	198.9	210.3	210.7	221.0
Cold Side Heat Rate (Btu/s)	89.8	84.4	91.0	92.0	104.6
Heat to Ambient (Btu/s)	-6.3	-6.2	-6.1	-6.0	-6.3
Effectiveness	0.33	0.33	0.30	0.29	0.33

Run	B4-7				B4-8
Trial	1	2	3	4	1
<b>Low Pressure Turbine</b>					
Inlet Temperature (F)	947	937	964	970	971
Inlet Pressure (psia)	21.6	20.3	20.8	21.0	23.9
Gamma	1.34	1.34	1.34	1.34	1.34
Shaft Power (hp)	-18.1	-13.3	-14.9	-15.6	-27.7
Isentropic Efficiency (%)	64.4	62.7	63.4	63.9	67.6
Expansion Ratio	1.46	1.38	1.41	1.42	1.62
Flow Rate (lbm/s)	0.57	0.51	0.52	0.53	0.65
Corrected Flow Rate (lbm/s)	0.64	0.60	0.61	0.62	0.67
<b>Hot Gas Cooler</b>					
Gas Side dT (F)	-391.9	-390.7	-394.5	-393.2	-413.8
Gas Side Heat Rate (Btu/s)	-104.1	-105.3	-107.5	-107.6	-109.5
<b>Warm Gas Cooler</b>					
Gas Side dT (F)	-412.5	-411.0	-437.4	-441.0	-422.0
Water Side dT (F)	16.1	15.8	15.8	16.2	16.3
Gas Side Heat Rate (Btu/s)	-105.1	-106.1	-114.1	-115.5	-107.1
Water Side Heat Rate (Btu/s)	78.6	78.6	87.2	92.3	79.2
Heat Loss to Ambient (Btu/s)	-26.4	-27.5	-26.9	-23.2	-27.9
Effectiveness	0.66	0.67	0.69	0.69	0.67
<b>Cold Gas Cooler</b>					
Gas Side dT (F)	-71.0	-58.9	-59.5	-60.6	-76.8
Gas Side Heat Rate (Btu/s)	-32.0	-25.5	-26.8	-27.5	-37.7
<b>Overall Performance</b>					
R	1.37	1.57	1.52	1.51	1.16
Power (hp)	75.6	69.1	76.3	76.1	83.4
Thermal Efficiency (%)	13.72	13.04	12.77	12.39	14.13
Average Water Extraction Rate (gph)	0.81	0.66	0.96	0.94	1.24
Average Fuel Flow Rate (gph)	10.94	10.52	11.86	12.20	11.71

Table C-4. Data from runs B4-10 and B4-11.

Run	B4-10		B4-11	
Trial	1	2	1	2
<b>Main Air Inlet</b>				
Ambient Temperature (F)	86.1	86.6	83.8	84.2
Ambient Pressure (psia)	14.8	14.8	14.8	14.8
Ambient Humidity Ratio	0.0186	0.0183	0.0169	0.0174
Mass Flow Rate (lbm/s)	0.00	0.00	0.00	0.00
<b>Low Pressure Compressor</b>				
Inlet Temperature (F)	93.0	93.9	91.5	92.5
Gamma	1.40	1.40	1.40	1.40
Shaft Power (hp)	14.2	14.3	16.8	17.8
Isentropic Efficiency (%)	67.3	67.9	67.7	68.0
Pressure Ratio	1.29	1.30	1.34	1.36
Flow Rate (lbm/s)	0.65	0.65	0.69	0.70
Corrected Flow Rate (lbm/s)	0.67	0.67	0.71	0.72
<b>High Pressure Compressor</b>				
Inlet Temperature (F)	88.2	89.4	88.8	91.2
Inlet Pressure (psia)	19.1	19.2	18.9	20.0
Adiabatic Exit Temperature (F)	339.3	340.5	338.7	340.7
Gamma	1.38	1.38	1.38	1.38
Shaft Power (hp)	153.3	152.3	148.5	150.1
Isentropic Efficiency (%)	70.6	70.3	71.2	71.5
Pressure Ratio	2.75	2.73	2.75	2.75
Total Gas Flow Rate (lbm/s)	1.73	1.72	1.69	1.71
Corrected Flow Rate (lbm/s)	1.37	1.36	1.29	1.29
<b>Combustor</b>				
Fuel Flow Rate (lbm/s)	0.021	0.022	0.022	0.023
Phi	0.47	0.48	0.47	0.47
Combustion Efficiency	94.4	95.2	97.4	97.1
Combustor Exit Temperature (F)	1399	1435	1500	1496
<b>High Pressure Turbine</b>				
Inlet Temperature (F)	1354	1363	1409	1403
Inlet Pressure (psia)	52.5	52.4	54.4	55.0
Gamma	1.32	1.32	1.32	1.32
Shaft Power (hp)	-225.0	-223.4	-225.9	-227.5
Isentropic Efficiency (%)	85.0	85.0	85.0	85.0
Expansion Ratio	2.75	2.73	2.75	2.75
Corrected Flow Rate (lbm/s)	0.88	0.88	0.85	0.85
<b>Recuperator</b>				
Hot Side dT (F)	-92.3	-95.4	-99.4	-99.0
Hot Side Heat Rate (Btu/s)	-93.6	-94.2	-97.3	-98.3
Cold Side dT (F)	197.3	199.9	210.8	210.9
Cold Side Heat Rate (Btu/s)	87.5	88.2	91.1	92.2
Heat to Ambient (Btu/s)	-6.1	-6.1	-6.2	-6.2
Effectiveness	0.32	0.31	0.30	0.30

Run	B4-10		B4-11	
Trial	1	2	1	2
<b>Low Pressure Turbine</b>				
Inlet Temperature (F)	923	930	963	959
Inlet Pressure (psia)	20.7	20.8	21.3	21.5
Gamma	1.34	1.34	1.34	1.34
Shaft Power (hp)	-14.2	-14.3	-16.8	-17.8
Isentropic Efficiency (%)	63.8	63.7	63.3	63.8
Expansion Ratio	1.39	1.39	1.44	1.46
Flow Rate (lbm/s)	0.52	0.52	0.55	0.56
Corrected Flow Rate (lbm/s)	0.61	0.61	0.63	0.63
<b>Hot Gas Cooler</b>				
Gas Side dT (F)	-370.2	-375.4	-384.3	-382.9
Gas Side Heat Rate (Btu/s)	-106.6	-106.8	-103.0	-103.3
<b>Warm Gas Cooler</b>				
Gas Side dT (F)	-417.2	-417.9	-442.3	-434.2
Water Side dT (F)	16.4	16.1	17.7	22.5
Gas Side Heat Rate (Btu/s)	-115.8	-114.4	-113.9	-112.7
Water Side Heat Rate (Btu/s)	81.4	82.6	85.2	82.6
Heat Loss to Ambient (Btu/s)	-34.3	-31.8	-28.7	-30.1
Effectiveness	0.68	0.68	0.69	0.68
<b>Cold Gas Cooler</b>				
Gas Side dT (F)	-64.1	-65.8	-67.2	-69.0
Gas Side Heat Rate (Btu/s)	-28.8	-29.2	-29.8	-30.9
<b>Overall Performance</b>				
R	1.66	1.63	1.46	1.44
Power (hp)	71.7	71.1	77.4	77.5
Thermal Efficiency (%)	12.96	12.56	13.32	13.11
Average Water Extraction Rate (gph)	0.88	0.75	1.02	1.08
Average Fuel Flow Rate (gph)	10.98	11.23	11.53	11.73

Table C-5. Data from run B4-12.

Run	B4-12			
Trial	1	2	3	4
<b>Main Air Inlet</b>				
Ambient Temperature (F)	84.4	85.7	86.5	87.1
Ambient Pressure (psia)	14.8	14.8	14.8	14.8
Ambient Humidity Ratio	0.0180	0.0183	0.0186	0.0186
Mass Flow Rate (lbm/s)	0.00	0.00	0.00	0.00
<b>Low Pressure Compressor</b>				
Inlet Temperature (F)	91.3	93.7	95.0	95.8
Gamma	1.39	1.39	1.39	1.39
Shaft Power (hp)	22.2	24.1	24.9	26.3
Isentropic Efficiency (%)	67.6	68.7	69.1	69.3
Pressure Ratio	1.41	1.45	1.46	1.48
Flow Rate (lbm/s)	0.76	0.78	0.79	0.80
Corrected Flow Rate (lbm/s)	0.78	0.80	0.81	0.82
<b>High Pressure Compressor</b>				
Inlet Temperature (F)	92.6	99.5	99.8	101.9
Inlet Pressure (psia)	20.9	21.4	21.6	21.9
Adiabatic Exit Temperature (F)	342.8	350.1	349.2	351.6
Gamma	1.38	1.38	1.38	1.38
Shaft Power (hp)	157.1	157.9	158.0	157.8
Isentropic Efficiency (%)	70.3	69.5	69.7	69.6
Pressure Ratio	2.71	2.66	2.65	2.64
Total Gas Flow Rate (lbm/s)	1.78	1.79	1.80	1.79
Corrected Flow Rate (lbm/s)	1.30	1.28	1.27	1.25
<b>Combustor</b>				
Fuel Flow Rate (lbm/s)	0.023	0.023	0.023	0.023
Phi	0.43	0.42	0.41	0.41
Combustion Efficiency	95.8	96.4	96.5	96.5
Combustor Exit Temperature (F)	1448	1457	1460	1473
<b>High Pressure Turbine</b>				
Inlet Temperature (F)	1392	1398	1399	1399
Inlet Pressure (psia)	56.5	56.8	57.2	57.7
Gamma	1.32	1.32	1.32	1.32
Shaft Power (hp)	-233.5	-231.1	-232.3	-230.6
Isentropic Efficiency (%)	85.0	85.0	85.0	85.0
Expansion Ratio	2.71	2.66	2.65	2.64
Corrected Flow Rate (lbm/s)	0.85	0.85	0.85	0.84
<b>Recuperator</b>				
Hot Side dT (F)	-98.1	-105.1	-102.1	-97.6
Hot Side Heat Rate (Btu/s)	-98.8	-97.9	-98.6	-98.6
Cold Side dT (F)	202.8	200.5	201.0	201.9
Cold Side Heat Rate (Btu/s)	92.5	91.8	92.6	92.7
Heat to Ambient (Btu/s)	-6.2	-6.1	-6.0	-5.9
Effectiveness	0.32	0.32	0.32	0.31

Run	B4-12			
Trial	1	2	3	4
<b>Low Pressure Turbine</b>				
Inlet Temperature (F)	954	957	962	968
Inlet Pressure (psia)	22.6	23.1	23.3	23.5
Gamma	1.34	1.34	1.34	1.34
Shaft Power (hp)	-22.2	-24.1	-24.9	-26.3
Isentropic Efficiency (%)	65.2	65.6	65.8	66.5
Expansion Ratio	1.53	1.56	1.57	1.59
Flow Rate (lbm/s)	0.61	0.63	0.64	0.65
Corrected Flow Rate (lbm/s)	0.66	0.67	0.67	0.67
<b>Hot Gas Cooler</b>				
Gas Side dT (F)	-382.2	-392.4	-389.2	-394.8
Gas Side Heat Rate (Btu/s)	-104.6	-105.9	-105.2	-104.8
<b>Warm Gas Cooler</b>				
Gas Side dT (F)	-408.1	-403.2	-404.4	-402.2
Water Side dT (F)	17.7	18.4	18.7	18.9
Gas Side Heat Rate (Btu/s)	-108.1	-105.0	-105.5	-103.2
Water Side Heat Rate (Btu/s)	81.7	83.4	84.7	85.8
Heat Loss to Ambient (Btu/s)	-26.3	-21.6	-20.8	-17.4
Effectiveness	0.65	0.64	0.64	0.64
<b>Cold Gas Cooler</b>				
Gas Side dT (F)	-82.4	-78.9	-83.4	-84.3
Gas Side Heat Rate (Btu/s)	-37.8	-36.1	-38.3	-38.7
<b>Overall Performance</b>				
R	1.35	1.30	1.29	1.25
Power (hp)	76.4	73.2	74.3	72.9
Thermal Efficiency (%)	13.05	12.56	12.66	12.27
Average Water Extraction Rate (gph)	1.07	0.85	0.85	0.90
Average Fuel Flow Rate (gph)	11.62	11.56	11.65	11.78

Table C-6. Data from run B4-14.

Run	B4-14			
Trial	2	3	4	5
<b>Main Air Inlet</b>				
Ambient Temperature (F)	84.3	85.8	86.8	88.6
Ambient Pressure (psia)	14.7	14.7	14.7	14.7
Ambient Humidity Ratio	0.0171	0.0176	0.0183	0.0181
Mass Flow Rate (lbm/s)	0.12	0.11	0.00	0.00
<b>Low Pressure Compressor</b>				
Inlet Temperature (F)	89.8	92.9	94.5	97.5
Gamma	1.40	1.40	1.40	1.39
Shaft Power (hp)	5.1	5.3	12.2	14.5
Isentropic Efficiency (%)	34.8	33.2	55.9	66.2
Pressure Ratio	1.06	1.06	1.20	1.30
Flow Rate (lbm/s)	0.55	0.55	0.66	0.65
Corrected Flow Rate (lbm/s)	0.57	0.57	0.68	0.67
<b>High Pressure Compressor</b>				
Inlet Temperature (F)	72.3	74.0	81.5	91.0
Inlet Pressure (psia)	15.6	15.6	17.7	19.1
Adiabatic Exit Temperature (F)	327.4	329.2	332.7	342.9
Gamma	1.39	1.39	1.38	1.38
Shaft Power (hp)	125.7	123.7	140.1	148.0
Isentropic Efficiency (%)	72.1	72.3	72.3	70.6
Pressure Ratio	2.90	2.90	2.83	2.74
Total Gas Flow Rate (lbm/s)	1.41	1.38	1.59	1.67
Corrected Flow Rate (lbm/s)	1.34	1.32	1.35	1.32
<b>Combustor</b>				
Fuel Flow Rate (lbm/s)	0.019	0.019	0.021	0.021
Phi	0.40	0.40	0.45	0.47
Combustion Efficiency	99.7	99.9	97.6	95.1
Combustor Exit Temperature (F)	1503	1528	1473	1425
<b>High Pressure Turbine</b>				
Inlet Temperature (F)	1373	1388	1383	1367
Inlet Pressure (psia)	45.4	45.3	50.1	52.5
Gamma	1.32	1.32	1.32	1.32
Shaft Power (hp)	-192.7	-191.0	-214.3	-217.8
Isentropic Efficiency (%)	85.0	85.0	85.0	85.0
Expansion Ratio	2.90	2.90	2.83	2.74
Corrected Flow Rate (lbm/s)	0.85	0.84	0.86	0.85
<b>Recuperator</b>				
Hot Side dT (F)	-127.0	-112.5	-85.0	-101.5
Hot Side Heat Rate (Btu/s)	-83.4	-83.4	-92.5	-89.6
Cold Side dT (F)	215.5	219.6	213.8	196.3
Cold Side Heat Rate (Btu/s)	77.0	77.3	86.5	83.9
Heat to Ambient (Btu/s)	-6.4	-6.1	-6.0	-5.8
Effectiveness	0.30	0.30	0.31	0.32

Run	B4-14			
Trial	2	3	4	5
<b>Low Pressure Turbine</b>				
Inlet Temperature (F)	889	916	947	925
Inlet Pressure (psia)	17.9	17.9	20.1	20.6
Gamma	1.34	1.34	1.34	1.34
Shaft Power (hp)	-5.1	-5.3	-12.2	-14.5
Isentropic Efficiency (%)	-3.2	25.7	59.8	63.4
Expansion Ratio	1.21	1.22	1.37	1.41
Flow Rate (lbm/s)	0.39	0.39	0.50	0.53
Corrected Flow Rate (lbm/s)	0.52	0.52	0.60	0.61
<b>Hot Gas Cooler</b>				
Gas Side dT (F)	-411.1	-417.3	-404.0	-374.5
Gas Side Heat Rate (Btu/s)	-81.0	-79.7	-99.7	-102.0
<b>Warm Gas Cooler</b>				
Gas Side dT (F)	-390.1	-391.7	-420.2	-398.2
Water Side dT (F)	11.7	12.6	15.6	17.5
Gas Side Heat Rate (Btu/s)	-76.6	-73.8	-101.0	-104.7
Water Side Heat Rate (Btu/s)	55.6	59.6	72.9	81.3
Heat Loss to Ambient (Btu/s)	-21.0	-14.2	-28.1	-23.4
Effectiveness	0.70	0.68	0.68	0.64
<b>Cold Gas Cooler</b>				
Gas Side dT (F)	-52.6	-60.5	-67.1	-80.8
Gas Side Heat Rate (Btu/s)	-20.0	-21.4	-28.5	-34.4
<b>Overall Performance</b>				
R	1.11	1.08	1.39	1.58
Power (hp)	67.0	67.3	74.2	69.7
Thermal Efficiency (%)	13.86	13.88	13.85	12.86
Average Water Extraction Rate (gph)	2.64	1.94	1.71	0.77
Average Fuel Flow Rate (gph)	9.59	9.62	10.64	10.76

Table C-7. Data from runs B4-15 and B4-16

Run	B4-15		B4-16	
Trial	1	2	3	1
<b>Main Air Inlet</b>				
Ambient Temperature (F)	83.0	86.1	86.5	85.1
Ambient Pressure (psia)	14.7	14.7	14.7	14.7
Ambient Humidity Ratio	0.0166	0.0171	0.0171	0.0186
Mass Flow Rate (lbm/s)	0.12	0.00	0.00	0.13
<b>Low Pressure Compressor</b>				
Inlet Temperature (F)	88.3	93.9	94.8	91.3
Gamma	1.40	1.40	1.39	1.40
Shaft Power (hp)	5.2	16.5	24.0	5.0
Isentropic Efficiency (%)	30.7	61.6	64.6	36.7
Pressure Ratio	1.06	1.29	1.41	1.06
Flow Rate (lbm/s)	0.54	0.70	0.79	0.55
Corrected Flow Rate (lbm/s)	0.56	0.72	0.81	0.56
<b>High Pressure Compressor</b>				
Inlet Temperature (F)	70.9	85.9	91.0	72.6
Inlet Pressure (psia)	15.5	19.0	20.7	15.6
Adiabatic Exit Temperature (F)	326.7	337.3	340.7	327.6
Gamma	1.39	1.38	1.38	1.39
Shaft Power (hp)	124.4	146.9	158.4	126.7
Isentropic Efficiency (%)	71.9	70.7	70.5	71.8
Pressure Ratio	2.91	2.76	2.71	2.89
Total Gas Flow Rate (lbm/s)	1.39	1.66	1.80	1.42
Corrected Flow Rate (lbm/s)	1.33	1.32	1.32	1.35
<b>Combustor</b>				
Fuel Flow Rate (lbm/s)	0.019	0.021	0.022	0.019
Phi	0.41	0.43	0.41	0.41
Combustion Efficiency	99.6	96.3	96.5	99.6
Combustor Exit Temperature (F)	1520	1456	1438	1510
<b>High Pressure Turbine</b>				
Inlet Temperature (F)	1382	1403	1406	1372
Inlet Pressure (psia)	45.2	52.5	56.3	45.1
Gamma	1.32	1.32	1.32	1.32
Shaft Power (hp)	-191.7	-222.4	-238.5	-193.4
Isentropic Efficiency (%)	85.0	85.0	85.0	85.0
Expansion Ratio	2.91	2.76	2.71	2.89
Corrected Flow Rate (lbm/s)	0.85	0.85	0.86	0.86
<b>Recuperator</b>				
Hot Side dT (F)	-113.3	-96.3	-100.8	-97.3
Hot Side Heat Rate (Btu/s)	-82.2	-94.1	-100.4	-83.8
Cold Side dT (F)	214.5	207.2	204.7	215.0
Cold Side Heat Rate (Btu/s)	75.8	88.0	94.4	77.5
Heat to Ambient (Btu/s)	-6.5	-6.1	-6.0	-6.2
Effectiveness	0.30	0.32	0.33	0.30

Run	B4-15		B4-16	
Trial	1	2	3	1
<b>Low Pressure Turbine</b>				
Inlet Temperature (F)	910	959	961	919
Inlet Pressure (psia)	17.7	21.0	22.8	17.9
Gamma	1.34	1.34	1.34	1.34
Shaft Power (hp)	-5.2	-16.5	-24.0	-5.0
Isentropic Efficiency (%)	55.1	64.5	66.7	44.3
Expansion Ratio	1.21	1.43	1.55	1.22
Flow Rate (lbm/s)	0.38	0.54	0.62	0.39
Corrected Flow Rate (lbm/s)	0.52	0.62	0.67	0.52
<b>Hot Gas Cooler</b>				
Gas Side dT (F)	-410.0	-390.4	-385.6	-415.0
Gas Side Heat Rate (Btu/s)	-79.8	-100.2	-104.7	-83.0
<b>Warm Gas Cooler</b>				
Gas Side dT (F)	-396.1	-407.0	-406.6	-399.2
Water Side dT (F)	10.7	16.2	17.9	10.3
Gas Side Heat Rate (Btu/s)	-77.0	-100.9	-106.5	-80.8
Water Side Heat Rate (Btu/s)	59.0	80.1	84.7	61.6
Heat Loss to Ambient (Btu/s)	-18.0	-20.8	-21.8	-19.3
Effectiveness	0.70	0.64	0.64	0.70
<b>Cold Gas Cooler</b>				
Gas Side dT (F)	-57.1	-89.0	-93.9	-58.2
Gas Side Heat Rate (Btu/s)	-21.4	-37.9	-43.1	-21.7
<b>Overall Performance</b>				
R	1.11	1.37	1.29	1.12
Power (hp)	67.2	75.5	80.2	66.7
Thermal Efficiency (%)	13.82	13.81	13.89	13.60
Average Water Extraction Rate (gph)	2.78	0.96	0.85	3.16
Average Fuel Flow Rate (gph)	9.65	10.85	11.45	9.73

Table C-8. Data from run B4-17.

Run	B4-17	
Trial	1	2
<b>Main Air Inlet</b>		
Ambient Temperature (F)	86.2	89.2
Ambient Pressure (psia)	14.7	14.7
Ambient Humidity Ratio	0.0177	0.0180
Mass Flow Rate (lbm/s)	0.00	0.00
<b>Low Pressure Compressor</b>		
Inlet Temperature (F)	93.1	96.3
Gamma	1.40	1.39
Shaft Power (hp)	9.2	19.9
Isentropic Efficiency (%)	47.6	61.2
Pressure Ratio	1.14	1.33
Flow Rate (lbm/s)	0.62	0.75
Corrected Flow Rate (lbm/s)	0.64	0.78
<b>High Pressure Compressor</b>		
Inlet Temperature (F)	78.1	84.8
Inlet Pressure (psia)	16.7	19.6
Adiabatic Exit Temperature (F)	330.4	334.9
Gamma	1.38	1.38
Shaft Power (hp)	133.4	150.9
Isentropic Efficiency (%)	72.6	70.9
Pressure Ratio	2.87	2.76
Total Gas Flow Rate (lbm/s)	1.51	1.72
Corrected Flow Rate (lbm/s)	1.35	1.32
<b>Combustor</b>		
Fuel Flow Rate (lbm/s)	0.020	0.021
Phi	0.46	0.41
Combustion Efficiency	95.7	96.2
Combustor Exit Temperature (F)	1463	1444
<b>High Pressure Turbine</b>		
Inlet Temperature (F)	1377	1415
Inlet Pressure (psia)	48.0	53.9
Gamma	1.32	1.32
Shaft Power (hp)	-204.8	-231.5
Isentropic Efficiency (%)	85.0	85.0
Expansion Ratio	2.87	2.76
Corrected Flow Rate (lbm/s)	0.85	0.86
<b>Recuperator</b>		
Hot Side dT (F)	-73.6	-101.6
Hot Side Heat Rate (Btu/s)	-89.8	-98.0
Cold Side dT (F)	218.3	210.0
Cold Side Heat Rate (Btu/s)	83.7	92.1
Heat to Ambient (Btu/s)	-6.1	-5.9
Effectiveness	0.32	0.33

Run	B4-17	
Trial	1	2
<b>Low Pressure Turbine</b>		
Inlet Temperature (F)	950	963
Inlet Pressure (psia)	19.1	21.9
Gamma	1.34	1.34
Shaft Power (hp)	-9.2	-19.9
Isentropic Efficiency (%)	59.2	65.2
Expansion Ratio	1.30	1.49
Flow Rate (lbm/s)	0.45	0.58
Corrected Flow Rate (lbm/s)	0.57	0.65
<b>Hot Gas Cooler</b>		
Gas Side dT (F)	-405.6	-401.0
Gas Side Heat Rate (Btu/s)	-96.0	-103.7
<b>Warm Gas Cooler</b>		
Gas Side dT (F)	-433.1	-429.5
Water Side dT (F)	14.1	15.2
Gas Side Heat Rate (Btu/s)	-100.8	-108.0
Water Side Heat Rate (Btu/s)	76.2	81.4
Heat Loss to Ambient (Btu/s)	-24.6	-26.6
Effectiveness	0.71	0.68
<b>Cold Gas Cooler</b>		
Gas Side dT (F)	-58.6	-79.6
Gas Side Heat Rate (Btu/s)	-23.9	-35.3
<b>Overall Performance</b>		
R	1.42	1.29
Power (hp)	71.4	80.6
Thermal Efficiency (%)	13.84	14.49
Average Water Extraction Rate (gph)	2.15	1.40
Average Fuel Flow Rate (gph)	10.24	11.04

## LIST OF REFERENCES

- [1] Gasparovic, N., 1968, "The Advantage of Semi-Closed Cycle Gas Turbines for Naval Ship Propulsion," *Naval Engineers Journal* **80**, April 1968, pp. 275-281, 333
- [2] Nemeč, T. S., 1995, "Thermodynamic Design Point Study of a Semi-Closed Recuperated Intercooled Gas Turbine Combined with a Rankine Bottoming Cycle," Master's Thesis, Dept. of Mechanical Engineering, University of Florida.
- [3] Landon, J. C., 1996, "Design and Off-Design Point Study of Two Regenerative Feedback Gas Turbine Engines for Marine Applications," Master's Thesis, Dept. of Mechanical Engineering, University of Florida.
- [4] Daniaš, G. E. , 1998, "Design and Off-Design Point Study of Two Regenerative Feedback Gas Turbine Engines for Helicopter Applications," Master's Thesis, Dept. of Mechanical Engineering, University of Florida.
- [5] MacFarlane, R. S., 1997, "A Study of the Impact of Water Extraction on the Regenerative Feedback Turbine Engine Cycle," Master's Thesis, Dept. of Mechanical Engineering, University of Florida.
- [6] Muley, N. S., 2002, "Effect of Exhaust Gas Recirculation on Thermal NO<sub>x</sub> Formation Rate in a Gas Turbine Engine," Master's Thesis, Dept. of Mechanical Engineering, University of Florida.
- [7] Boza, J. J., 2003, "Performance of a Semi-Closed Gas Turbine and Absorption Refrigeration Combined Cycle," Master's Thesis, Dept. of Mechanical Engineering, University of Florida.
- [8] Khan, J., 2006, "Design and Optimization of a Distributed Generation System with the Production of Water and Refrigeration," Doctoral Dissertation, Dept. of Mechanical Engineering, University of Florida.
- [9] Lear, W. E., Laganelli, A. L., 1999, "High Pressure Regenerative Turbine Engine: 21<sup>st</sup> Century Propulsion," Final Test Report for Contract No. NAS3-27396.
- [10] Crittenden, J. F., Lear, W. E., Azzazy, M., 1999, "Exploratory Design of a Depleted Oxygen Gas Turbine Combustor," Final Report for Contract No. NAS3-27759.
- [11] Pringle, D. S., 1972, "Testing a Small Gas Turbine In the Laboratory Shop," *Sawyer's Gas Turbine Engineering Handbook*, Vol. III, Gas Turbine Publications, Inc.
- [12] Lear, W. E., 2006, "Test Report for a Novel Combined Cycle Turbine Engine with Water Harvesting," Test Report for Subcontract to Phase II SBIR Contract No. A03-037.

- [13] Brown, D., 2005, Internal Report for US Army Phase II SBIR Contract No. A03-037.
- [14] Gater, R. A., 2002, *Engineering Thermodynamics—Foundation Topics*, Textbook Published by Author.
- [15] Incropera, F. P., DeWitt, D. P., 2002, *Fundamentals of Heat and Mass Transfer*, 5<sup>th</sup> Edition, John Wiley & Sons, New York.
- [16] 1958, *Rover Gas Turbine—Service Literature*, Rover Gas Turbines Ltd., Solihull Warwickshire England, Publication No. SP/101/758.
- [17] Crittenden, J. F., 1999, “Dilute, Kinetically Controlled Combustion Efficiency Prediction for Recirculating Semi-Closed Gas Turbine Cycles: A Non-Dimensional Approach Using the First Damkohler Number as a Parameter,” Master’s Thesis, Dept. of Mechanical Engineering, University of Florida, pp. 56-57.
- [18] Holman, J. P. 2001, *Experimental Methods for Engineers*, 7<sup>th</sup> Edition, McGraw-Hill, Boston.
- [19] Volponi, A. J., 1999, “Gas Turbine Parameter Corrections,” *Journal of Engineering for Gas Turbines and Power*, **121** Oct. pp. 613-621.
- [20] Brown, D. Internal Progress Report for US Army Phase II SBIR Contract No. A03-037.

## BIOGRAPHICAL SKETCH

Eric Howell received his Bachelor of Science degree cum laude in mechanical engineering from the University of Florida in 2004. His deep-seated fascination with the thermal sciences compelled him to pursue a master's degree at the University of Florida, while working as a Research Assistant in the Energy and Gasdynamics Systems Laboratory. The Author received his Master of Science degree in mechanical engineering from the University of Florida in 2007.